2016

Metamorphic Conditions of Aluminous Gneisses in the Sawtooth Metamorphic Complex, Idaho, USA: Implications for the Middle-Lower Crust

Eleanor Wesley-Anne Smith
Louisiana State University and Agricultural and Mechanical College

METAMORPHIC CONDITIONS OF ALUMINOUS GNEISSES IN THE SAWTOOTH METAMORPHIC COMPLEX, IDAHO, USA: IMPLICATIONS FOR THE MIDDLE-LOWER CRUST

A Thesis

Submitted to the Graduate Faculty of the
Louisiana State University and
Agricultural and Mechanical College
in partial fulfillment of the of the
requirements for the degree of
Master of Science

in

The Department of Geology and Geophysics

by
Eleanor Smith
B.S., Louisiana State University, 2015
May 2016

ACKNOWLEDGMENTS

I would like to thank my committee members Dr. Barbara Dutrow, Dr. Darrell Henry, and Dr. Karen Luttrell for sharing their invaluable expertise with me during my graduate career and for their time, patience, and encouragement as I completed this project. I would especially like to thank Dr. Dutrow providing me challenging research opportunities early in my career, for her constant motivation, and for teaching me the skills necessary to succeed in my future endeavors. I owe my successes during my undergraduate and graduate careers to her dedicated guidance.

I would also like to thank Mr. Rick Young in the LSU rock lab for creating my thin sections, Dr. Nele Muttik for assistance with the electron microprobe, and Ashley Thrower for help collecting samples in the field. Sample collection was made possible through the National Forest Service by David Fluetsch and Lieze Dean of the Sawtooth National Recreation Area.

Funding was provided by NSF-Tectonics #1145073 awarded to Drs. Barbara, Dutrow, Paul Mueller, and David Foster and a Rocky Mountain Section Geological Society of America Undergraduate Research Grant awarded to me. I would also like to thank the LSU Department of Geology and Geophysics for awarding me several undergraduate scholarships and a graduate teaching assistantship.

TABLE OF CONTENTS

ABSTRACT

The Sawtooth Complex (SMC) of central Idaho contains metasedimentary units that elucidate the pressure-temperature conditions and potentially, the evolution of Precambrian crust in the northwestern United States. Petrographic analysis, whole rock geochemistry, and geothermobarometry combined with thermodynamic phase equilibrium modeling record a regional metamorphic pathway for SMC aluminous gneisses characterized by burial to middle-lower crustal levels with at least two deformational events, followed by a retrograde overprint.

P-T conditions are generally consistent with the peak assemblage of SMC aluminous gneisses of bt + grt + sil + ilm + zrn + mnz ± pl ± qtz ± kfs ± ap ± xn ± py ± po ± ccp ± gr. This assemblage constrains P-T conditions to be below the biotite dehydration-melting reaction, within sillimanite zone, and above the thermal stability of muscovite. Abundant leucosomes suggest melt. Peak conditions are associated with two deformational events evidenced by crenulation cleavage and rotated inclusions in garnet.

Classic geothermobarometry combined with thermodynamic phase equilibrium modeling constrain peak pressure conditions. These pressures decrease from ~11 kbars in the south to ~7.5 kbars in the north at similar temperatures of ~800 °C. Mineral assemblage diagrams are used to identify likely post-peak reequilibration features and used to determine retrograde conditions. SMC samples share a similar retrograde path to conditions near ~4-6 kbars and ~600-650 °C into the stability field of muscovite.

Peak pressures from south the north suggest burial depths between 33 and 23 km (3 km /kbar). This range in burial depth indicates that the SMC records different crustal levels that may have been juxtaposed by faulting.

Whole rock geochemical data is consistent with a mature shale protolith having undergone significant weathering of feldspar to clay minerals with varying amounts of potassium metasomatism and sedimentary sorting. These shales were likely deposited in a passive margin environment and may represent a deep-water continuation of calc-silicates found adjacent to aluminous gneisses.

P-T conditions of SMC aluminous gneisses are consistent with burial to middle crust with subsequent uplift. P-T conditions of SMC aluminous gneisses may elucidate metamorphic conditions along the southwestern margin of the Lauretian craton during the development of Rodinia.

INTRODUCTION

The North American continent offers one of the most complete geologic records of continental formation. It resided at the center of both the Nuna and Rodinia supercontinents, offering invaluable insight into the supercontinent cycle (e.g. Whitmeyer and Karlstrom, 2007). The geologic core of North America, the Laurentian craton, formed through a series of plate collisions between Archean microcontinents, 2.0-1.8 Ga, known as the Trans-Hudson Orogeny (e.g. Hoffman, 1988; Whitmeyer and Karlstrom, 2007). These microcontinents include mostly reworked Archean crust but also entrap slivers of juvenile volcanic arcs at suture zones (e.g. Mogk et al., 1992; Foster et al., 2006). Following the formation of the Archean-Paleoproterozoic core of North America, accretion of juvenile volcanic arcs and oceanic terranes built the growing continent from its southern margins during the Yavapai (1.71-1.68 Ga), Mazatzal (1.70-1.65 Ga), and Grenville orogenies (1.30-0.95 Ga; e.g. Whitmeyer and Karlstrom, 2007).

Middle-lower crustal rocks are key to understanding the accretion of North American Archean-Proterozoic terranes and the associated orogenic events that created the Laurentian Craton. Lack of outcrops of Precambrian middle-to-lower crustal rocks renders the tectonic reconstructions of Laurentia largely difficult to constrain. In the Idaho area, the Idaho Batholith and volcanic rocks from the Yellowstone hotspot produced during Cretaceous-Tertiary magmatic activity cover large expanses of Precambrian basement rock (Mueller et al., 2005; Gaschnig et al., 2011). Also masking Precambrian rocks in this region are thick sedimentary units such the Windermere Supergroup (> 780 Ma) and the 1.47-1.44 Ga Belt-Purcell Supergroup (Fig. 1; e.g. Lund et al., 2003; Mueller et al., 2005; Foster et al., 2006).

Within this enigmatic region, in the Sawtooth Range in central Idaho, lies the Sawtooth Metamorphic Complex (SMC). The SMC contains high-grade metamorphic rocks suspended as a roof pendant within the Idaho and Sawtooth batholiths (Anderson, 1995; Dutrow at al., 1995; Metz, 2010; Bergeron, 2012; Fukai, 2013). The SMC is located at the intersection of Archean-Proterozoic terranes i.e. the >2.5-1.5 Ga Priest River block, the 2.6-3.3 Ga Medicine Hat block, the >2.5 Ga Wyoming craton, and the >2.5 Ga Grouse Creek block (Fig. 1; e.g., Hoffman, 1988; Mogk et al., 1992; Foster et al., 2006) and occur within the proposed 2.4-1.6 Ga Selway terrane (Foster et al., 2006). Characterization of SMC lithologies and metamorphic conditions may elucidate a relationship between the SMC and the surrounding terranes. Limited studies on various SMC lithologies have yielded upper greenschist to lower-granulite facies conditions but the relationship between these lithologies and their individual pressure (P)-temperature (T) conditions remain unclear (Anderson, 1995; Dutrow et al., 1995; Metz, 2010; Bergeron, 2012; Dutrow et al., 2013; Fukai, 2013; Dutrow et al, 2014).

Detailed characterization of a single lithology using classic geothermobarometry techniques in conjunction with mineral assemblage modeling constrains on the P-T conditions of the SMC. These data may reveal significant relationships between the SMC and surrounding exposures of basement rock that can be incorporated into the history of crustal evolution in the western United States and within the SMC itself.

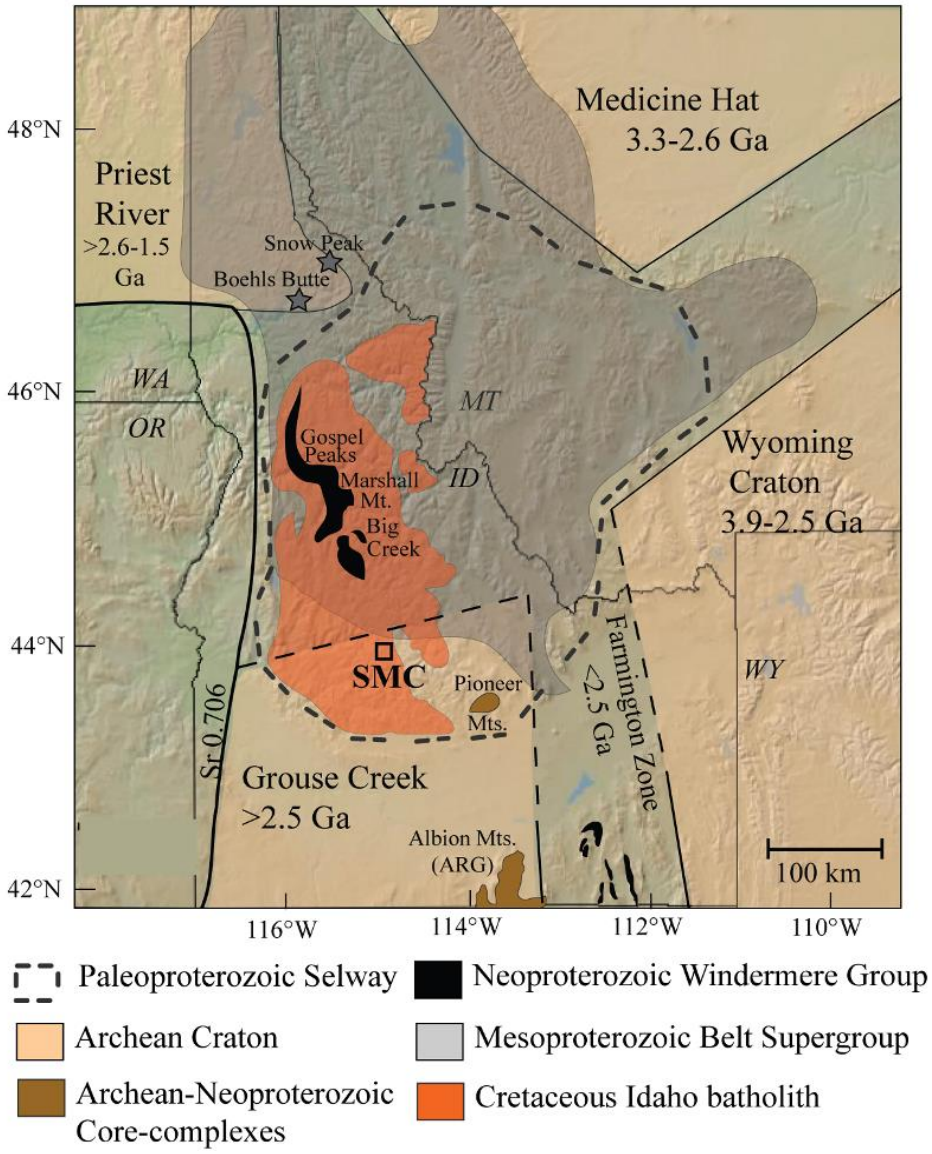

Figure 1: Location of the SMC in central Idaho. It occurs in the proposed Selway terrane among Archean-Proterozoic terranes and the Idaho batholith (from Fukai, 2013, after Foster et al., 2006, Gashnig et al., 2012, and Lund et al., 2003).

Aluminous gneisses occur within the SMC and contain a mineral assemblage that is ideal for determining the conditions of formation (e.g., Anderson, 1995; Dutrow et al., 1995; Metz, 2010; Dutrow et al., 2013). P-T conditions of aluminous gneisses can be compared with P-T conditions for surrounding exposures of Archean-Proterozoic basement, such as the Pioneer Core Complex and the Belt-Purcell Supergroup, may provide a method of correlation.

This study combines detailed petrographic analysis, whole rock geochemical analysis, mineral chemical analysis, and classic geothermobarometric techniques and mineral assemblage diagrams to constrain the metamorphic conditions of formation and geochemical signatures of SMC aluminous gneisses. These data will provide insights into the crustal evolution of this portion of Laurentia.

Regional Geologic Setting:

The SMC occurs at high elevation within the northern Sawtooth Range in central Idaho (Reid, 1963; Fig. 2). Steep arêtes flanking U-shaped valleys carved during Pleistocene glaciation account for the serrated profile of the range (Maley, 1987). The Sawtooth Range is largely composed of granitic rocks of the Tertiary Sawtooth Batholith (46 – 47 Ma) that intrude monzodioritic rocks of the Cretaceous Idaho Batholith (100-75 Ma; Reid, 1963; Dutrow et al., 2013). The range was uplifted during Tertiary Basin and Range extension as a horst block adjacent to the downdropped Stanley Basin and is separated from the basin by the Sawtooth normal fault (e.g. Reid, 1963; Thackray et al., 2013).

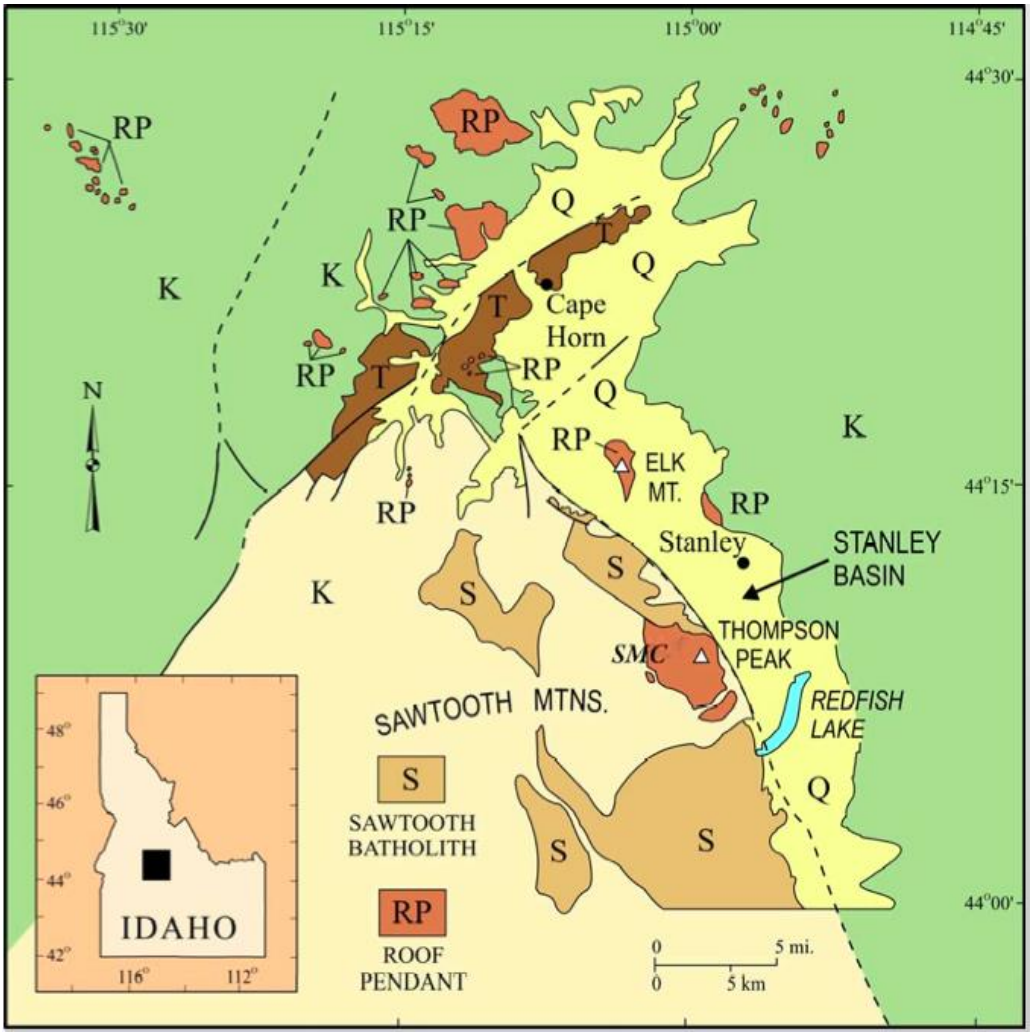

Figure 2: Location of the SMC roof pendant within the northern Sawtooth Range. It is bound to the north by the Sawtooth Batholith, to the west and south by the Idaho Batholith, and separated from the Stanley Basin by the Sawtooth normal fault (Dutrow et al., 1995). K = Cretaceous. The K beige unit is the Idaho Batholith, the K green unit represents sedimentary and igneous rocks, Q is Quaternary alluvium, and T is composed of Tertiary volcanics. Geologic map adapted from Fischer et al., 1983, 2001.

The SMC occurs as a metamorphic roof pendant largely within the Sawtooth Batholith and is composed of numerous N-S striking metamorphic lithologies. The dominant lithologies are aluminous gneisses, quartzofeldspathic gneisses, calc-silicate gneisses, amphibolites, quartzites, and marble mylonites (Anderson, 1995; Dutrow at al., 1995; Metz, 2010; Bergeron, 2012; Fukai, 2013; Ma et al., 2016). Aluminous gneisses

commonly occur intercalated in quartzofeldspathic gneisses and crop out in the saddle between Thompson and Williams Peak, in the basin north of Thompson Peak, near Goat Lake, and in the eastern fork of Iron Creek (Fig. 3; Metz, 2010; Dutrow et al., 2013).

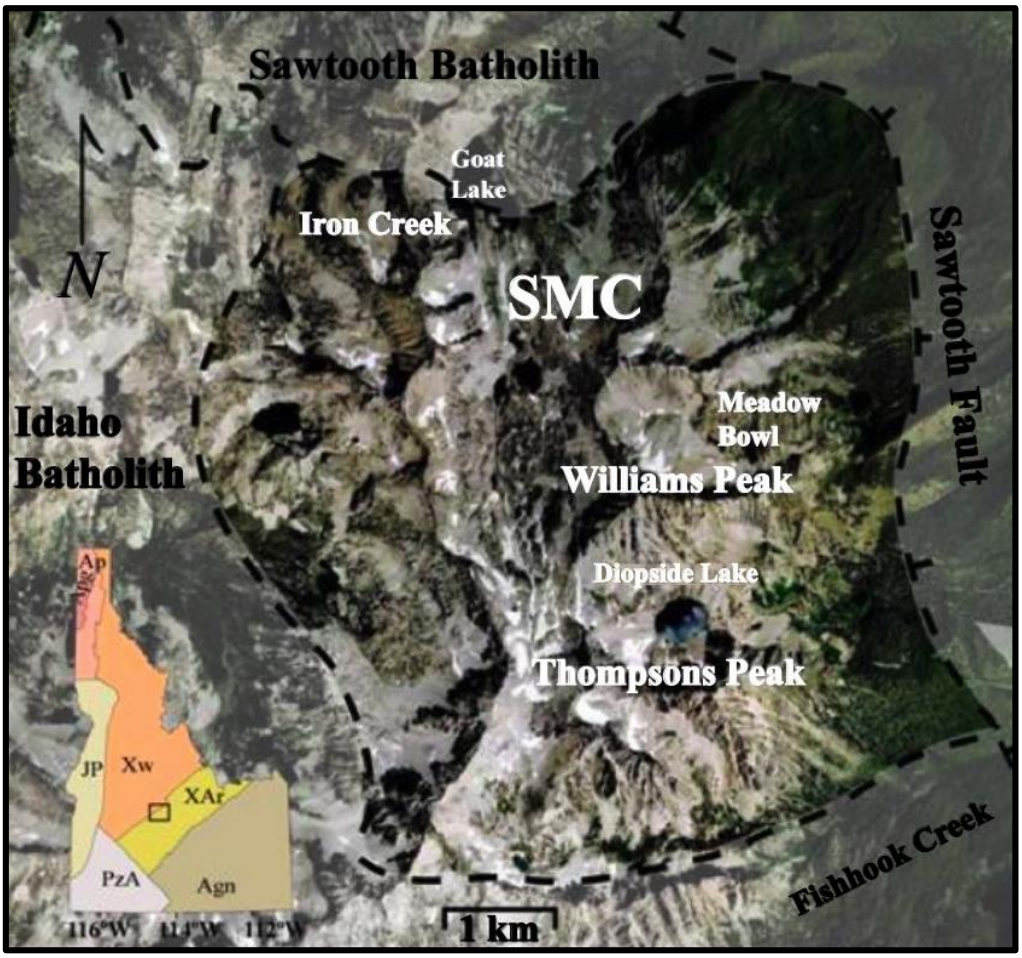

Figure 3. Google Earth image with locations of interest labeled. The SMC in central Idaho is shown by the small box. Map from Fukai (2013). Aluminous gneisses occur between Goat Lake to Thompson Peak and in the eastern fork of Iron Creek (Metz, 2010; Dutrow et al., 2013).

The SMC was initially mapped as undifferentiated Precambrian metamorphic rocks (Reid, 1963). Whole-rock Sm/Nd depleted mantle model ages from a single sample of each of four lithologies, a quartzite, biotite calc-silicate, calc-silicate, and an amphibolite, yield Precambrian ages from 2.4 to 1.6 Ga (Dutrow et al., 1995). U-Pb

detrital zircon ages from two SMC quartzite units west of Diopside Lake (Fig. 3) yield maximum depositional ages of 1068 ± 6 Ma and 1059 ± 24 Ma and one quartzite from east of Diopside Lake yields a maximum depositional age of 1704 ± 108, confirming that SMC lithologies include Precambrian components (Bergeron, 2012). More recently, U-Pb zircon ages from 12 SMC metapsammites, including some near Thompson Peak of are dominantly of five age groups, 2.79-2.65, 1.99-1.76, 1.87, 1.67, 1.49-1.33, and 1.22-1.02 Ga, consistent with Laurentian sources. Maximum depositional ages are constrained to the Cambrian by three Cambrian aged detrital zircons (529 ± 9 Ma, 496 ± 5 Ma and 526 ± 6 Ma; Ma et al., 2016).

The metamorphic conditions of SMC samples from the Headwall near Thompson Peak were first investigated by Anderson (1995) and Dutrow et al. (1995). These studies indicate that SMC aluminous gneisses from both Thompson Peak and Iron Creek record peak conditions between 675-750 °C at >8 kbars pressure. SMC amphibolites, aluminous gneisses, and one calc-silicate also record a lower-grade amphibolite facies overprint (550-650 °C) and mylonites record a greenschist facies event (320-350 °C; Dutrow et al., 1995). Geothermobarometry using TWQ, the multiequilibria approach (Berman, 1991), calculated peak conditions of 765 ± 10 °C and 6.54 ± 0.11 kbars for a grt-sil-bt aluminous gneiss collected near Thompson Peak (Anderson, 1995; mineral abbreviations in Table 1 from Whitney and Evans 2010).

Table 1: Mineral Abbreviations, (from Whitney and Evans, 2010)

Ab	Albite
Alm	Almandine
An	Anorthite
Ap	Apatite
Bt	Biotite
Ccp	Chalcopyrite
Chl	Chlorite
Crd	Cordierite
Gr	Graphite
Grs	Grossular
Grt	Garnet
Hc	Hercynite
Hem	Hematite
Ilm	Ilmenite
Ksp	Alkali Feldspar
Mnz	Monazite
Ms	Muscovite
Or	Orthoclase
Pn	Pinite
Po	Pyrrhotite
Pl	Plagioclase
Py	Pyrite
Qtz	Quartz
Rt	Rutile
Ser	Sericite
Sil	Sillimanite
Sps	Spessartine
Ttn	Titanite
Xn	Xenotime
Zrn	Zircon

Six aluminous gneisses studied by Metz (2010) from the Iron Creek area contain the post peak mineral assemblage crd + bt + pl + qtz + grt + sil + ms + kfs + and + ilm + ttn + ccp + po + py + mnz + zrn. These samples yield temperatures between 615-774 °C using Garnet-Biotite (GB) geothermometry (Holdaway, 2000) and lower pressures of 4.3-5.8 kbar using Garnet-Aluminosilicate-Plagioclase (GASP) geobarometry (e.g. Holdaway, 2001). Using TWQ (Berman, 1991), these gneisses yielded conditions of 660-770 °C and 5.2-6.7 kbar, similar to samples from Thompson Peak. Variations in calculated P-T conditions are interpreted to reflect local resetting at post-peak condtions. Peak conditions of the aluminous gneisses were followed by rehydration in the muscovite stability field and at low-pressures the formation of cordierite and andalusite that overprint foliation. These minerals are not observed elsewhere in the SMC. Iron Creek and Thompson Peak samples appear to have different retrograde assemblages, suggesting different exhumation/uplift histories (Metz, 2010; Dutrow et al., 2013; Dutrow et al., 2014).

Mineral chemistry of aluminous gneisses used by Metz (2010) and Anderson (1995) were reevaluated by Dutrow et al. (2013) using updated geothermobarometric methods (Wu et al., 2004). Thompson Peak samples contain the mineral assemblage sil + grt + ksp + pl + bt + qtz + ilm + mnz + zrn + rt + ttn + po with minor secondary poikiloblastic ms. Garnet-biotite-plagioclase-quartz geothermobarometry (GBPQ; Wu at al., 2004), garnet-biotite geothermometry (GB; Holdaway, 2000), and garnet-aluminosilicate geobarometry (GASP; Holdaway, 2001) yielded conditions of 729-747 ± 25 °C and 6.2-7.2 ± 1.2 kbar for four samples. One Goat Lake sample containing the assemblage crd + bt + pl + qtz + grt + sil + kfs + ilm + ccp + po + ttn + mnz + zrn + py,

yielded GB temperatures of 788 ± 25 °C, GBPQ pressures of 8.31 ± 1.2 kbars using, and GASP pressures of 9.50 kbar. Five Iron Creek samples record lower pressures than Thompson Peak and Goat Lake samples. These conditions are 700-775 ± 25 °C and 4.6-5.8 ± 1.2 kbars. SMC aluminous gneisses record peak conditions in the upper amphibolite to lower granulite facies (Table 2; Anderson, 1995; Metz, 2010; Dutrow et al., 2013).

Pressure can be used to determine burial depth assuming by assuming an average density of the overlying rocks. Pressures calculated for Thompson Peak samples indicate middle-lower crustal burial depths of 24-30 km. In contrast, pressures calculated for Iron Creek samples indicate 18 km burial depth, suggesting that SMC samples are from different crustal levels (Dutrow et al., 2013). A more robust series of P-T constraints for SMC aluminous gneisses are needed to assess variation in P-T conditions in the SMC. Additionally, these data will provide the necessary information to select samples for mineral geochronology, which must be interpreted in the petrologic context of the sample.

A petrologic characterization of SMC calc-silicate gneisses can be compared to that of aluminous gneisses to assess their metamorphic relationship and history. Fukai (2013) conducted a high spatial-resolution study of the calc-silicate rocks near the Thompson Peak and Diopside Lake (Fig. 2). Isobaric T-X (CO_2, H_2O) pseudosections (created by Perple_X version 6.6.8; Connolly, 2005; Connolly, 2009) of 10 calc-silicate gneisses were used to constrain thermal and metamorphic conditions based on mineral assemblages and textures (Fukai, 2013). These calc-silicates record two distinct metamorphic events (M1, M2) and two deformational events (D1, D2). M1 reached temperatures of >750-775 °C and are assumed to represent peak conditions based on

mineral assemblages that include clinopyroxene. This event was followed a high P-T, ductile deformational event (D1). M2 postdates M1 and D1 and reached temperatures of ~550-725 °C, based on amphibole stability and amphibole textures that cross cut M1 minerals. D2 was a late stage brittle-ductile event preserved by brittle deformation and mylonitic texture (Fukai, 2013). The occurrence of two metamorphic events suggests that calc-silicates record a different temperature path than aluminous gneisses, perhaps due to the assembly of tectonic slices in the SMC (Dutrow et al., 2013). A similar analysis of P-T conditions of SMC aluminous gneisses may reveal a relationship between aluminous gneisses and calc-silicates, which has implications for the architecture of the SMC as a whole.

Table 2: Previous geothermobarometric calculations for peak metamorphism (Dutrow et al. 2013)

Sample number	Location	T (°C) GB ± 25 °C Holdaway, 2000	P (kbar) GBPQ ± 1.2 kbars Wu et al., 2004	P (kbar) GASP ± 1.5 kbars Holdaway, 2001
ST-95-08	Thompson Peak	736	6.3	6.2
ST-95-06a	Thompson Peak	729	7.1	8.0
ST-95-07	Thompson Peak	747	7.2	10.0
SMC-12-111	Thompson Peak	717	7.1	11.1
SMC-12-003	Thompson Peak	771	8.7	-
SMC-12-134	Goat Lake	788	8.3	9.5
IC-08-01a	Iron Creek	774	3.7	5.8
IC-08-01a	Iron Creek	615	5.4	4.6
IC-08-01b	Iron Creek	704	4.7	5.8
IC-08-01a1	Iron Creek	751	4.3	-
IC-08-01e	Iron Creek	735	4.8	4.9

A petrologic characterization of SMC calc-silicate gneisses can be compared to that of aluminous gneisses to assess their metamorphic relationship and history. Fukai (2013) conducted a high spatial-resolution study of the calc-silicate rocks near the Thompson Peak and Diopside Lake (Fig. 2). Isobaric T-X (CO_2, H_2O) pseudosections (created by Perple_X version 6.6.8; Connolly, 2005; Connolly, 2009) of 10 calc-silicate gneisses were used to constrain thermal and metamorphic conditions based on mineral assemblages and textures (Fukai, 2013). These calc-silicates record two distinct metamorphic events (M1, M2) and two deformational events (D1, D2). M1 reached temperatures of >750-775 °C and are assumed to represent peak conditions based on mineral assemblages that include clinopyroxene. This event was followed a high P-T, ductile deformational event (D1). M2 postdates M1 and D1 and reached temperatures of ~550-725 °C, based on amphibole stability and amphibole textures that cross cut M1 minerals. D2 was a late stage brittle-ductile event preserved by brittle deformation and mylonitic texture (Fukai, 2013). The occurrence of two metamorphic events suggests that calc-silicates record a different temperature path than aluminous gneisses, perhaps due to the assembly of tectonic slices in the SMC (Dutrow et al., 2013). A similar analysis of P-T conditions of SMC aluminous gneisses may reveal a relationship between aluminous gneisses and calc-silicates, which has implications for the architecture of the SMC as a whole.

Regional basement exposures:

The Wyoming craton

The Wyoming craton is a thick, geologically distinct unit of Archean aged rocks subdivided into the 2.8-2.9 Ga Beartooth Bighorn Magmatic Zone (BBMZ), the Southern

Accreted Terranes (SAT), and the Montana Metasedimentary Terrane (MMT; Fig. 1). Wyoming craton rocks are characterized by unique Pb isotopic signatures (e.g. Mueller et al. 2003). The northwest portion of the Wyoming craton is made up of mid-Archean gneisses (3.2-3.5 Ga) intermingled with younger metasedimentary units (2.5-3.5 Ga), including pelitic schists and quartzofeldspathic gneisses, which constitute the Montana metasedimentary terrane (MMT; e.g. Chamberlain et al., 2003; Foster et al, 2006). The MMT is interpreted as an original continental platform sedimentary sequence that experienced upper amphibolite-lower granulite facies conditions during the late Archean (e.g. Mueller et al., 2003; Chamberlain et al., 2003; Kellogg et al., 2009). Peak metamorphic conditions of ~800°C and ~6-7 kbars are recorded in trondhjemitic gneisses. A clockwise, regional metamorphic path is suggested by mineral inclusions, reaction textures and P-T calculations from mineral cores to rims (e.g. Mogk, 1990). Metamorphic ages are consistent with Archean calc-alkaline magmatism, suggesting the presence of a long-lived active margin.

The Great Falls tectonic zone

The Great Falls tectonic zone (GFTZ) is an area of Paleoproterozoic tectonic activity between the northwestern border of the Wyoming craton and southeastern border of the Medicine Hat block (e.g. Mueller et al., 2005; Fig. 1). Trace element data consistent with convergent margins and a north-dipping paleosubducted slab beneath the Medicine Hat and Hearne cratons indicate the GFTZ was an active continental margin up to ~1.86 Ga (Gorman et al., 2002; Mueller et al., 2002; Mueller et al., 2005). Western exposures of the GFTZ occur in the Tobacco Root Mountains and Highland Mountains, MT. A 1.77-2.06 Ga metabasaltic dike within a qtz + bt + sil + grt schist records P-T

conditions 600-730°C and 7-11 kbar (Cheney et al., 2004; Mueller et al., 2005). Ages of metamorphism are consistent with the collision of the Wyoming craton and Medicine Hat block (Mueller et al., 2002; Mueller et al., 2005).

The Priest River complex

The Priest River Complex is a metamorphic core complex exhumed between 46 and 55 Ma stretching from Spokane, Washington to Creston, British Columbia (Fig. 1). Four metamorphosed Precambrian rock units are exposed within the Priest River Complex, including meta-igneous and metasedimentary lithologies (e.g. Doughty et al., 1998). Metasedimentary units include the Hauser Lake gneiss, a migmatitic metasedimentary gneiss interlayered with quartzofeldspathic granofels, semipelitic schists, and amphibolites. Metamorphic condtions within the Hauser Lake gneiss a lie between 7 and 10 kbars and 675 and 930 °C, indicating it represents exhumed middle-lower crust (Doughty, 1995). U-Pb zircon ages from schists within Hauser Lake gneiss yield crystallization ages of about 1.58 Ga. Metasedimentary rocks in the Priest River complex are interpreted to be those of the Belt-Purcell Supergroup (Doughty et al., 1998).

The Belt-Purcell Supergroup

The Belt-Purcell Supergroup is a 15-20 km thick succession of middle-Proterozoic siliciclastic and carbonate strata in the northern Rocky Mountains (e.g. Ross et al, 1991; Fig. 1). Stretching from southwestern Montana to southern British Columbia, the Belt-Purcell Supergroup has been proposed to be an intracratonic rift basin filled with sediments between 1.40 and 1.47 Ga (e.g. Evans et al, 2000). Zircons within the lower two-thirds of Belt-Purcell Supergroup strata yield ages consistent with intra-Belt magmatic units (1.61-1.48 Ga), indicating their provenance from a magmatically active

source (e.g. Ross and Villeneuve, 2003). Metasedimentary units within these lower units include quartzites, pelitic schists, and calc-silicates. Metamorphic grade generally increases towards the Idaho batholith. Three regional metamorphic events are recorded for these rocks. The first (M1) is associated with regional contractional deformation (D1) at 480-625 °C and 4-6 kbars and is associated with the amalgamation of Rodinia at 1380-1300 Ma. The second event (M2), preserved in pelitic schists, is associated with the development of kyanite and sillimanite at peak conditions of 650-750 °C and 8-11 kbars followed by isothermal decompression (M3) resulting on the growth of andalusite. Deformation in M2 is obscured by M3. The timing of M2 is uncertain (e.g. Carey et al., 1992; Grover, 1992).

The Selway terrane

The Selway terrane is a proposed 2.4-1.6 Ga amalgamation of juvenile magmatic arcs west of the Wyoming craton in Montana and Idaho (Fig. 1; Foster et al., 2006). Outcrops of the Selway terrane occur in the Pioneer Range, ID, the Biltmore anticline, MT, the Tendoy Range, MT, the Highland Range, NV, the Bitterroot Range, ID and MT, and at Boehls Butte, ID (Foster et al, 2006). The Selway terrane is distinguished from the Wyoming craton by 2.4-1.8 Ga U-Pb zircon ages from orthogneisses and an amphibolite in southwestern Montana, by 1.93-1.72 Ga Sm-Nd depleted mantle model ages, and by arc-like Sr, Nd, and Pb isotopic signatures, which are consistent with abundant juvenile crust to the west of Archean exposures in the Wyoming craton (Mueller et al., 1996; Foster et al., 2006). The proposed Selway terrane, along with the Grouse Creek block, is thought to have accreted to the western margin of the Wyoming craton 1.80-1.76 Ga,

becoming pinned at the intersection of these terranes. The SMC lies in the area of the putative Selway Terrane.

The Pioneer Core Complex

The Pioneer Core Complex in the Pioneer Mountains, ID, 100 miles south of the SMC is a metamorphic core complex (Fig. 1) composed of two plates of Archean and Precambrian basement detached from an unmetamorphosed footwall of Paleozoic strata and is thought to be an extension of the Grouse Creek block (e.g. Link, 2009; Link, 2010). The lower plate is composed of Archean gneisses and Proterozoic quartzites, calc-silicates and pelitic gneisses that have been correlated with the Belt Supergroup. The middle plate is composed of 1.45-1.80 Ga calc-silicates, quartzites, marbles, and sillimanite-bearing pelitic schist metamorphosed during Cretaceous shortening to mid-lower amphibolite facies conditions (Silverberg, 1990; Vogl et al., 2012). Metasedimentary rocks contain zircons with 1.05-1.33 Ga cores and rims ~50 m.y. younger (Link, 2009). One grt-ms-sil-bt pelitic schist from the middle plate records P-T conditions of 655-701 °C and 4.4 kbars and preserves two deformational events (Smith et al., 2014).

The P-T conditions of lithologies from surrounding terranes can be compared with the P-T conditions of SMC aluminous gneisses. Additional samples of SMC aluminous gneisses must be characterized for a more robust interpretation of the relationship between the SMC and the surrounding Archean-Proterozoic terranes and the relationship between SMC aluminous gneisses and calc-silicates. Theses relationships have implications for crustal evolution in the western United States.

METHODS

To determine the P-T conditions of SMC aluminous gneisses, field sampling was conducted followed by analysis using the petrographic microscope, X-ray fluorescence (XRF), and the electron microprobe (EMPA). These data were used to interpret the P-T conditions of formation of SMC aluminous gneisses using various geothermobarometers and mineral assemblage modeling.

Hand sized samples were collected for this study and the latitude and longitude of their location noted. Samples were selected for further analyses based in the occurrence of pressure and temperature sensitive minerals, such as biotite, plagioclase, and garnet, and based on the lack of alteration.

Petrographic analysis:

Samples were cut into billets and crafted into thin sections at Louisiana State University. Thin sections were petrographically analyzed with an Olympus BH-2 petrographic microscope to determine mineral assemblages and metamorphic textures and to identify optimal minerals for mineral chemical analysis.

To determine the appropriate rock name, modal amounts of the mineral assemblages were obtained by point counting 1000 points using a petrographic microscope and point counting stage. These data were used to provide a name consistent with IUGS (Fettes and Desmons, 2007) using an excel program by D. Henry (personal communication). Differences in mineral assemblages and textures were compared to assess variation among SMC aluminous gneisses.

Electron microprobe analysis:

Quantitative mineral chemistry was obtained with the JEOL JXA-8230 Superprobe at LSU using wavelength dispersive spectroscopy (WDS). Minerals analyzed include garnet, biotite, and plagioclase. Garnet was analyzed for Si, Al, Ti, Cr, Fe, Mn, Mg, and Ca. One to two garnets were analyzed per sample on a core to rim traverse of five to seven points to check for compositional zoning. WDS elemental maps for two garnet grains of Fe, Mg, and Ca were made to visually depict concentration as a function of weight percent oxides and to check for compositional zoning. Biotite was analyzed for Si, Al, Ti, Cr, Fe, Mn, Mg, Ca, Na, K, and F. Ten to twenty spots were measured per sample and one to three spots were measured from each biotite grain. Measured grains were close to but not touching the analyzed garnet. Plagioclase was analyzed for Si, Al, Fe, Mg, Ca, Ba, Na, and K. Five to twenty spots were measured for each sample and one to seven spots were analyzed for each plagioclase depending on size to check for compositional zoning. Limits of detection for all elements are between 20 and 400 ppm. Precision and accuracy were monitored by analyzing well-characterized standards as unknowns between analysis of every sample.

Mineral formulae were calculated by normalizing analyses in weight-percent oxides to atoms per formula unit (apfu) using an excel program (D. Henry, personal communication). Garnet structural formulae were calculated on a 12-oxygen basis. Iron in garnet was measured as FeO and an assumed Fe^{3+} was calculated based on stoichiometry. Feldspar structural formulae were calculated on an 8-oxygen basis and biotite structural formulae were calculated on a 24-oxygen basis. The hydroxyl content in biotite was calculated assuming OH + F + Cl = 4. All Fe in biotite was calculated as Fe^{2+}.

Quantitative mineral chemistry provides highly precise data that were used in a variety of geothermobarometers to determine the P-T conditions of the samples. Mineral chemistry for garnet, plagioclase, and biotite are in Appendix A-C.

Geothermobarometry:

A variety of geothermobarometers can be used to determine the P-T conditions of aluminous gneisses by mineral chemistry of their pressure and temperature sensitive minerals. Mineral chemistry was grouped into core-to-rim pairs for geothermobarometry calculations. Chemical analyses for plagioclase and biotite that shows no chemical zoning was averaged. Inclusions (plagioclase and biotite) in garnet were paired with garnet chemistry consistent with their location in the garnet. Geothermobarometers used for aluminous gneisses include the garnet-biotite (GB) geothermometer and garnet-biotite-plagioclase-quartz (GBPQ) geobarometer of Wu et al. (2004) and Holdaway (2000) and the garnet-aluminosilicate-plagioclase (GASP) geobarometer (Holdaway, 2001). Additionally, the Ti-in-biotite (TiB) geothermometer was used (Henry et al., 2005).

The GB geothermometer is described by the reaction almandine + annite = pyrope + phlogopite. This reaction represents the temperature dependent Fe-Mg exchange between biotite and garnet. This geothermometer was empirically calibrated by Holdaway (2000) based on the 1978 experimental calibrations of Ferry and Spear (600-800 °C, 2.07 kbar), the 1983 experimental calibrations of Perchuk and Lavrent'eva (575-950 °C, 6.0 kbar), and the 1997 calibrations by Holdaway. Estimated error for the GB geothermometer is ± 25 °C (Holdaway, 2000).

For metapelites containing ilmenite or rutile that have equilibrated between ~3-6 kbar and coexist with graphite, quartz and an aluminosilicate, the Ti content in biotite can

serve as a useful geothermometer (Henry et al., 2005). The relationship between Ti content, temperature, and Mg/(Mg + Fe) values was calibrated empirically between 480 and 800 °C at 4-6 kbars by Henry et al. (2005) using a 529-sample data set from western Maine and south-central Massachusetts. The error of the TiB geothermometer is ± 24 °C at lower temperatures but decreases to ± 12 °C at higher temperatures (Henry et al., 2005). A limitation in using TiB is that Ti content in biotite is reduced at pressures greater than ~6 kbars, resulting in a lower apparent temperature (Henry et al., 2005).

The garnet-aluminosilicate-plagioclase (GASP) geobarometer, first proposed by Ghent (1976), is represented by the reaction grossular + aluminosilicate + quartz + anorthite. This geobarometer is based on the pressure sensitivity of calcium content in coexisting plagioclase and garnet. The GASP geobarometer was calibrated up to 12.3 kbar and 900 °C and has an error of ± 1.5 kbar (using Holdaway, 2001).

The garnet-biotite-plagioclase-quartz (GBPQ) geobarometer is based on the Fe- and Mg-model equilibria pyrope + grossular + eastonite + quartz = anorthite + phlogopite and almandine + grossular + siderophyllite + quartz = anorthite + annite (Wu et al., 2004). The GBPQ geobarometer was empirically calibrated between 1.0-11.4 kbar and 515-878 °C based on GB temperatures (Holdaway, 2000) and GASP pressures (Holdaway, 2001). The calibrations are consistent with the quaternary solid solution model for both garnet and biotite, as well as the Al-avoidance solution model for plagioclase. The error of the GBPQ geobarometer is ± 1.2 kbar (Wu et al., 2004).

Geothermobarometry using multiple geothermobarometers provides a robust suite of P-T data for SMC samples. A comparison of these data determines if samples represent the same metamorphic pathways relative to each other, to other SMC

lithologies, and to surrounding terranes, elucidating the P-T conditions of the middle-lower crust.

Whole rock geochemical analysis:

Whole rock geochemical analysis for major elements in weight percent oxides (SiO_2, TiO_2, Al_2O_3, FeO, MnO, MgO, CaO, Na_2O, K_2O, and P_2O_5) and trace elements in ppm (Ni, Cr, Sc, V, Ba, Rb, Sr, Zr, Y, Nb, Ga, Cu, Zn, Pb, La, Ce, Th, Nd, and U) as well as loss on ignition (LOI) was measured by X-ray fluorescence at Washington State University. The ThermoARL Advant'XP automated sequential wavelength spectrometer measures 29 major and trace elements with major elements normalized to 100%, volatile free. All Fe is reported as FeO. Precision is measured using two internal standards, BCR-P and GSP-1, between every 28 samples. Limits of determination are given in Table 3 (Johnson et al., 1999).

Mineral assemblage diagrams:

To determine the P-T conditions and possible P-T pathways under which the samples formed, whole rock analyses were used for calculating mineral assemblage diagrams. Theriak-Domino is a program that calculates mineral assemblage diagrams (pseudosections) based on the minimization of Gibbs free energy (de Capitani and Petrakakis, 2010). Mineral assemblage diagrams display equilibrium mineral assemblages over a range of temperature and pressure conditions for a specified bulk composition using an internally consistent thermodynamic database. The database used in these calculations was that compiled by Tinkham (2010) based on the data from Holland and Powell (1988). Activity models used in calculating phase equilibrium models are listed in Table 4.

Major Elements Unnormalized (wt%)	Replicate r2	Replicate LOD
SiO_2	0.99929	0.58
TiO_2	0.99992	0.017
Al_2O_3	0.99949	0.16
FeO*	0.99948	0.20
MnO	0.99983	0.002
MgO	0.99994	0.076
CaO	0.99976	0.064
Na_2O	0.99981	0.045
K_2O	0.99992	0.031
P_2O_5	0.99990	0.005
LOI	0.966	1.00
Normalized (wt %)		
SiO_2	0.99992	0.19
TiO_2	0.99996	0.012
Al_2O_3	0.99987	0.082
FeO*	0.99956	0.18
MnO	0.99988	0.002
MgO	0.99994	0.073
CaO	0.99998	0.043
Na_2O	0.99989	0.036
K_2O	0.99998	0.015
P_2O_5	0.99996	0.003
Trace Elements (ppm):		
Ni	0.9992	3.5
Cr	0.9998	3.0
Sc	0.997	1.6
V	0.9996	5.0
Ba	0.9997	11.7
Rb	0.9998	1.7
Sr	0.99992	4.6
Zr	0.99994	3.9
Y	0.9987	1.2
Nb	0.99987	1.2
Ga	0.955	2.7
Cu	0.994	7.4
Zn	0.9991	3.3
Pb	0.9966	2.6
La	0.9941	5.7
Ce	0.996	7.9
Th	0.997	1.6
Nd	0.992	4.3
U	0.983	2.7

*at 2 sigma

Table 3: Precision and Limited of detection for XRF analyses (Johnson et al., 1999).

Table 4: Activity models, database compiled by Tinkham (pers comm, 2010)

Biotite	White et al., 2007
Chlorite	Holland and Powell, 1998
Chloritoid	White et al., 2000
Cordierite	Holland and Powell, 1998
Feldspar	Holland and Powell, 2003
Garnet	White et al., 2007
Ilmenite	Tinkham pers comm, 2010
Staurolite	Holland and Powell, 1998
White mica	Coggon and Holland, 2002
Melt	Holland and Powell, 1998

Whole rock geochemistry was converted to moles of elements of Si, Al, Ti, Fe, Mg, Na, Ca, and K for input into Theriak-Domino using Rock Maker (Büttner, 2012). The negligible value of Mn (atomic proportions <0.5) was added to Fe. The degree of silica saturation was constrained by manipulating the degree of silica saturation input into the model until the modal amount of quartz calculated in the model was similar to the modal amount of quartz determined by point counting. The molecular proportion of H is set equal to LOI, assuming all LOI is H_2O, and to a range between 25-100. Theriak-Domino automatically calculates the moles of oxygen on a stoichiometric basis (de Capitani and Petrakakis, 2010).

By comparing the peak assemblages of SMC samples with the assemblages calculated by Theriak-Domino, the P-T conditions at which the stable assemblage formed are constrained. Compositional isolines calculated by Theriak-Domino are compared to mineral chemistry from EMPA to further constrain P-T. Mineral inclusions, retrograde overprints, and zoning patterns are used to determine approximate metamorphic pathway of the samples based on the phase equilibrium modeling results. These data are compared with those P-T data determined by other classical geothermobarometric techniques described above.

RESULTS

Fifteen aluminous gneisses from the SMC were chosen for detailed study based on mineralogy and presence of pressure and temperature sensitive minerals. Samples chosen have minimal alteration. The samples cover the two-mile length of the SMC (Fig. 3). Nine samples were chosen from near the Headwall between Thompson Peak and Williams Peak in the southern SMC, three samples were chosen from the central SMC (referred to as basin samples), and three samples were chosen from near Goat Lake in the northern SMC (Fig. 4; Table 5).

Table 5: Sample names and locations in the SMC, Idaho, listed from north to south

Sample number	Lat/Lon	Elevation (ft)
SMC-14-034	44° 10'0.17"N 115° 1'7.38"W	8657'
SMC-14-035	44° 10'0.17"N 115° 1'7.38"W	8657'
SMC-14-027	44° 9'45.42"N 115° 0'57.96"W	8861’
SMC-14-031	44° 9'24.66"N 115° 0'52.56"W	8847'
SMC-15-025a	44° 9'20.09"N 115° 1'3.50"W	8884'
SMC-14-039	44° 9'7.08"N 115° 0'59.58"W	9006'
SMC-13-131	44° 8'48.95"N 115° 0'51.55"W	9803'
SMC-13-130	44° 8'49.20"N 115° 1'0.12"W	9689'
SMC-14-053b	44° 8'49.20"N 115° 0'45.18"W	9751'
SMC-13-127	44° 8'40.49"N 115° 0'48.13"W	9814'
SMC-13-128	44° 8'40.49"N 115° 1'5.70"W	9592'
SMC-13-116	44° 8'33.00"N 115° 0'49.86"W	9974'
SMC-13-118	44° 8'31.49"N 115° 0'49.79"W	10061'
SMC-13-101	44° 8'30.16"N 115° 0'49.79"W	8639'
SMC-13-119	44° 8'31.38"N 115° 0'49.68"W	10085'

Visual evaluations suggest that the samples are migmatitic metapelitic and semipelitic schists and gneisses. Both gneisses and schists occur over the length of the SMC and are not restricted to a specific geographic area. Gneisses are light-colored and contain non-foliated granoblastic quartz and plagioclase with biotite (Table 6). Large red-brown garnet porphyroblasts (3-5 mm) occur throughout (Figs. 5A, 5B, 5C). Foliated

layers of biotite, sillimanite, and muscovite are intercalated with granoblastic minerals (Figs. 5A, 5C). Some gneisses occur in conjunction with light-colored tonalitic veins (Fig. 5B). Three gneisses collected north of Thompson Peak in the basin contain elongate leucocratic bands of quartz and minor plagioclase (Figs. 6A, 6B).

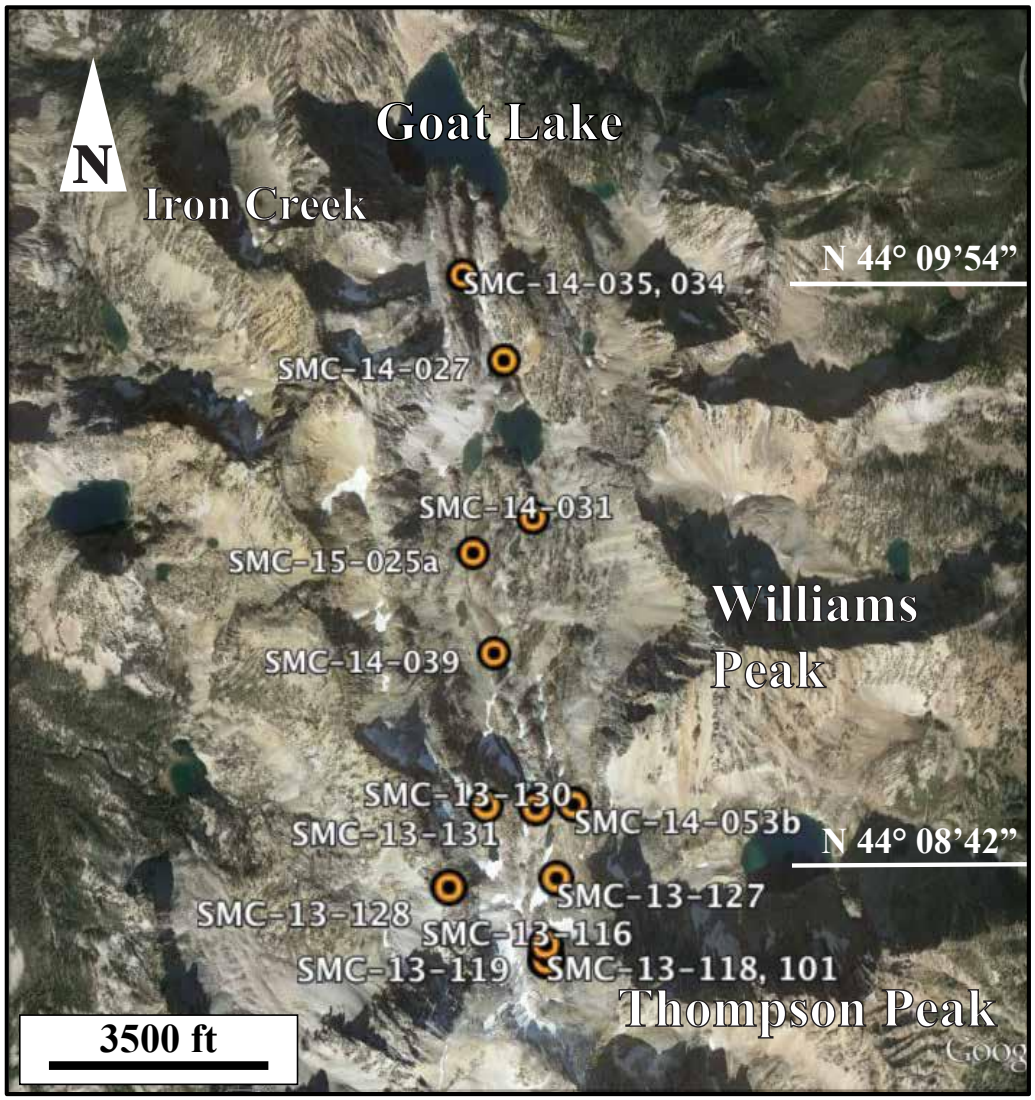

Figure 4: Location of SMC aluminous gneisses used in this study near Goat Lake, at the Headwall near Thompson Peak, and in the basin north of Thompson Peak, image from Google Earth.

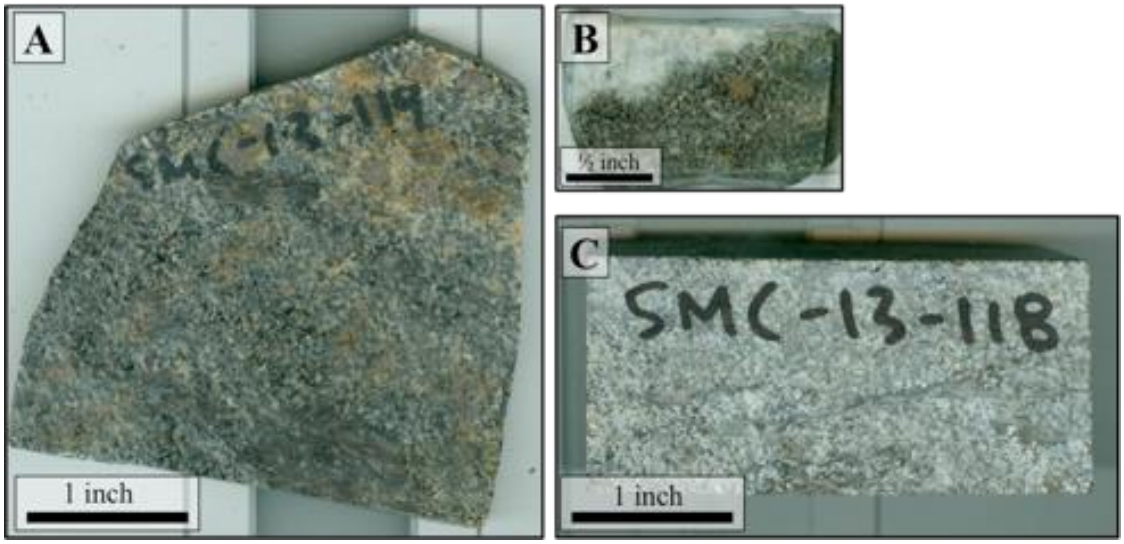

Figure 5: Optical scans of samples studied: (A) slab of SMC-13-119, (B) billet of SMC-13-053b, and (C) slab of SMC-13-118 showing dominantly gneissic texture composed of plagioclase, quartz, biotite, and garnet porphyroblasts. Gneisses contain foliated pelitic layers composed of biotite and sillimanite. Some samples occur with tonalitic veins composed of feldspar and quartz as seen in (B) SMC-14-053b.

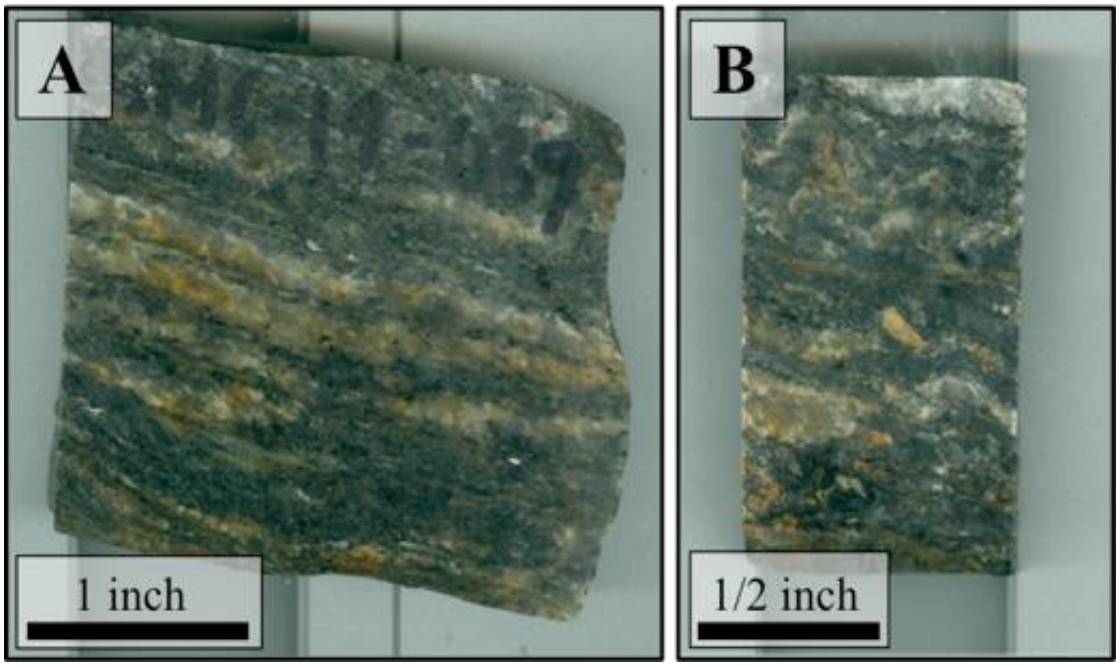

Figure 6: Optical scan of samples studied: (A) slab of SMC-14-039 and (B) billet of SMC-15-025a showing gneissic texture defined by foliated biotite, muscovite, and sillimanite and quartz rich leucosomes with minor plagioclase and sparse, red garnet porphyroblasts.

Table 6: Mineral Modes of SMC samples studied.

	Major minerals							Accessory minerals								
Sample number*	sil	grt	bt	ms	pl	qtz	crd	ilm	ap	zrn	mnz	xn	hc	py	po	ccp	gr
SMC-13-119	9	11	34	2	28	5		0.1	Tr#	Tr	Tr						0.1
SMC-13-118	7	8	29	4	41	11		Tr	Tr	Tr	Tr					Tr	Tr
SMC-13-101	9	5	17	6	49	14		Tr	Tr	Tr	Tr						Tr
SMC-13-116	2	29	25	13	25	5		1	Tr	Tr	Tr			Tr	Tr	Tr	Tr
SMC-13-128	10	7	27	12	18	22		Tr	Tr	Tr	Tr						Tr
SMC-13-127	17	27	12	4	22	3	11	2	Tr	Tr	Tr		2	Tr		Tr	
SMC-13-053b	3	4	16	6	56	9	4	2	Tr	Tr	Tr		Tr				
SMC-13-130	23	15	39	14	3	1		3	Tr	Tr	0.1						0.1
SMC-13-131		14	22	4	31	22		Tr	Tr	Tr	1				Tr		
SMC-14-039	8	4	15	18	2	52		Tr	Tr	Tr	Tr						Tr
SMC-15-025a	11	6	18	15	2	44		Tr	Tr	Tr	Tr				Tr		Tr
SMC-14-031	40	15	31	1	5	4		1		Tr	Tr						
SMC-14-027	2		16	47	Tr	34		1	Tr	Tr	Tr						Tr
SMC-14-034	25	13	27	6	1	19		Tr		Tr	Tr	Tr			Tr	Tr	Tr
SMC-14-035	6	5	2	57	Tr	31		Tr	Tr	Tr	Tr						

* Samples listed from south to north
% Mineral abbreviations in Table 1
# Trace minerals (< 1 %) labeled (Tr)

Schists contain higher proportions of foliated biotite, sillimanite, and muscovite than the gneisses (Figs. 7, 8A, 8B). Some schists have crenulation cleavage visible in hand specimen (Fig. 8A, 8B). Schists contain abundant garnet porphyroblasts (1-5 mm), which are augen shaped and typically surrounded by thin haloes of white plagioclase (Figs. 7, 8A, 8B). Elongate leucosomes composed of plagioclase and quartz occur concordantly with foliation (Figs. 7, 8).

Figure 7: Optical scan of a slab of SMC-13-130 showing schistose texture defined by foliated layers of biotite and sillimanite with abundant garnet porphyroblasts and sparse leucosomes of plagioclase and quartz.

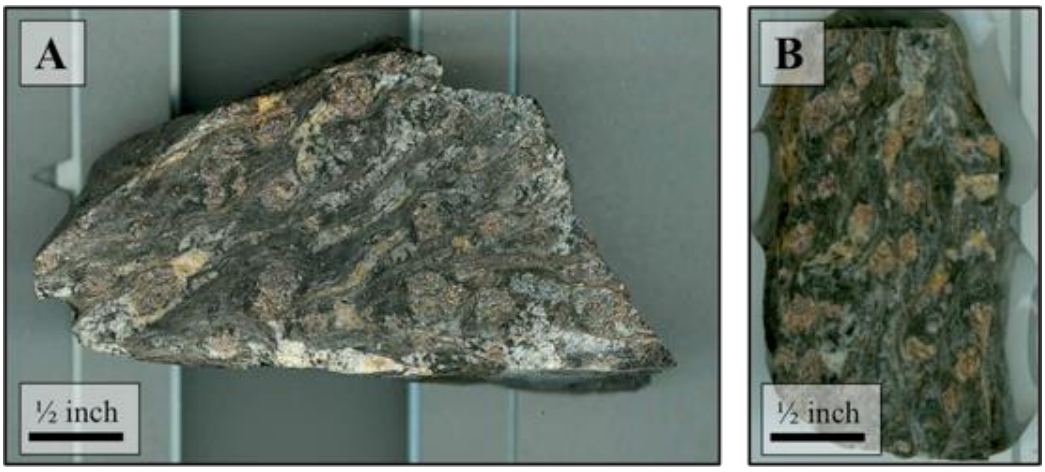

Figure 8: Optical scans of samples studied: (A) Slab and (B) billet of SMC-14-031 showing gneissic texture defined by crenulated layers of biotite and sillimanite imbedded with elongate leucosomes of plagioclase and abundant garnet porphyroblasts.

Petrographic analysis:

All samples are lithologically similar metapelites and semipelites and contain the common assemblage pl + qtz + bt + ms + grt + ilm + zrn + mnz ± crd ± hc ± ap ± xn ± py ± po ± ccp ± gr (Table 5). Modal mineral assemblages were used to assign rock names (Table 7). Twelve samples are metapelites. Metapelites contain less than 60% plagioclase and quartz with greater than 40% biotite, muscovite, sillimanite, and garnet. Three samples are semipelites. Semipelites contain greater than 60% plagioclase and quartz and less than 40% biotite, muscovite, sillimanite, and garnet.

Table 7: Rock Types based on texture and modal mineralogy

Sample #	Sample Rock Type
Headwall	
SMC-13-131	Migmatitic ms-grt-semipelitic gneiss
SMC-13-130	Migmatitic ms-grt-sil-bt metapelitic schist
SMC-14-053b	Migmatitic sil, crd, and grt bearing ms-bt semipelitic gneiss
SMC-13-127	Migmatitic hc-and ms-bearing crd-bt-sil-grt metapelitic gneiss
SMC-13-128	Migmatitic grt-sil-ms-bt metapelitic gneiss
SMC-13-116	Migmatitic sil-bearing ms-bt-grt metapelitic gneiss
SMC-13-118	Migmatitic grt-ms-sil-bt metapelitic gneiss
SMC-13-101	Migmatitic ms-bearing sil-grt-bt semipelitic gneiss
SMC-13-119	Migmatitic ms-bearing sil-grt-bt metapelitic gneiss
Basin	
SMC-14-031	Migmatitic grt-bt-sil metapelitic schist
SMC-15-025a	Migmatitic grt-sil-ms-bt metapelitic gneiss
SMC-14-039	Migmatitic grt-bearing sil-bt-ms metapelitic gneiss
Goat Lake	
SMC-14-034	Migmatitic grt-sil-bt metapelitic schist
SMC-14-035	Migmatitic grt-sil-ms metapelitic schist
SMC-14-027	Migmatitic sil-bearing bt-ms metapelitic gneiss

Major differences between the samples are the relative abundances of quartz to plagioclase. Samples from near Thompson Peak, with the exception of SMC-13-130, contain ~20% higher modal amounts of plagioclase than samples collected north of Thompson Peak (Table 6). Samples collected in the basin contain generally contain higher modal amounts of quartz than those collected near Thompson Peak.

Textures

SMC samples display both gneissic and schistose textures. Eleven semipelitic and metapelitic gneisses contain an abundance of granoblastic quartz and plagioclase. Quartz and plagioclase meet at ~120° grain boundaries (Fig. 9). Plagioclase displays polysynthetic twinning. Some quartz exhibits sutured grain boundaries. Quartz also displays undulose and checkerboard extinction. Loosely foliated to non-foliated blocky biotite occurs at grain boundaries of quartz and plagioclase (Fig. 9). Ilmenite occurs throughout granoblastic regions. Included in granoblastic plagioclase are some fine sillimanite needles (<20 μm).

Two gneisses, SMC-13-053b and SMC-13-127, contain cordierite after sillimanite, with cordierite and muscovite overprinted onto large sillimanite patches in a granoblastic matrix. Hercynite is included in sillimanite in these patches. Cordierite is altered almost fully to pinite. These samples were not considered further in this study, due to the presence of low temperature phases.

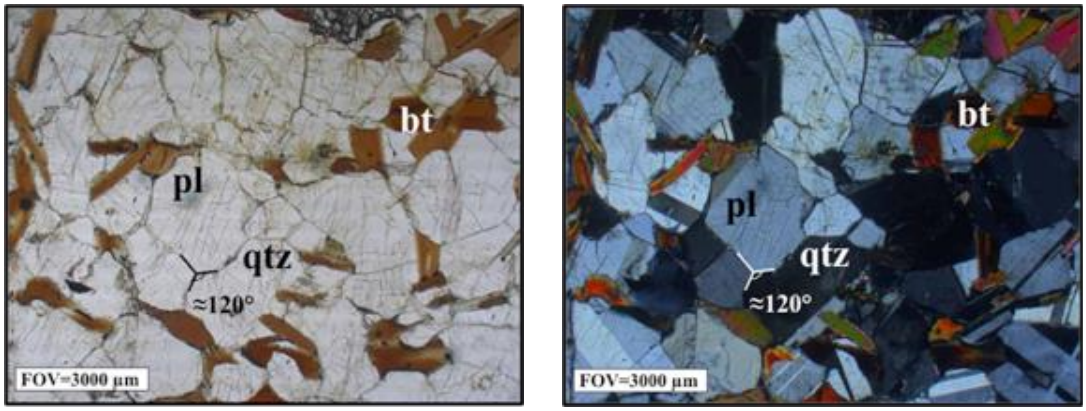

Figure 9: Photomicrographs, PPL (left) and XPL (right), of SMC-13-127, displaying granoblastic quartz and plagioclase meeting at ~120° grain boundaries

Garnet in gneisses has a unique morphology compared to schists. Garnet in gneisses occurs as embayed poikiloblasts that include matrix minerals, as well as sparse zircon and monazite. In some grains, inclusions are most heavily concentrated at the core of the garnet (Fig. 10). The rims of garnet are scalloped and commonly replaced by coarse-grained biotite and plagioclase.

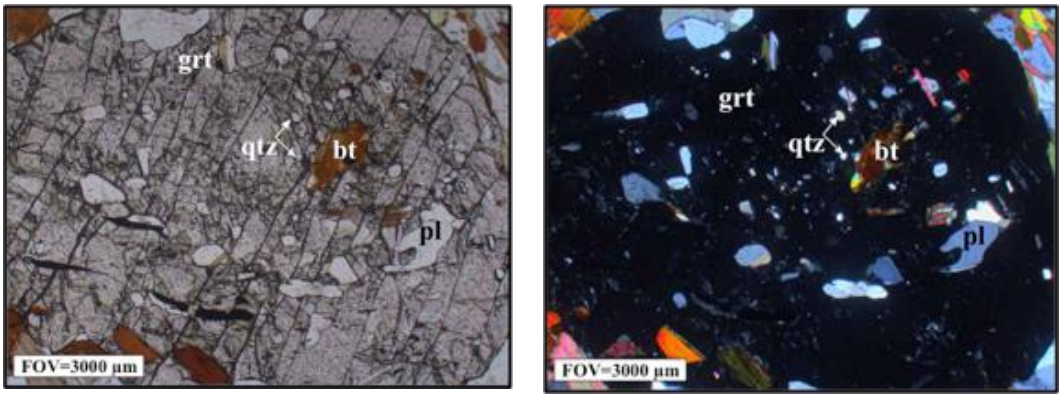

Figure 10: Photomicrograph, PPL (left) and XPL (right), of SMC-13-119, poikiloblastic grt with an inclusion-rich core overprinting the granoblastic

Unlike semipelites, metapelitic gneisses contain continuous layers of foliated sillimanite and biotite (Fig. 11). These layers sharply contact granoblastic regions. Sillimanite occurs commonly as coarse and needlelike but also as fibrolite. Foliated

biotite includes abundant monazite and zircon. Randomly oriented, coarse-grained muscovite overprints foliation.

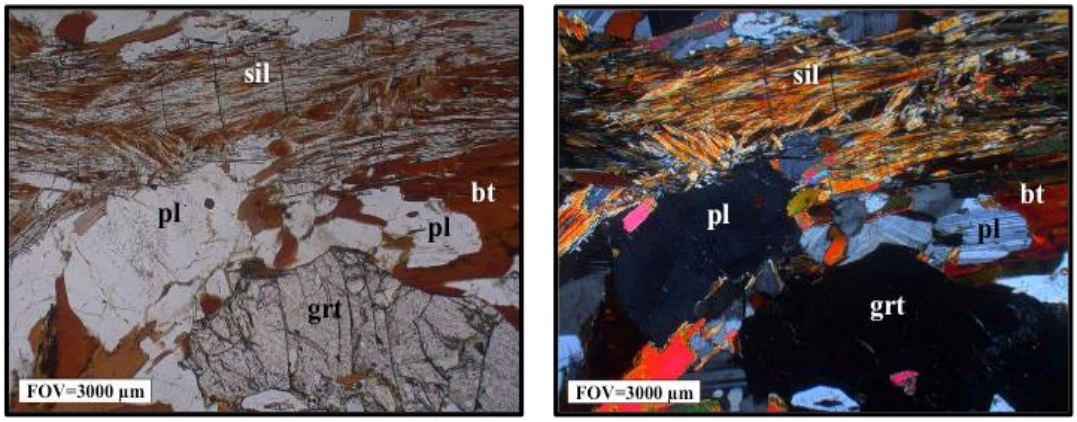

Figure 11: Photomicrograph, PPL (left) and XPL (right), of SMC-13-118, foliated sil and bt in granoblastic matrix with grt porphyroblasts.

Three metapelitic schists contain greater than 50% foliated/crenulated biotite and sillimanite. Foliation wraps around abundant garnet porphyroblasts (Table 6; Fig. 13). Garnet in schists is augen shaped and has rims of coarse-grained biotite, plagioclase, and quartz (Fig. 12). Lineated inclusions of sillimanite and quartz in garnet occur at an angle to foliation (Fig. 13). Randomly oriented muscovite crosscuts foliation and replaces foliated minerals. Minor granoblastic plagioclase and quartz occurs in some schists.

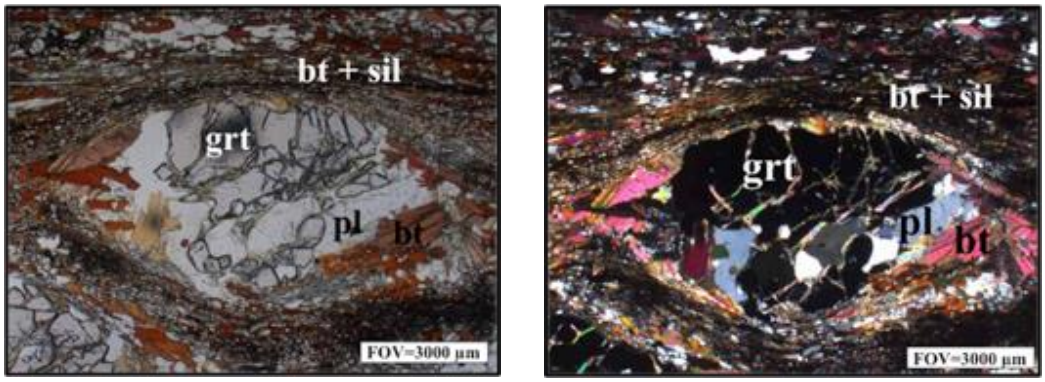

Figure 12: Photomicrograph, PPL (left) and XPL (right), of SMC-14-034, foliation wrapping around an augen-shaped grt porphyroblast that is partially replaced by bt and pl.

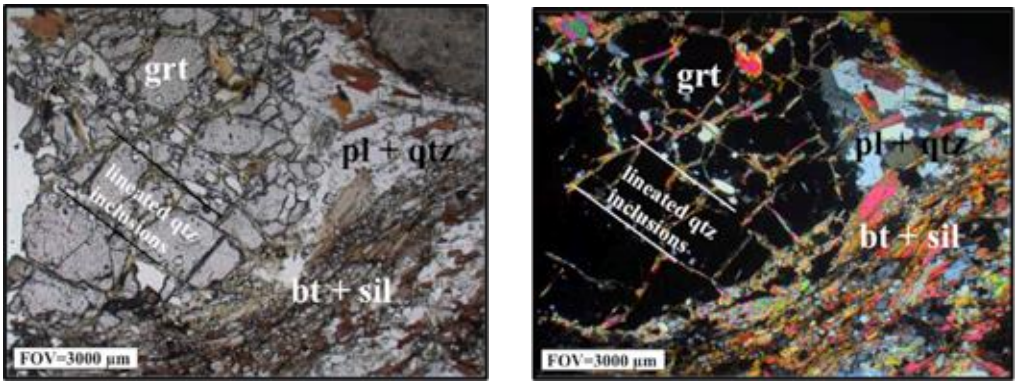

Figure 13: Photomicrograph, PPL (left) and XPL (right), of SMC-13-034, lineated qtz inclusions in grt wrapped in foliation.

SMC metapelitic schists vary in the relative modes of biotite and muscovite (Table 6). Two schists, SMC-14-027 and SMC-14-035, contain abundant, foliated muscovite with lesser biotite and sillimanite (Table 6). Some coarse muscovite overprints biotite and sillimanite and crystallized at a different foliation direction to the dominant foliation (Fig. 14). Muscovite-rich layers are intercalated with quartz ribbons.

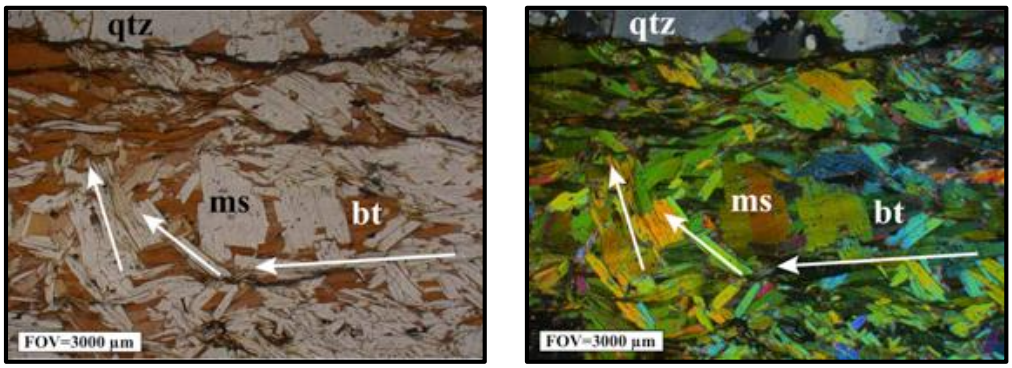

Figure 14: Photomicrograph, PPL (left) and XPL (right), of SMC-14-035, rotated foliation direction of ms and bt.

Evidence of melt

All SMC samples are interpreted as migmatites due to textural evidence of melt. Lenticular leucosomes in schists (Fig. 15) composed of plagioclase and quartz are indicative of muscovite-dehydration melting (muscovite + plagioclase + quartz = melt + alkali-feldspar + sillimanite; e.g. Spear et al., 1999; Anenburg and Katzir, 2013). This

reaction is the first major melt producing reaction aluminous gneisses undergo during prograde metamorphism. It produces modal amounts of melt proportional to ~70% of the original amount of muscovite (e.g. Spear et al., 1999).

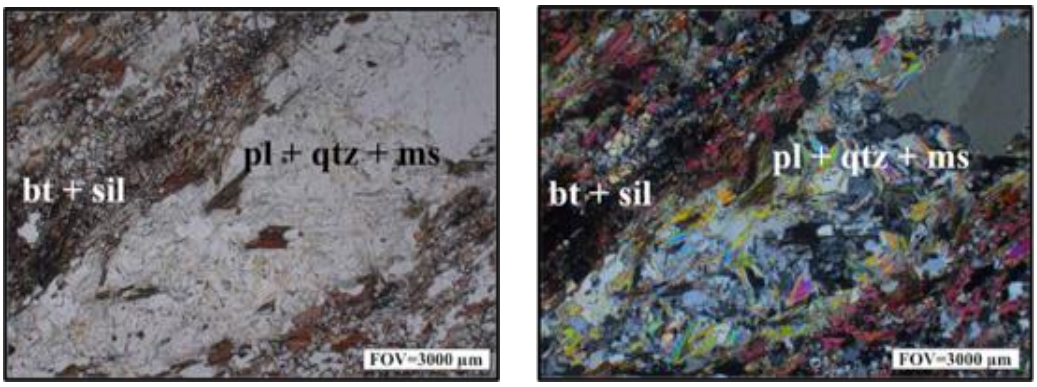

Figure 15: Photomicrograph, PPL (left) and XPL (right), of SMC-14-034 leucosome of pl and qtz with crosscutting ms inclusions in bt and sil matrix.

Myrmekites in leucosomes and in the granoblastic matrix of gneisses are also indicative of muscovite dehydration-melting (Fig. 16; e.g. Anenburg and Katzir, 2013). The formation of myrmekites occurs during melt crystallization. Alkali feldspar is consumed during myrmekitization by the reaction alkali feldspar + sillimanite + H_2O = muscovite + quartz, explaining the lack of alkali feldspar in myrmekites (e.g. Brown, 2002; Anenburg and Katzir, 2013). This reaction is responsible for the formation of quartz-muscovite symplectites, which are found in close proximity to myrmekites in almost all SMC samples (Fig. 15; 17; e.g. Petrík and Janák, 2002; Anenburg and Katzir, 2013).

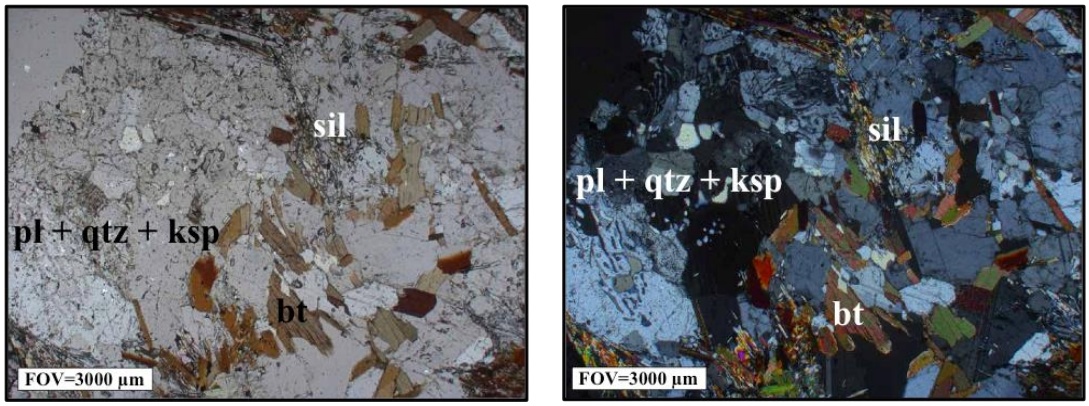

Figure 16: Photomicrograph, PPL (left) and XPL (right), of SMC-14-031, myrmekites composed of pl, qtz, and ksp.

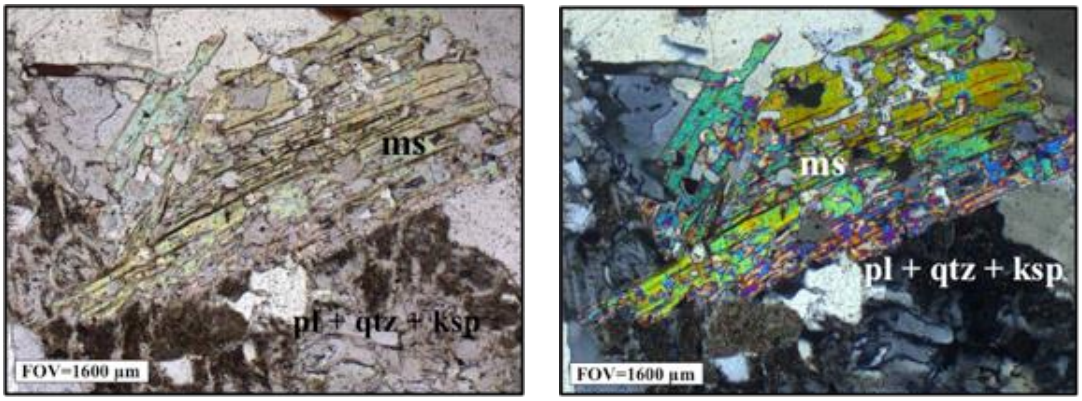

Figure 17: Photomicrograph, PPL (left) and XPL (right), of SMC-14-039, ms symplectite with quartz surrounded by myrmekites.

Peak conditions are interpreted to be above the P-T stability range of muscovite due to abundant melt textures. Crosscutting muscovite in the matrix of SMC aluminous gneisses is post deformational and likely formed during rehydration in the muscovite stability field at post peak P-T conditions.

Whole rock geochemical analysis:

Whole rock geochemical data for major and minor elements was obtained for eight SMC aluminous gneisses (Table 8). Whole rock data is used to predict mineral assemblages over a range of P-T conditions using mineral assemblage diagrams and to provide information on the protolith(s) of the samples.

Table 8: Samples analyzed for whole rock geochemical data

Sample #	Rock type
SMC-13-130	Migmatitic ms-grt-sil-bt metapelitic schist
SMC-14-053b	Migmatitic sil, crd, and grt bearing ms-bt semipelitic gneiss
SMC-13-119	Ms-bearing sil-grt-bt metapelitic gneiss
SMC-14-031	Migmatitic grt-bt-sil metapelitic schist
SMC-14-039	Migmatitic grt-bearing sil-bt-ms metapelitic gneiss
SMC-14-034	Migmatitic grt-sil-bt metapelitic schist
SMC-14-035	Migmatitic grt-sil-ms metapelitic schist
SMC-14-027	Migmatitic sil-bearing bt-ms metapelitic gneiss

Major elements

Whole rock geochemistry of SMC aluminous gneisses does not show any trend with geographic location across the length of the SMC (Table 9; Fig. 18). SiO_2 ranges from 39.70 to 54.71 wt. % for all samples except SMC-14-027 and SMC-14-039, which contain higher SiO_2 amounts of 74.43 and 74.59 wt. %, respectively. SiO_2 is inversely proportional to Al_2O_3, TiO_2, FeO, and MgO (Fig. 18). SMC aluminous gneisses contain similar, Al_2O_3 (12.53-33.43 wt. %) and K_2O (2.86-6.82 wt. %). MgO ranges between 1.23 and 3.26 wt. %. FeO shows a larger variation, between 2.78 and 12.29 wt. %. SMC-13-130 and SMC-14-035 contain the highest K_2O of 5.47 and 6.82 wt. %, and highest Al_2O_3 of 32.92 and 33.43 wt. %. SMC-14-053a and SMC-13-119 contain higher CaO (2.43 and 3.09 wt. %) and Na_2O (2.71 and 3.49 wt. %) values than all other samples, which range from 0.16 to 1.62 wt. % CaO and 0.32 to 1.67 wt. % Na_2O (Table 9, Fig. 18). All three samples collected from near Goat Lake contain similar low CaO (0.16-0.32) and Na_2O (0.32-0.74).

Table 9: Whole rock geochemistry of major elements in wt. % and trace elements in ppm oxides of SMC aluminous gneisses

				Headwall		Basin			Goat Lake
Sample*	NASC**	SMC-13-119	SMC-13-130	SMC-14-053a	SMC-14-039	SMC-14-031	SMC-14-027	SMC-14-034	SMC-14-035
SiO_2	64.8	53.2	39.7	54.71	74.59	42.07	74.43	54.22	49.49
TiO_2	0.7	0.98	1.36	1.13	0.64	1.41	0.66	1.04	1.05
Al_2O_3	16.9	22.42	32.92	23.26	12.53	33.43	12.8	26.61	23.88
FeO*	5.67	9.13	12.19	7.95	4.72	12.29	2.78	9.42	10.02
MnO	-	0.22	0.4	0.15	0.08	0.33	0.02	0.15	0.22
MgO	2.86	2.76	3.26	2.38	1.23	2.87	2.06	2.42	2.54
CaO	3.63	3.09	0.57	2.43	0.19	1.62	0.26	0.32	0.16
Na_2O	1.14	3.49	1.14	2.71	0.66	1.67	0.67	0.32	0.74
K_2O	3.97	3.12	5.47	3.07	2.86	2.84	3.97	3.36	6.82
P_2O_5	0.13	0.08	0.04	0.05	0.04	0.07	0.04	0.06	0.07
Sum	99.8	98.49	99.24	97.83	97.55	98.61	97.68	97.92	95
LOI %	-	0.83	2.21	1.55	1.56	1.22	1.99	1.47	3.61
Ni	58	49.99	-	49.2	28.45	37.54	22.92	23.42	33.89
Cr	125	133.38	-	146.92	86.94	204.46	172.5	72.42	162.33
Sc	15	19.27	-	20.06	11.36	37.73	26.08	10.97	24.6
V	130	99.99	-	103.05	64.02	132.02	109.96	91.98	118.66
Ba	636	564.54	-	863.91	412.89	586.07	766.6	359.73	473.94
Rb	125	158.08	-	152.45	139.7	155.51	164.11	139.9	450.53
Sr	142	365.46	-	230.2	68.67	209.82	71.33	63.13	79.63
Zr	200	242.95	-	407.65	174.09	410.96	166.77	388.28	154.03
Y	35	37.05	-	44.76	25.49	65.13	41.89	34.88	79.14
Nb	13	21.04	-	23.71	11.36	26.91	18.57	15.12	51.38
Ga	-	27.07	-	31.12	16.40	42.22	32.90	17.98	42.88
Cu	-	5.93	-	12.25	2.77	5.46	12.75	0.99	25.98
Zn	-	128.34	-	128.93	67.29	94.87	123.01	66.89	132.59
Pb	12	26.68	-	25.98	10.08	22.72	8.99	8.2	20.45
La	31	66.69	-	68.76	39.12	85.51	75.38	40.71	126.46
Ce	67	126.37	-	132.98	78.94	169.26	128.14	91.29	241.86
Th	12.3	22.82	-	26.48	13.24	32.66	22.92	16.6	36.75
Nd	27.4	53.25	-	54.93	32.6	73.03	56.71	37.54	98.9
U	2.7	3.56	-	3.56	1.88	5.56	3.16	3.75	11.26

*Samples listed from south to north

** North American Shale Composite (NASC; Condie, 1993) for comparison.

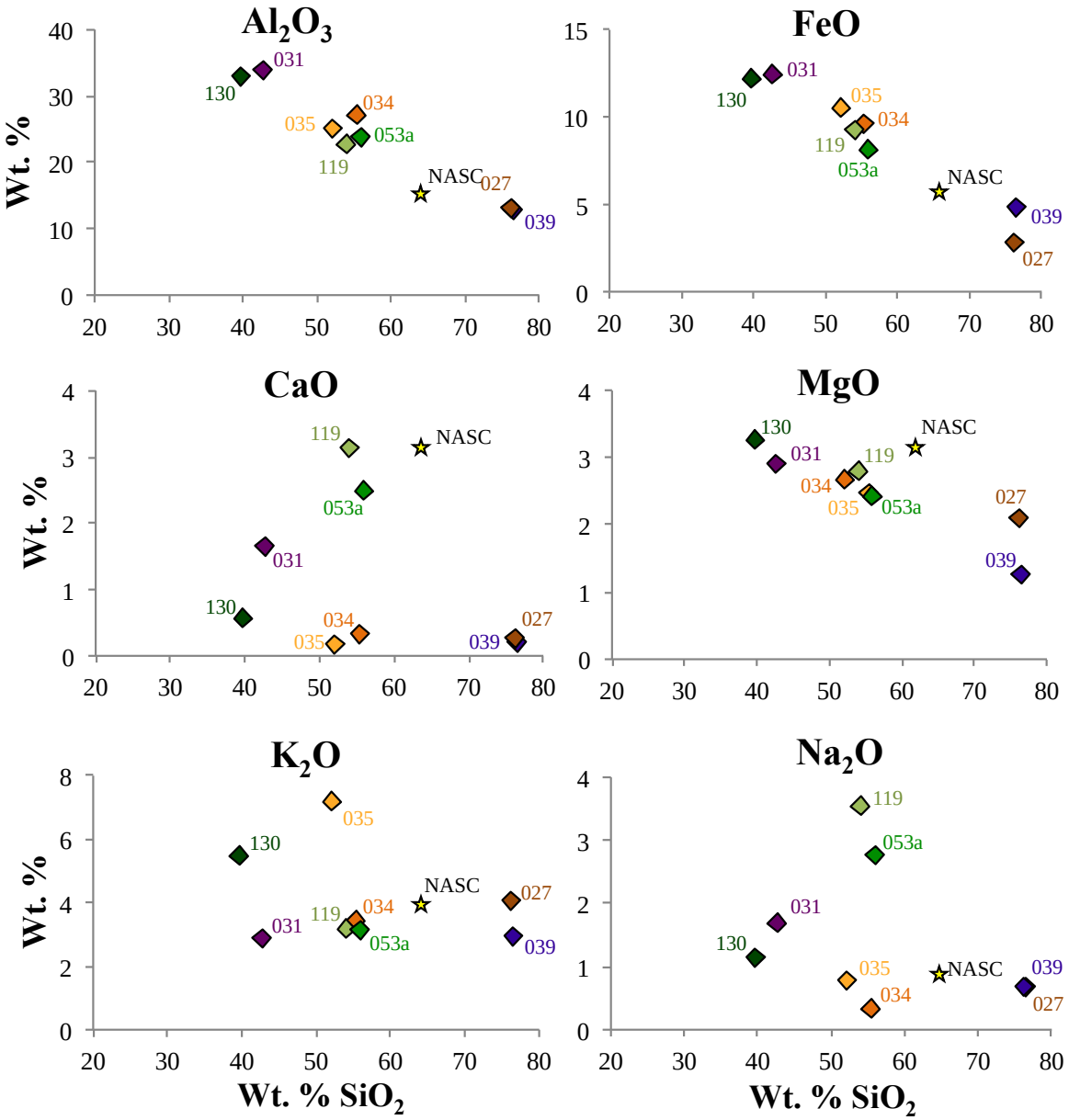

Figure 18: Weight percent oxides of major elements as a function of SiO_2 for SMC aluminous gneisses. Marker color reflects location: Headwall samples-green, Basin samples-purple, and Goat Lake samples-orange. North American Shale Composite (NASC) is starred (values for NASC from Condie, 1993).

Whole rock geochemistry of SMC aluminous gneisses can be compared to modern analogs such as North American Shale Composite (NASC) as a reference, which contains similar major element concentrations (Condie, 1993; Table 9; Figs. 18, 19). The greatest deviations from NASC data are for CaO and Na_2O (Fig. 19). All samples are

depleted in CaO and P_2O_5 relative to NASC (Fig. 19). The degree of CaO depletion is strongly correlated to the degree of Na_2O enrichment and loosely correlated to MgO enrichment (Fig. 19). All but three samples, SMC-13-119, SMC-13-053a, and SMC-14-031, are depleted in Na_2O relative to NASC and these samples also have the strongest CaO depletions. SiO_2 relative to NASC is inversely correlated to TiO_2, Al_2O_3, and MgO, FeO in all SMC samples (Fig. 19). All but two samples, SMC-14-027 and SMC-14-039, are enriched in TiO_2, Al_2O_3, and FeO and depleted in SiO_2 relative to NASC. SMC-14-027 and SMC-14-039 are enriched in SiO_2 relative to NASC and depleted in TiO_2, Al_2O_3, and FeO (Fig. 19). All but two samples, SMC-14-035 and SMC-13-130, are slightly depleted in K_2O relative to NASC, but the ratio is very close to one. Headwall samples and one basin sample, SMC-14-039, show the best correlation to NASC (Fig. 18). Comparison of the bulk rock geochemistry of SMC aluminous gneisses to NASC provides a reference to assess the protolith of the samples.

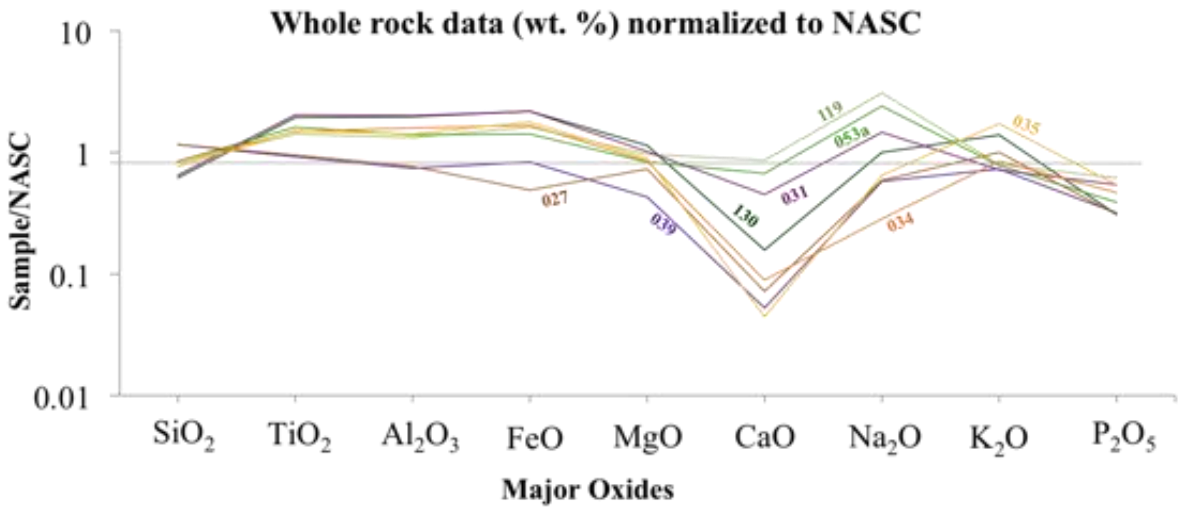

Figure 19: Bulk rock composition of SMC aluminous gneisses in weight percent oxides normalized to NASC (Condie, 1993; Gieré et al., 2011). Marker color reflects location: Headwall samples-green, Basin samples-purple, and Goat Lake samples-orange.

Trace elements

Trace element data was obtained for seven SMC aluminous gneisses (Table 9). Trace element concentrations in SMC aluminous gneisses show distinct trends with respect to the concentrations of large ion lithophiles (LILEs), high field strength elements (HFSEs), and rare earth elements (REEs).

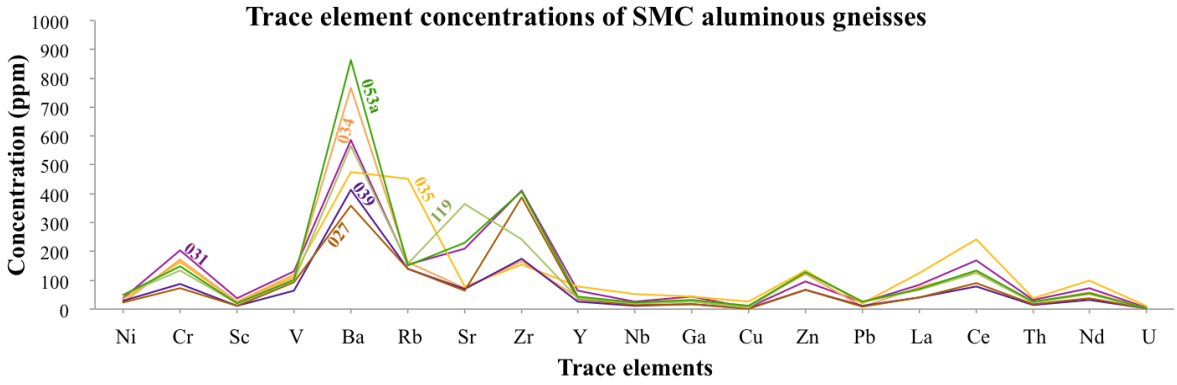

Figure 20: Trace element concentrations of SMC aluminous gneisses (ppm). Marker color reflects location: Headwall samples-green, Basin samples-purple, and Goat Lake samples-orange. Note the high Ba and Zr in some samples.

SMC-14-035 and SMC-14-031 are enriched in Ga, V, the high field strength elements (HFSEs) Nb, Th, and U, and the rare earth elements (REEs) Y, La, Ce, and Nd compared to the other samples (Table 8; Figs. 20, 21). SMC-14-035 also contains the highest Rb and Cu. SMC-14-031 contains the highest Zr. The two most SiO_2 rich samples, SMC-14-039 and SMC-14-027 contain the lowest concentrations of the LILEs - Ba, Rb, and Sr, the HFSEs - Nb, and Th, and the REEs - Y, La, Ce, and Nd (Table 8; Figs. 20, 21). These two samples also contain the lowest Ni, Cr, Sc, V, Ga, Cu, Zn, and Pb. SMC-13-119 contains the highest Ni, Sr, and Pb of all the samples. These concentrations are similar to those of SMC-13-053a. SMC-13-119 and SMC-13-053a contain intermediate amounts of HFSEs and REEs except that SMC-13-053a contains the highest Ba concentrations of 863.91 ppm (Table 8; Fig. 20).

With respect to the NASC, SMC aluminous gneisses contain similar concentration of Sc and V but are enriched in the rare-earth-elements (REEs) Y, La, Ce, and Nd (Table 8; Fig. 21). Concentrations of the large-ion-lithophiles (LILEs) - Sr, and Rb are similar to NASC. The high-field strength elements (HFSE) - Zr, Nb, Th, and U are similar to or slightly enriched relative to NASC (Fig. 21).

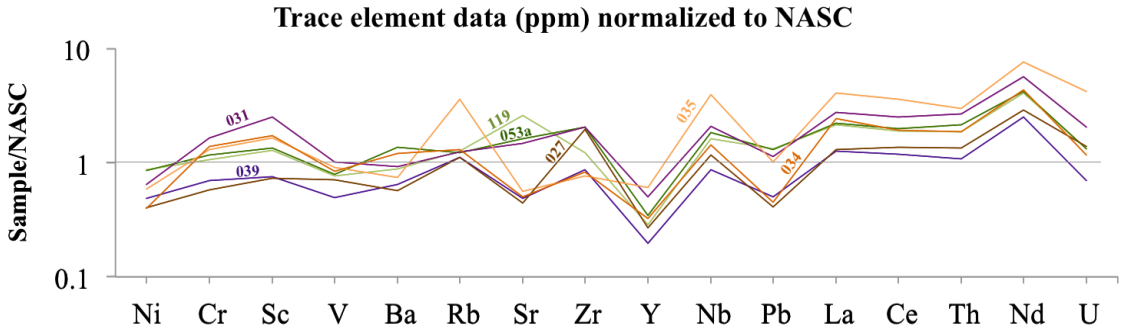

Figure 21: Trace element concentrations of SMC aluminous gneisses (ppm) normalized to the NASC (Condie, 1993). Marker color reflects location: Headwall samples-green, Basin samples-purple, and Goat Lake samples-orange. Note the depletion in Y of all SMC samples.

Mineral chemistry

Mineral chemical data of garnet, biotite, and plagioclase were obtained for eight SMC aluminous gneisses. Four samples were analyzed from near the Headwall in the south, two from in the basin in the central SMC, and two from near Goat Lake in the north. All mineral chemical data are listed in Appendices A-C. Representative mineral chemical data used in geothermobarometry calculations are given in Tables 9-11.

Garnet

Garnet is almandine-rich and grossular-poor. Most grains have Fe, Mg, Mn, and Ca zoning from core to rim (Table 9; Appendix A). In four samples, SMC-13-118, SMC-13-119, SMC-14-031, SMC-14-034, the almandine component increases from core to rim, while the pyrope component decreases from core to rim (Table 9). In two samples,

SMC-13-128 and SMC-13-130, almandine decreases and pyrope increases from core to rim (Table 9). The grossular component generally decreases from core to rim. The spessartine component is generally elevated at the rim of garnet. Two samples, SMC-14-039 and SMC-14-035, show little to no zoning in major elements.

The most grossular-rich garnet is from sample SMC-13-118 collected near Thompson Peak, with the average composition $Alm_{69.6}Pyp_{14.7}Grs_{8.1}Sps_{6.9}$ (Table 9). This sample displays distinct Fe, Mg, Ca, and Mn zoning with the core composition of $Alm_{63.5}Pyp_{15.7}Grs_{13.0}Sps_{6.6}$ gradually changing to $Alm_{73.6}Pyp_{11.7}Sps_{10.1}Grs_{4.3}$ towards the rim (Table 9). Another sample from near Thompson Peak, SMC-13-119, contains garnet with the average core to rim composition $Alm_{72.6}Pyp_{15.6}Grs_{6.4}Sps_{5.1}$ (Table 9). The inner rim has lower almandine component and higher pyrope component than the core, with an average inner-rim composition of $Alm_{70.8}Pyp_{17.7}Grs_{7.6}Sps_{3.4}$. The core contains the highest spessartine component and lowest pyrope component with a composition of $Alm_{74.9}Pyp_{10.5}Sps_{9.98}Grs_{5.0}$. The core analysis point for SMC-13-119 was near a large biotite crystal, which is likely responsible for the elevated almandine and spessartine component. SMC-14-034, collected near Goat Lake, also has increasing almandine from core to rim. The rim has the composition $Alm_{75.8}Pyp_{14.2}Sps_{5.5}Grs_{4.3}$ (Table 9). The core is $Alm_{72.9}Pyp_{20.3}Grs_{4.2}Sps_{2.2}$ while the average of the two rim points is $Alm_{74.4}Pyp_{18.5}Grs_{4.33}Sps_{2.3}$ (Table 9). The grossular component in SMC-14-034 shows no significant zoning. SMC-14-031 has a more pyrope rich and spessartine poor average composition of $Alm_{75.3}Pyp_{16.0}Sps_{3.4}Grs_{4.7}$. The inner rim and rim analyses are homogenous while the core is relatively almandine poor and pyrope and grossular rich, with the composition $Alm_{71.8}Pyp_{18.4}Sps_{2.9}Grs_{5.9}$ (Table 9).

Two garnets from SMC-13-128 and SMC-13-130 have the opposite almandine zoning pattern to the previously described samples, characterized by higher-almandine cores lower-almandine rims. Mg, Mn, and Ca zoning is consistent with SMC-13-118 and SMC-13-119 (Table 9). SMC-13-128 is subtly zoned with the core composition $Alm_{75.8}Pyp_{14.1}Sps_{5.6}Grs_{3.7}$ and a rim composition of $Alm_{74.1}Pyp_{10.2}Sps_{12.0}Grs_{3.5}$ (Table 9). SMC-13-130 has the highest almandine, lowest pyrope, and lowest grossular of all Headwall samples with an average composition of $Alm_{75.8}Pyp_{11.0}Sps_{9.3}Grs_{3.5}$ (Table 9). This sample is also subtly zoned with a core composition of $Alm_{77.3}$ $Pyp_{13.3}$ $Sps_{5.3}$ $Grs_{3.7}$ and an average rim composition of $Alm_{74.4}Sps_{12.2}Pyp_{9.3}Grs_{3.4}$ (Table 9).

Samples SMC-14-039 and SMC-14-035 show little to no Fe, Mg, and Ca zoning from core to rim (Table 9). SMC-14-039 has a core to rim average of $Alm_{75.8}Pyp_{9.5}Sps_{10.3}Grs_{3.3}$ and shows no continuous zoning trends, except for slightly elevated spessartine component in the rim (Table 9). However, the highest almandine content and lowest pyrope content is in the core. SMC-13-035 has an average composition $Alm_{76.5}Pyp_{11.2}Sps_{8.3}Grs_{3.1}$ (Table 9). The highest grossular (2.67 %) content and lowest pyrope content (10.12 %) are in the core but there is no consistent zoning from core to rim for any major elements.

Plagioclase

Plagioclase compositions from SMC aluminous gneisses range from $An_{15.7}$ to $An_{51.5}$ (Table 10; Appendix B). All samples contain less than 1.2% orthoclase component. Matrix plagioclase in SMC-13-118, SMC-13-130, SMC-13-128, SMC-14-039, and SMC-14-035 are oligoclase ($An_{15.7\text{-}29.1}$; Fig. 22). Plagioclase in SMC-13-118, SMC-13-128, and SMC-13-130 is unzoned from core to rim (Table 10). Two matrix grains in SMC-13-118

Table 9: Average compositions of garnet cores inner rims, and rims of SMC aluminous gneisses.

	SMC-13-118			SMC-13-119			SMC-13-128			SMC-13-130			SMC-14-039			SMC-14-031			SMC-14-034			SMC-14-035		
Wt. %	core	inner rim	rim	core	inner rim	rim	core	inner rim	rim	core	inner rim	rim	core	inner rim	rim	core	inner rim	rim	core	inner rim	rim	core	inner rim	rim
SiO_2	37.87	37.77	37.20	36.90	37.73	37.37	37.21	37.25	37.16	37.16	37.00	36.94	37.09	37.20	37.08	37.72	37.48	37.39	37.94	37.66	37.66	36.79	37.21	37.01
Al_2O_3	21.51	21.41	21.21	21.18	21.41	21.21	21.30	21.26	21.13	21.26	21.12	21.11	21.13	21.10	21.06	21.35	21.32	21.29	21.52	21.50	21.45	20.96	21.15	21.02
Fe_2O_3	0.67	0.33	0.06	0.40	0.00	0.00	0.69	0.35	0.06	0.00	0.18	0.00	0.00	0.38	0.23	0.47	0.06	0.40	0.00	0.08	0.31	0.91	0.00	0.32
FeO	28.96	30.94	32.84	33.25	31.89	33.93	34.02	33.84	33.05	34.45	33.78	32.92	34.00	33.71	33.57	32.53	34.05	34.34	33.00	33.42	33.64	33.81	34.14	33.86
MnO	2.95	2.61	4.43	3.94	1.53	2.42	2.47	3.17	5.08	2.33	3.89	5.34	4.24	4.44	4.79	1.29	1.39	1.70	1.00	0.93	1.02	4.15	2.94	4.08
MgO	4.02	4.01	2.92	2.61	4.47	3.57	3.54	3.23	2.62	3.32	2.79	2.31	2.25	2.44	2.37	4.68	4.02	3.77	5.15	4.84	4.71	2.52	3.03	2.66
CaO	4.84	3.47	1.52	1.74	2.68	1.50	1.30	1.32	1.19	1.31	1.16	1.28	1.29	1.45	1.33	2.30	1.70	1.51	1.53	1.55	1.56	1.18	1.18	1.21
Total	100.88	100.58	100.21	100.03	99.72	100.00	100.53	100.42	100.29	99.86	99.94	99.91	100.06	100.76	100.43	100.37	100.02	100.42	100.17	99.99	100.35	100.36	99.67	100.19
Structural formula based on 12 oxygens (apfu)																								
Si	2.98	2.99	2.99	2.98	3.00	3.00	2.98	2.99	2.99	2.99	2.99	2.99	3.00	2.99	2.99	2.99	3.00	2.99	3.00	2.99	2.99	2.97	3.00	2.99
Al	1.98	1.99	2.00	2.00	2.01	2.00	1.99	2.00	2.00	2.01	2.00	2.01	2.01	1.99	2.00	1.98	2.00	1.99	2.01	2.00	1.99	1.97	2.01	1.99
Fe^{2+}	1.91	2.05	2.21	2.25	2.12	2.28	2.28	2.27	2.23	2.32	2.28	2.23	2.30	2.27	2.27	2.16	2.28	2.29	2.18	2.22	2.23	2.29	2.31	2.29
Mn^{2+}	0.20	0.18	0.30	0.27	0.10	0.16	0.17	0.22	0.35	0.16	0.27	0.37	0.29	0.30	0.33	0.09	0.09	0.12	0.07	0.06	0.07	0.28	0.20	0.28
Mg	0.47	0.47	0.35	0.31	0.53	0.43	0.42	0.39	0.31	0.40	0.34	0.28	0.27	0.29	0.28	0.55	0.48	0.45	0.61	0.57	0.56	0.30	0.36	0.32
Ca	0.41	0.29	0.13	0.15	0.23	0.13	0.11	0.11	0.10	0.11	0.10	0.11	0.11	0.13	0.11	0.20	0.15	0.13	0.13	0.13	0.13	0.10	0.10	0.10
Calculated % garnet species																								
Alm	63.52	68.30	73.64	74.85	70.79	75.88	75.84	75.64	74.27	77.31	76.11	74.39	76.74	75.53	75.50	71.84	75.84	76.45	72.80	74.04	74.38	76.15	76.92	76.20
Pyr	15.72	15.76	11.67	10.47	17.70	14.23	14.07	12.85	10.48	13.28	11.20	9.28	9.05	9.75	9.48	18.42	15.96	14.94	20.25	19.11	18.55	10.12	12.15	10.67
Sps	6.55	5.83	10.06	8.98	3.43	5.48	5.58	7.17	11.55	5.30	8.88	12.22	9.69	10.08	10.91	2.88	3.13	3.83	2.22	2.08	2.27	9.47	6.71	9.29
Grs	12.95	9.43	4.28	4.98	7.58	4.30	3.66	3.70	3.37	3.68	3.29	3.66	3.59	3.92	3.67	5.90	4.77	4.09	4.23	4.36	4.33	2.67	3.31	3.18

have an average composition of $Ab_{70.3}An_{29.1}Or_{0.5}$ (Table 10). Three inclusions in garnet; however, are labradorite with an average composition of $Ab_{48.1}An_{51.5}Or_{0.3}$ (Fig. 22; Table 10). Plagioclase in SMC-13-128 has average composition of $Ab_{75.6}An_{23.8}Or_{0.6}$. Plagioclase in SMC-13-130 has an average of $Ab_{78.9}An_{20.2}Or_{0.9}$ (Table 10).

Plagioclase in SMC-14-039 and SMC-14-035 is slightly zoned (Table 10). Two plagioclase grains analyzed in SMC-14-039 have an average composition of $Ab_{83.3}An_{16.3}Or_{0.4}$ (Fig. 22; Table 10). The core values are more anorthitic with the composition $Ab_{81.6}An_{17.7}Or_{0.7}$. Two plagioclase grains analyzed in SMC-14-035 have an average composition of $Ab_{81.5}An_{17.5}Or_{1.0}$ (Table 10). Plagioclase cores in SMC-14-035 are also slightly more anorthitic than rims, with a composition of $Ab_{79.3}An_{19.6}Or_{1.0}$.

Matrix plagioclase in SMC-13-119, SMC-14-031, and SMC-14-034 are andesine ($An_{66.0\text{-}68.6}$; Fig. 22). Plagioclase in SMC-13-119 has slight core to rim zoning (Table 10). Cores from five plagioclase grains have an average composition of $Ab_{66.0}An_{32.1}Or_{0.7}$. Inner rims and rims are largely the same with an average composition of $Ab_{67.3}An_{31.9}Or_{0.7}$. Four inclusions in garnet are more anorthitic in composition: $Ab_{62.7}An_{36.7}Or_{0.5}$ (Fig. 22; Table 10). Core values in SMC-13-119 have 0.69% BaO, whereas the inner rims, rim, and inclusions contain BaO from 0 to 0.23% (Table 10).

Matrix plagioclase in SMC-13-119, SMC-14-031, and SMC-14-034 are andesine ($An_{66.0\text{-}68.6}$; Fig. 22). Plagioclase in SMC-13-119 has slight zoning (Table 10). Cores from five plagioclase grains have an average composition of $Ab_{66.0}An_{32.1}Or_{0.7}$. Inner rims and rims are homogenous with an average composition of $Ab_{67.3}An_{31.9}Or_{0.7}$. Four inclusions in garnet are more anorthitic in composition: $Ab_{62.7}An_{36.7}Or_{0.5}$ (Fig. 22; Table 10). Core

values in SMC-13-119 have 0.69% BaO, whereas the inner rims, rim, and inclusions contain BaO ranging from 0 to 0.23% (Table 10).

Five plagioclase grains analyzed in SMC-14-031 are homogenous from core to rim and contain more anorthitic plagioclase than other samples with the average composition of $Ab_{68.6}An_{30.9}Or_{0.5}$ (Fig. 22; Table 10). Two plagioclase inclusions in garnet in SMC-13-031 are more anorthitic, with an average composition of $Ab_{63.0}An_{36.4}Or_{0.5,}$ than the matrix grains. Five plagioclase grains analyzed in SMC-14-034 are on average $Ab_{66.6}An_{32.3}Or_{1.1}$ with no zoning from core to rim.

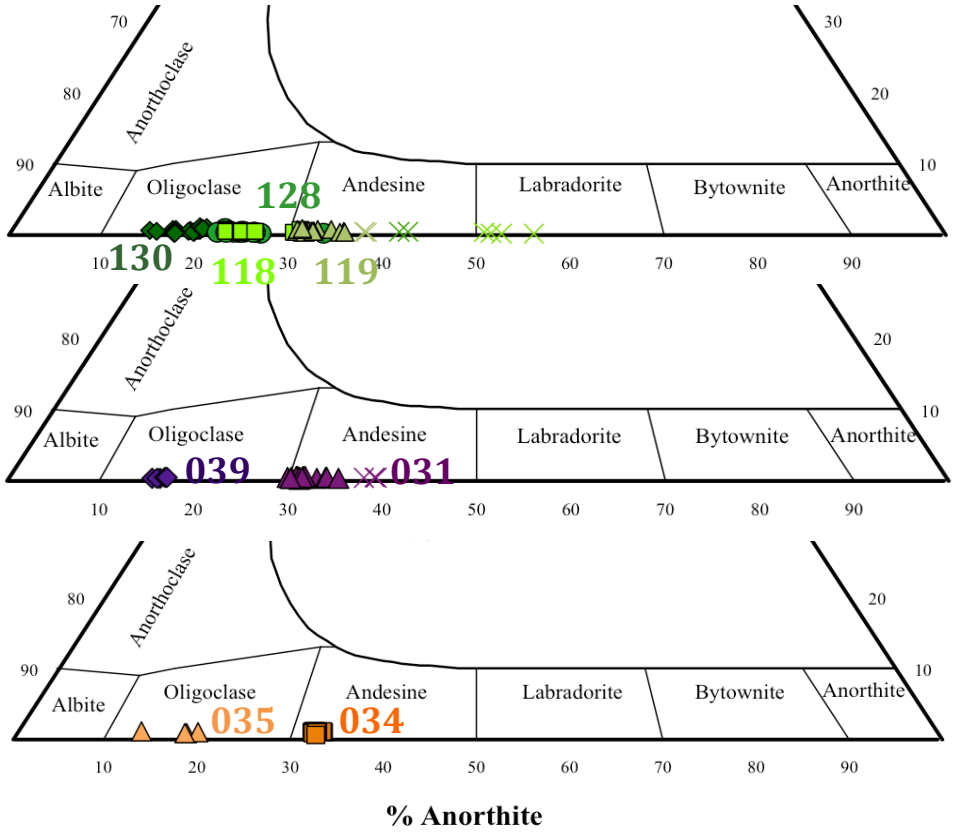

Figure 22: Plagioclase compositions for eight SMC samples plotted on the feldspar classification diagram. K (Or) is at the apex and not shown. Na (Ab) and Ca (An) are along the base. Xs correspond to plagioclase composition for inclusions in garnet. Marker color reflects location: Headwall samples-green, Basin samples-purple, and Goat Lake samples-orange.

Table 10: Compositional averages of plagioclase from SMC aluminous gneisses

	SMC-13-118		SMC-13-119			SMC-13-128	SMC-13-130	SMC-14-039		SMC-14-031		SMC-14-034	SMC-14-035	
Wt. %	matrix	inclusions	core	rim	inclusions	matrix	matrix	core	rim	matrix	inclusions	matrix	core	rim
SiO_2	61.26	55.24	59.89	60.21	58.76	63.74	63.18	64.91	64.95	60.70	59.03	59.70	63.83	63.98
Al_2O_3	24.88	28.75	25.50	25.34	26.07	24.07	23.16	22.85	22.68	25.21	26.09	25.24	23.43	23.12
FeO	0.01	0.08	0.01	0.08	0.10	0.01	0.06	0.01	0.01	0.03	0.06	0.05	0.02	0.05
CaO	6.02	10.56	6.73	6.61	7.60	4.92	4.19	3.47	3.29	6.41	7.53	6.68	4.17	3.89
BaO	0.05	0.01	0.69	0.03	0.06	0.01	0.03	0.03	0.00	0.00	0.03	0.01	0.03	0.01
Na_2O	8.06	5.45	7.64	7.71	7.17	8.64	9.07	9.56	9.71	7.82	7.20	7.55	9.33	9.42
K_2O	0.09	0.06	0.13	0.12	0.08	0.11	0.16	0.08	0.07	0.09	0.08	0.20	0.18	0.15
Total	100.38	100.14	100.57	100.09	99.84	101.50	99.86	100.89	100.70	100.27	100.02	99.43	101.00	100.61
Structural formula based on 8 oxygens (apfu)														
Si	2.60	2.69	2.65	2.68	2.63	2.77	2.80	2.83	2.84	2.69	2.63	2.67	2.79	2.81
Al	1.41	1.32	1.34	1.33	1.37	1.24	1.21	1.18	1.17	1.32	1.37	1.33	1.21	1.20
Fe	0.00	0.00	0.00	0.00	0.00	0.00	0.00	0.00	0.00	0.00	0.00	0.00	0.00	0.00
Ca	0.39	0.31	0.32	0.32	0.36	0.23	0.20	0.16	0.15	0.30	0.36	0.32	0.20	0.18
Ba	0.00	0.00	0.05	0.00	0.00	0.00	0.00	0.00	0.00	0.00	0.00	0.00	0.00	0.00
Na	0.58	0.67	0.66	0.66	0.62	0.73	0.78	0.81	0.82	0.67	0.62	0.65	0.79	0.80
K		0.00	0.01	0.01	0.01	0.00	0.01	0.01	0.00	0.01	0.01	0.01	0.01	0.01
Main feldspar components (%)														
Ab	70.33	48.11	65.98	67.35	62.69	75.56	78.87	81.57	83.91	68.48	63.05	66.38	79.32	80.70
An	29.05	51.54	31.10	31.92	36.74	23.80	20.16	17.74	15.71	31.01	36.44	32.45	19.59	18.43
Or	0.54	0.33	0.73	0.69	0.47	0.62	0.91	0.66	0.38	0.51	0.46	1.15	1.03	0.87

Biotite

Biotite analyses from all samples plot in the siderophyllite field (Fig. 23; Appendix C). Matrix biotite analyses are homogenous within each sample (Fig. 23; Table 11). Magnesium number (Mg/(Mg+Fe)) ranges between 0.34 and 0.41. Total aluminum ranges between 3.35 and 3.47 apfu.

Biotite inclusions in garnet were analyzed in four samples (Table 11). Compositions of biotite inclusions in garnet typically fall outside of the range of matrix biotite (Fig. 23).

Matrix biotite in SMC-13-118 and SMC-13-119 collected near Thompson Peak in the southern SMC are similar (green in Fig. 23; Table 11). Six matrix biotite grains in SMC-13-118 have the average structural formula $(K_{1.81}\square_{0.12}Na_{0.06}Ba_{0.01}Ca_{0.00})(Fe_{2.70}Mg_{1.88}Al_{0.73}Ti_{0.34}\square_{0.33}Mn_{0.02})(Al_{2.64}Si_{5.36})O_{20}(OH_{3.85}F_{0.12}Cl_{0.03})$. Three biotite inclusions in garnet in SMC-13-118 have similar composition as matrix biotite (Fig. 23; Table 11). The average structural formula of six biotite grains in SMC-13-119 is $(K_{1.81}\square_{0.12}Na_{0.06}Ba_{0.01}Ca_{0.00})(Fe_{2.70}Mg_{1.81}Al_{0.79}\square_{0.35}Ti_{0.33}Mn_{0.01})(Al_{2.64}Si_{5.36})O_{20}(OH_{3.87}F_{0.10}Cl_{0.03})$. Three biotite inclusions in garnet SMC-13-119 have compositions with Ti of 0.31 apfu, lower Fe of 2.64 apfu, and higher Mg of 1.90 apfu than matrix grains (Fig. 23; Table 11).

SMC-13-128 and SMC-13-130, also collected near Thompson Peak contain higher Fe and lower Mg than the SMC-13-118 and SMC-13-119 (Fig. 23; Table 11). The average structural formula for four biotite grains in SMC-13-128 is $(K_{1.80}\square_{0.13}Na_{0.06}Ba_{0.01}Ca_{0.00})(Fe_{2.94}Mg_{1.67}Al_{0.76}\square_{0.31}Ti_{0.30}Mn_{0.01})(Al_{2.62}Si_{5.38})O_{20}(OH_{3.84}F_{0.}$

$_{12}Cl_{0.04}$). Two biotite grains in SMC-13-130 have the average structural formula $(K_{1.79}\square_{0.14}Na_{0.06}Ba_{0.01}Ca_{0.00})(Fe_{2.94}Mg_{1.70}Al_{0.78}Ti_{0.32}\square_{0.29}Mn_{0.02})(Al_{2.62}Si_{5.38})O_{20}(OH_{3.74}F_{0.21}Cl_{0.05})$. Biotite inclusions in garnet from SMC-13-130 have lower atomic proportions of Fe of 2.85 apfu and higher atomic proportions of Mg of 1.74 apfu (Fig. 23; Table 11).

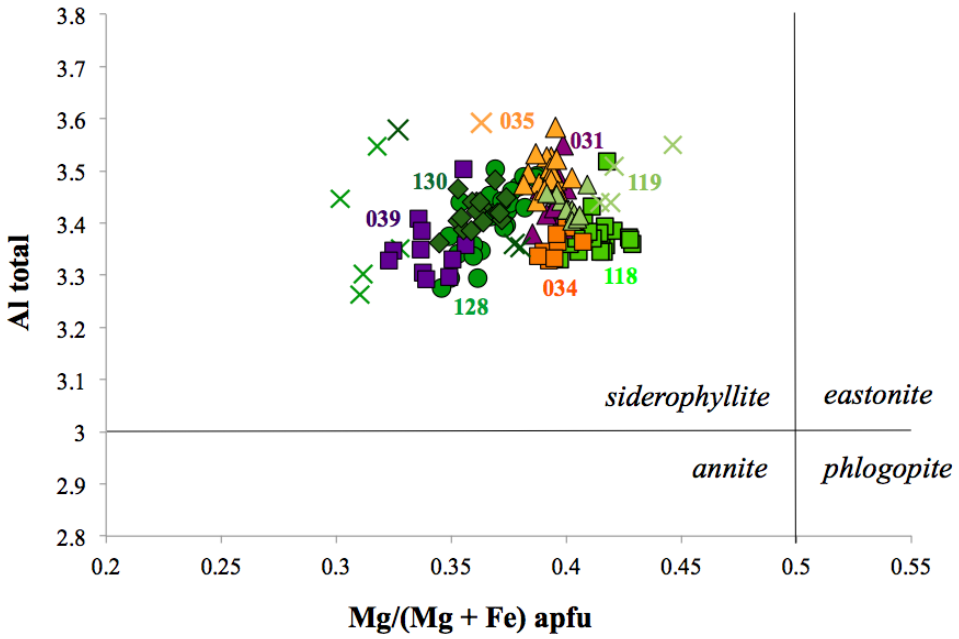

Figure 23: Biotite composition in apfu for SMC aluminous gneisses. Color corresponds to the sample number and location, Thompson Peak samples: green, basin samples, purple, and Goat Lake samples: orange. Xs correspond to compositions of biotite inclusions in garnet, color codes per sample.

SMC-14-039 collected from in the basin has an average structural formula of $(K_{1.78}\square_{0.14}Na_{0.07}Ba_{0.01}Ca_{0.00})(Fe_{3.05}Mg_{1.57}Al_{0.75}\square_{0.31}Ti_{0.29}Mn_{0.02})(Al_{2.60}Si_{5.40})O_{20}(OH_{3.83}F_{0.12}Cl_{0.05}$; Fig. 23; Table 11). The second basin sample, SMC-13-031, has lower atomic proportions of Fe and higher atomic proportions of Mg compared to SMC-14-039 (Fig. 23; Table 11). The structural formula of SMC-14-031 is $(K_{1.79}\square_{0.13}Na_{0.07}Ba_{0.01}Ca_{0.00})(Fe_{2.73}Mg_{1.78}Al_{0.80}\square_{0.35}Ti_{0.33}Mn_{0.01})(Al_{2.64}Si_{5.36})O_{20}(OH_{3.88}F_{0.10}Cl_{0.02}$; Fig. 23; Table 11).

Table 11: Compositional averages of matrix biotite and biotite inclusions in garnet in SMC aluminous gneisses

	SMC-13-118		SMC-13-119		SMC-13-128	SMC-13-130		SMC-14-039	SMC-14-031	SMC-14-034	SMC-14-035	
Wt. %	matrix	inclusions	matrix	inclusions	matrix	matrix	inclusions	matrix	matrix	matrix	matrix	inclusions
SiO_2	34.48	34.31	34.55	34.62	34.38	34.37	34.18	34.35	34.42	34.65	34.74	34.68
Al_2O_3	18.33	18.52	18.75	18.98	18.32	18.50	18.15	18.10	18.78	18.33	18.91	19.18
TiO_2	2.81	2.71	2.91	2.63	2.53	2.13	2.87	2.47	2.81	2.99	1.87	1.33
Cr_2O_3	0.05	0.06	0.04	0.02	0.04	0.04	0.04	0.03	0.04	0.05	0.04	0.05
FeO	20.72	20.69	20.77	20.37	22.45	22.51	21.73	23.20	20.94	21.05	21.53	21.99
MnO	0.15	0.13	0.12	0.08	0.10	0.12	0.16	0.14	0.07	0.08	0.17	0.15
MgO	8.10	8.10	7.90	8.22	7.16	7.33	7.44	6.71	7.67	7.76	7.57	7.47
CaO	0.01	0.01	0.01	0.00	0.00	0.00	0.00	0.00	0.00	0.00	0.00	0.00
BaO	0.21	0.19	0.14	0.20	0.20	0.11	0.15	0.12	0.19	0.06	0.04	0.06
Na_2O	0.20	0.20	0.20	0.19	0.20	0.20	0.18	0.24	0.23	0.18	0.32	0.27
K_2O	9.09	9.09	9.13	9.00	9.00	8.93	9.04	8.88	8.99	9.00	8.94	8.97
Total	98.08	97.94	98.46	98.28	98.32	98.21	97.86	98.19	98.05	98.13	98.09	98.09
Structural formula based on 24 anions (apfu)												
Si	5.36	5.35	5.36	5.36	5.38	5.38	5.36	5.40	5.36	5.39	5.41	5.41
Al	3.37	3.40	3.43	3.46	3.38	3.41	3.36	3.35	3.45	3.36	3.47	3.53
Ti	0.34	0.32	0.33	0.31	0.30	0.25	0.34	0.29	0.33	0.35	0.22	0.16
Cr^{3+}	0.01	0.01	0.01	0.00	0.01	0.00	0.00	0.00	0.01	0.01	0.01	0.01
Fe^{2+}	2.70	2.70	2.70	2.64	2.94	2.95	2.85	3.05	2.73	2.74	2.81	2.87
Mn^{2+}	0.02	0.02	0.01	0.01	0.01	0.02	0.02	0.02	0.01	0.01	0.02	0.02
Mg	1.88	1.88	1.81	1.90	1.67	1.71	1.74	1.57	1.78	1.80	1.76	1.74
Ca	0.00	0.00	0.00	0.00	0.00	0.00	0.00	0.00	0.00	0.00	0.00	0.00
Ba	0.01	0.01	0.01	0.01	0.01	0.01	0.01	0.01	0.01	0.00	0.00	0.00
Na	0.06	0.06	0.06	0.06	0.06	0.06	0.05	0.07	0.07	0.06	0.10	0.08
K	1.81	1.81	1.81	1.78	1.80	1.78	1.81	1.78	1.79	1.79	1.78	1.79

Matrix biotite in sample SMC-14-034 from near Goat Lake has an average structural formula of $(K_{1.79}\square_{0.16}Na_{0.06}Ba_{0.003}Ca_{0.00})(Fe_{2.74}Mg_{1.80}Al_{0.75}\square_{0.35}Ti_{0.35}Mn_{0.01})(Al_{2.61}Si_{5.39})O_{20}(OH_{3.85}F_{0.11}Cl_{0.05}$; Table 11). Matrix biotite in SMC-14-035 has lower atomic proportions of titanium than SMC-14-034. The average structural formula for matrix biotite in SMC-14-035 is $(K_{1.78}\square_{0.12}Na_{0.10}Ba_{0.002}Ca_{0.00})(Fe_{2.81}Mg_{1.76}Al_{0.88}\square_{0.31}Ti_{0.22}Mn_{0.02})(Al_{2.59}Si_{5.41})O_{20}(OH_{3.63}F_{0.35}Cl_{0.02}$; Fig. 23; Table 11). Two biotite inclusions in garnet from SMC-14-035 have lower Ti than the matrix grains of 0.14 and 0.17 apfu, respectively. One inclusion contains higher atomic proportions of Fe of 2.94 apfu and lower atomic proportions of Mg of 1.67 apfu (Fig. 23; Table 11).

P-T determination:

To determine peak temperatures and pressures at which the samples formed, a series of calculations using both whole rock data and mineral chemistry were performed. Temperature estimates were calculated using the titanium-in-biotite geothermometer (TiB; Henry et al., 2005) and the garnet-biotite geothermometer (GB; Holdaway, 2000; Table 12). Pressure estimates were calculated using the garnet-aluminosilicate-plagioclase geobarometer (GASP; Hodges and Crowley, 1985) combined with temperature estimates from GB geothermometry. Pressures were also calculated with the Garnet-biotite-plagioclase-quartz geobarometer (GBPQ Wu et al., 2004; Table 12).

Garnet core, inner rim, and rim analyses were calculated separately and combined with matrix plagioclase core, inner rim, and rim data, respectively, where plagioclase zoning was evident. Averages of matrix biotite analyses used were from biotite in close

proximity to but not touching the garnet used in calculations. Plagioclase and biotite inclusions in garnet were used with spatially similar garnet analyses and calculated separately for determining the potential P-T path.

Garnet-biotite geothermometry

Peak GB temperatures from all SMC samples range between 777 and 665 ± 25°C (Fig. 24; Table 12). GB temperatures calculated are typically the highest when using garnet core analyses (c.f. SMC-13-119 and SMC-14-039; Table 12). The peak temperature of SMC-13-118 (777 ± 25 °C) is the highest recorded temperature for the SMC samples and was calculated using garnet core analyses and matrix biotite. Slightly lower temperatures, 745 to 646 ± 25 °C, were obtained when using garnet inner rim and rim garnet analyses, respectively. Temperatures calculated using data from plagioclase inclusions in garnet produce a similar core to rim trend from 776 to 645 ± 25 °C. The peak GB temperature of SMC-13-119 is 754 ± 25 °C, which was obtained using inner rim garnet data and matrix biotite (Table 12). The GB temperature using garnet core analyses is 709 ± 25 °C and the temperature using rim analyses is 676 ± 25 °C. SMC-13-130 records a GB temperatures from 698-640 ± 25 °C and using two biotite inclusions in garnet combined with garnet inner rim data yield T = 653 ± 25 °C (Table 12).

A sample from in the basin produces peak temperatures using garnet inner rim data and matrix biotite data of 671 ± 25 °C (Fig. 24; Table 12). GB temperatures calculated for the other basin sample, SMC-14-031, decrease towards garnet and plagioclase rims from 765 to 703 ± 25 °C using matrix biotite. GB temperature calculations using two plagioclase inclusions in garnet combined with garnet core data record peak temperatures of 769 and 768 ± 25°C (Fig. 24; Table 12).

Table 12: Geothermobarometry Results

Sample number	GB (± 25°C)	TiB (± 24°C)	GBPQ (± 1.2 Kb)	GASP (± 1.5 Kb)
SMC-13-118				
Core	777	668	10.9	13.5
Inner Rim	745	668	9.1	11.0
Inclusions: b8-10, p2*	776	660	10.6	13.2
Inclusions: b8-10, p3	744	660	8.8	10.6
SMC-13-119				
Core	709	669	5.4	6.7
Inner Rim	754	669	8.1	9.6
Inclusions: p9-10	740	669	7.3	8.7
Inclusions: p11-12	753	669	7.7	9.3
Inclusions: p11-12, b2-4	752	654	7.3	8.9
SMC-13-128				
Core	716	640	5.3	7.2
Inner Rim	687	640	4.2	5.7
Rim	661	640	4.1	5.5
SMC-13-130				
Core	698	608	5.9	7.1
Inner Rim	667	608	5.1	6.2
Rim	640	608	5.3	6.1
Inclusions: b12, 13	653	650	5.1	5.9
SMC-14-039				
Inner Rim	671	633	6.8	7.6
SMC-14-031				
Core	765	662	7.6	9.1
Inner Rim	704	662	5.5	6.7
Rim	703	662	6.5	6.3
Inclusions: p1-3	769	662	9.1	8.4
Inclusions: p4-6	768	662	8.8	8.3
SMC-14-034				
Core	772	672	5.9	7.5
Inner Rim	753	672	5.7	7.2
Rim	744	672	5.6	7.1
SMC-14-035				
Core	633	587	5.1	5.7
Inner Rim	665	587	5.8	6.5
Inclusions: b1	668	474	5.9	6.4
Inclusions: b2	663	529	5.8	6.3

* points listed in Appendix A-C

In SMC-14-034 from Goat Lake, GB temperatures decrease from core to rim from 772 to 744 ± 25 °C (Table 12). In SMC-14-035, however, the inner rim temperature (665 ± 25 °C) is higher than core the temperature (633 ± 25 °C; Fig. 24; Table 12). GB temperatures calculated for biotite inclusions paired with garnet core data are 653 and 631 ± 25 °C and inclusions paired with plagioclase inner rim data are 668 and 663 ± 25 °C (Table 12).

Ti-in-biotite geothermometry

Peak TiB temperatures from all SMC samples range between 669 and 587 ± 24 °C (Table 12). Samples collected near Thompson Peak record a TiB temperature range of 607-669 ± 24 °C (Table 12). Samples in the basin, SMC-14-039 and SMC-14-031, record TiB temperatures for matrix biotite of 633 and 662 ± 24 °C. TiB temperatures calculated for Goat Lake samples are 672 ± 24 °C and 474-587 ± 24 °C (Table 12). TiB calculations yield lower temperature results than GB calculations by up to 100 °C, suggesting the thermometer has been reset and TiB temperatures do not reflect peak temperatures. Another possibility is that high-pressure conditions have reduced the Ti content in biotite, leading to a lower apparent temperature result (Henry et al., 2005).

Garnet-aluminosilicate-plagioclase-quartz geobarometry

Peak GASP pressures for all SMC samples range between 13.5 and 6.5 ± 1.5 kbars (Fig. 24, Table 12). Headwall samples record peak GASP pressure between 13.5 and 7.1 ± 1.5 kbars. SMC-13-118 records peak GASP pressures of 13.5 ± 1.5 kbars using garnet core data and averaged matrix plagioclase data (Table 12). Plagioclase is unzoned. Plagioclase inclusions in the garnet core, inner rim, and rim produces a trend from 13.2 to 5.3 ± 1.5 kbars. GASP pressures for SMC-13-119 are highest (9.6 ± 1.5 kbars) using

garnet and plagioclase inner rim data. Similarly, garnet inner rim data combined with plagioclase inclusions in garnet record GASP pressures of 9.3 ± 1.5 kbars. Pressure calculated using garnet and plagioclase core data is 6.7 ± 1.5 kbars and rim data produces a pressure of 5.7 ± 1.5 kbars (Table 12). GASP pressures using garnet and plagioclase core data are 7.2 ± 1.5 kbars. Inner rim and rim data produce 5.7 and 5.5 ± 1.5 kbars. SMC-13-130 records a peak GASP pressure of 7.1 ± 1.5 kbars using garnet and plagioclase core data. Inner rim and rim data produce 6.2 and 6.1 ± 1.2 kbars (Table 12).

Peak pressures from the samples in the central SMC are 7.6 and 9.1 ± 1.5 kbars (Fig. 24; Table 12). Sample SMC-14-039 records a GASP pressure of 7.6 ± 1.5 kbars using garnet inner rim data and plagioclase core data. For SMC-14-031, GASP pressures decrease when using garnet and plagioclase core to rim data from the peak pressure of 9.1 ± 1.5 kbars to 6.3 ± 1.5 kbars (Table 12). Pressures calculations using two plagioclase inclusions in garnet yield peak GASP pressures of 8.4 and 8.8 ± 1.5 kbars.

For SMC-14-034, GASP pressures decrease between using garnet core to rim data with averaged matrix plagioclase data from 7.5 to 7.1 ± 1.5 kbars (Fig. 24; Table 12). For SMC-14-035, pressure calculated using garnet inner rim and averaged plagioclase provides pressures of 6.5 ± 1.5 kbars. Biotite inclusions paired with inner rim garnet and plagioclase data render higher pressures than when calculated using garnet core data of 6.4 and 6.3 ± 1.5 kbars (Table 12).

Garnet-biotite-plagioclase-quartz geobarometry

Peak GBPQ pressures from SMC aluminous gneisses range between 10.9 and 5.3 ± 1.2 kbars (Fig. 24; Table 12). Headwall samples record peak GBPQ pressures between 10.9 and 5.9 ± 1.2 (Table 12). Averaged matrix biotite and matrix plagioclase combined

with garnet data collected from the core to rim produce GBPQ pressures that decrease from 10.9 to 4.5 ± 1.2 kbars. Biotite and plagioclase inclusions in garnet produce a similar trend, which decreases from 10.6 to 4.2 ± 1.2 kbars. Similar to temperature trends and the GASP pressure trend, GBPQ pressures for SMC-13-119 are highest when calculated using averaged matrix biotite data with plagioclase and garnet inner rim data (8.1 ± 1.2 kbars). Pressure calculated using garnet core data, plagioclase core data, and averaged matrix biotite is 5.4 ± 1.2 kbars. For SMC-13-128, GBPQ pressures using garnet and plagioclase core to rim data with matrix biotite decrease from 7.2 to 5.5 ± 1.2 kbars (Table 12). GBPQ pressure calculated for SMC-13-130 using averaged matrix biotite with garnet and plagioclase core data is 5.9 ± 1.2 kbars. Garnet and plagioclase inner rim data yield lower pressure (5.1 ± 1.3 kbars) than rim data (5.3 ± 1.2 kbars).

GBPQ pressure calculated for SMC-14-039 using garnet and plagioclase inner rim data with averaged matrix biotite is 6.8 ± 1.2 kbars (Table 12). GBPQ pressures for SMC-14-031 are highest using garnet and plagioclase core data with matrix biotite (7.6 ± 1.2 kbars) and lowest using garnet and plagioclase inner rim data with averaged matrix biotite (5.5 ± 1.2 kbars; Table 12). Peak pressure calculations using garnet core data with matrix biotite and plagioclase inclusions in garnet are 8.8 and 9.1 ± 1.2 kbars.

For SMC-14-034, averaged matrix plagioclase, averaged matrix biotite and garnet core to rim data yield temperatures from 5.9 to 5.6 ± 1.2 kbars (Table 12). For SMC-14-035, pressure calculated using garnet core data and averaged plagioclase data (5.1 ± 1.2 kbars) are lower than inner rim pressures (5.8 ± 1.2 kbars; Table 12). Biotite inclusions paired with inner rim garnet and plagioclase data render higher pressures than when calculated using garnet core data of 5.9 and 5.8 ± 1.2 kbars.

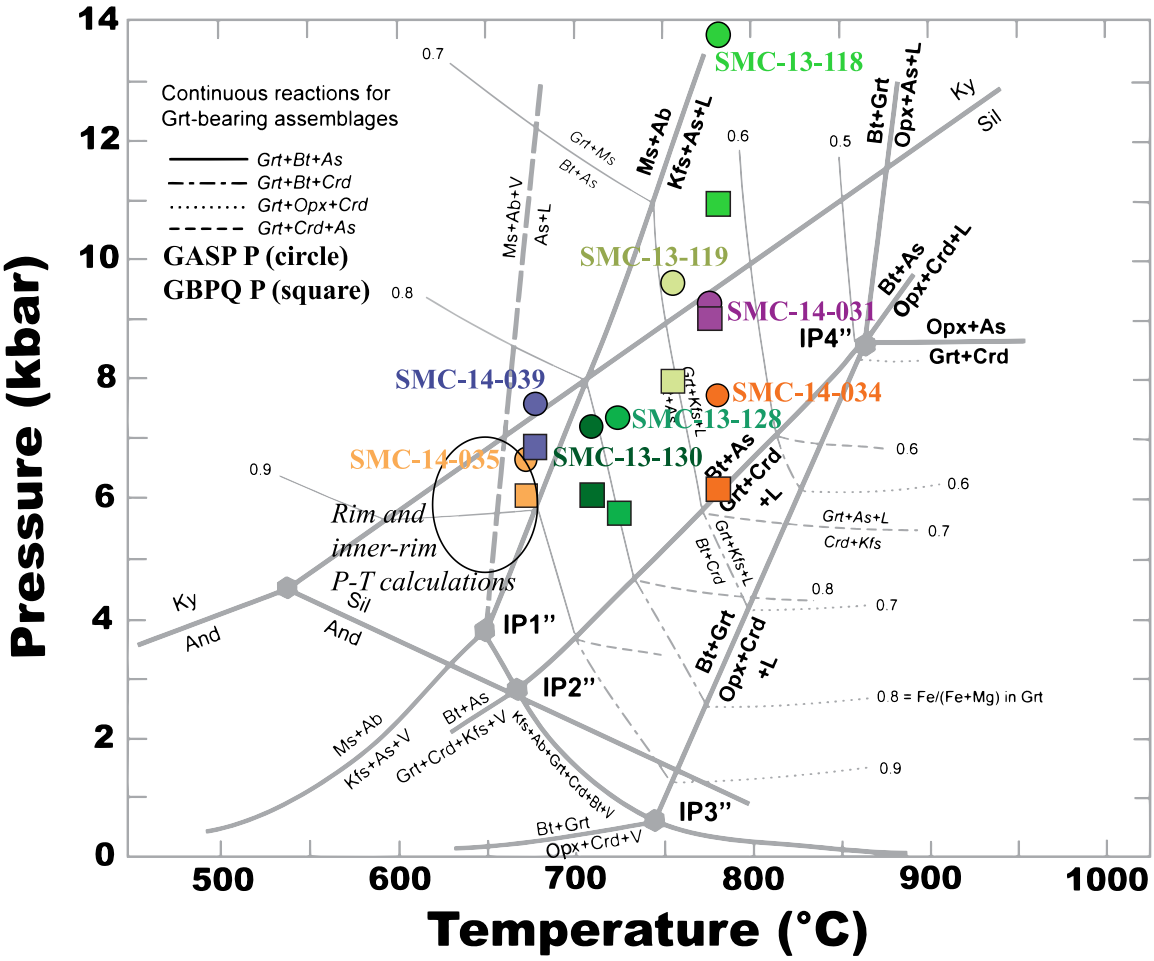

Figure 24: Peak P-T conditions of SMC aluminous gneisses using GB geothermometry (Holdaway, 2001) and GBPQ (squares; Wu et al, 2004), and GASP (circles; Hodges and Crowley, 1985) geobarometry. Data is plotted on a petrogenetic grid for pelitic bulk compositions (Spear et al., 1999).

Mineral assemblage diagrams:

To provide additional constants on the conditions of formation of SMC aluminous gneisses, mineral assemblage diagrams were calculated using Theriak-Domino (de Capitani and Petrakakis, 2010) with whole rock geochemical data (Table 13). Based on petrographic analyses, the eight samples used in phase equilibrium modeling contain the assemblage bt + sil + grt + qtz + ilm + melt ± ms ± fsp (Table 14). Leucosomes, myrmekites, and the presence of muscovite symplectites are interpreted as evidence of melt (e.g. Spear et al., 1999; Anenburg and Katzir, 2013). This melt is a combination of

plagioclase, quartz, and alkali feldspar derived from dehydration melting reactions involving hydrous phases such as biotite and muscovite. Muscovite in all samples overprints the dominant foliation and the peak assemblage and is assumed to be secondary.

Table 13: Whole rock geochemical data in atomic proportions used as for mineral assemblage diagrams.

Sample #	Si	Al	Ti	Fe	Mg	Na	Ca	K	H	ex. Si
SMC-13-119	49.99	24.82	0.69	7.34	3.86	6.36	3.11	3.74	20	15
SMC-13-130	37.14	36.3	0.95	8.89	4.54	2.06	0.57	6.52	20	15
SMC-14-053b	52.05	26.08	0.8	6.43	3.37	4.99	2.48	3.71	20	20
SMC-14-039	73.95	14.64	0.47	3.9	1.83	1.27	0.2	3.61	20	20
SMC-14-031	35.81	33.54	0.9	8.98	3.64	2.75	1.47	3.08	20	15
SMC-14-034	52.49	30.36	0.75	7.74	3.49	0.6	0.33	4.14	20	10
SMC-14-035	48.93	27.82	0.78	8.46	3.37	1.42	0.17	8.60	20	10

Based on mineral assemblage diagrams, the calculated stable assemblage of each sample occurs between 4.5 to 9 kbars and 700 to 850 °C (Table 14). At high pressures, the stable assemblage for each sample is bound by the occurrence of rutile and loss of ilmenite at ~9 kbars and the occurrence of kyanite in lieu of sillimanite. At low pressure (~5 kbars), cordierite becomes stable rather than garnet. At temperatures greater than ~800-850 °C, biotite dehydration is attained for most samples. At temperatures less than ~700 °C, muscovite becomes stable. In each sample, melt is first generated at temperatures between 650 and 700 °C. Garnet becomes stable at pressures between 3 and 5 kbars. The almandine component in garnet for all samples ranges between 65 and 90%. Variations in calculated P-T stability fields are most apparent in the P-T stability ranges of biotite, plagioclase, and quartz.

Table 14: Mineral assemblage diagram results

Location	Sample	Peak assemblage	T (°C)	P (kbars)
Headwall	SMC-13-119	bt + sil + grt + fsp + qtz + ilm + melt	700-850	5-8.5
	SMC-13-130	bt + sil + grt + fsp + qtz + ilm + melt	700-775	4.5-9
	SMC-14-053b	bt + sil + grt + fsp + qtz + ilm + melt	700-850	5-8.5
Basin	SMC-14-039	bt + sil + grt + qtz + ilm + melt	725-850	5-9
	SMC-14-031	bt + sil + grt + fsp + qtz + ilm + melt	700-800	5-8.5
Goat Lake	SMC-13-034	bt + sil + grt + qtz + ilm + melt	725-850	5.5-9
	SMC-14-035	bt + sil + grt + fsp + qtz + ilm + melt	700-850	4-9

Mineral assemblage diagrams calculated for SMC-13-119 and SMC-13-053b are similar (Fig. 25). The peak stable assemblage for both samples is bt + sil + grt + pl + qtz + ilm + melt. This assemblage is calculated to occur between ~5 and 8.5 kbars pressure and between ~700 and 850 °C. Biotite in both calculations becomes unstable above ~800 °C. Quartz becomes unstable at pressures lower than ~5 kbars and temperatures greater than ~800 °C. Plagioclase is stable in all assemblages within the P-T limits of the calculation.

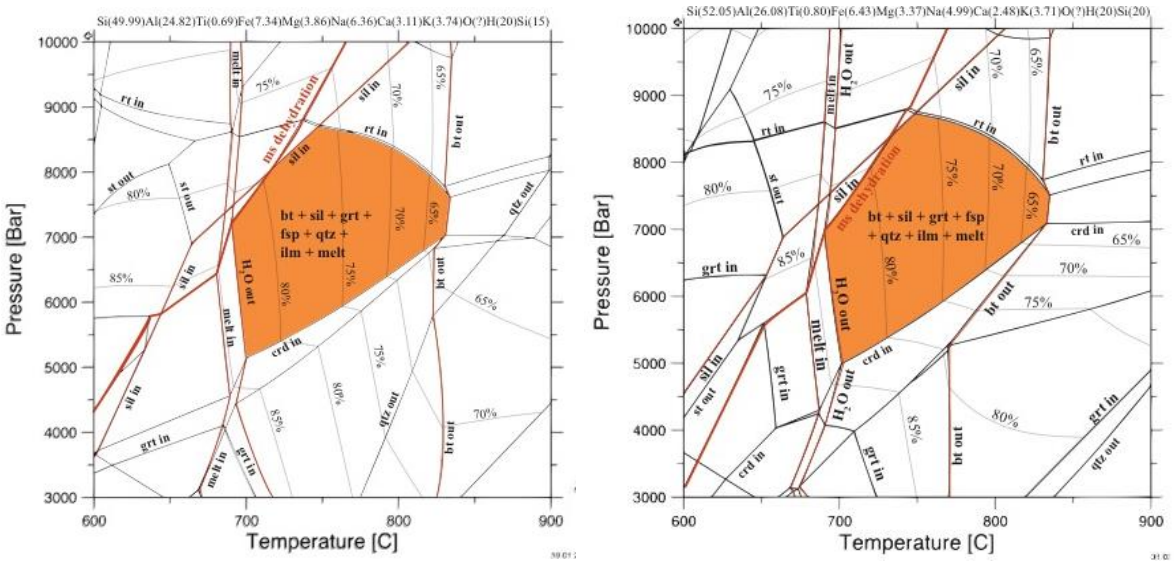

Figure 25: Mineral assemblage diagram for SMC-13-119 (left) and SMC-14-053b (right) with the stable assemblage bt + sil + grt + pl + qtz + ilm + melt highlighted in orange and the atomic proportions used in modeling listed above the plot. Major changes in the stable assemblage are shown in red. Isopleths for the percent almandine in garnet are shown in grey.

The peak assemblage of SMC-13-130 is bt + sil + grt + pl + qtz + ilm + melt (Fig. 26). This assemblage occurs over a broad pressure range of ~4.5 to 8.5 kbars but over a more restricted temperature range of ~700-750 °C. This smaller temperature range is due to the disappearance of quartz at ~750 °C. This sample has the largest calculated P-T stability field of biotite, which is stable in all assemblages within the P-T limits of the model. Plagioclase disappears from the assemblage at temperatures as low as 800 °C. Isolines for almandine component in garnet in the stable assemblage are between 85 and 60% (Fig. 26).

SMC-14-039 has the stable assemblage of bt + sil + grt + ilm + melt (Fig. 27). Plagioclase and potassium feldspar are present only in the melt. Melt is inferred by the presence of myrmekites and muscovite symplectites with quartz. The stability of plagioclase as a separate component bounds the low temperature stability of the

assemblage. This assemblage occurs between ~4.5 and 9 kbars and 725-850 °C. Isolines for the almandine component in garnet are between 90 and 75 %.

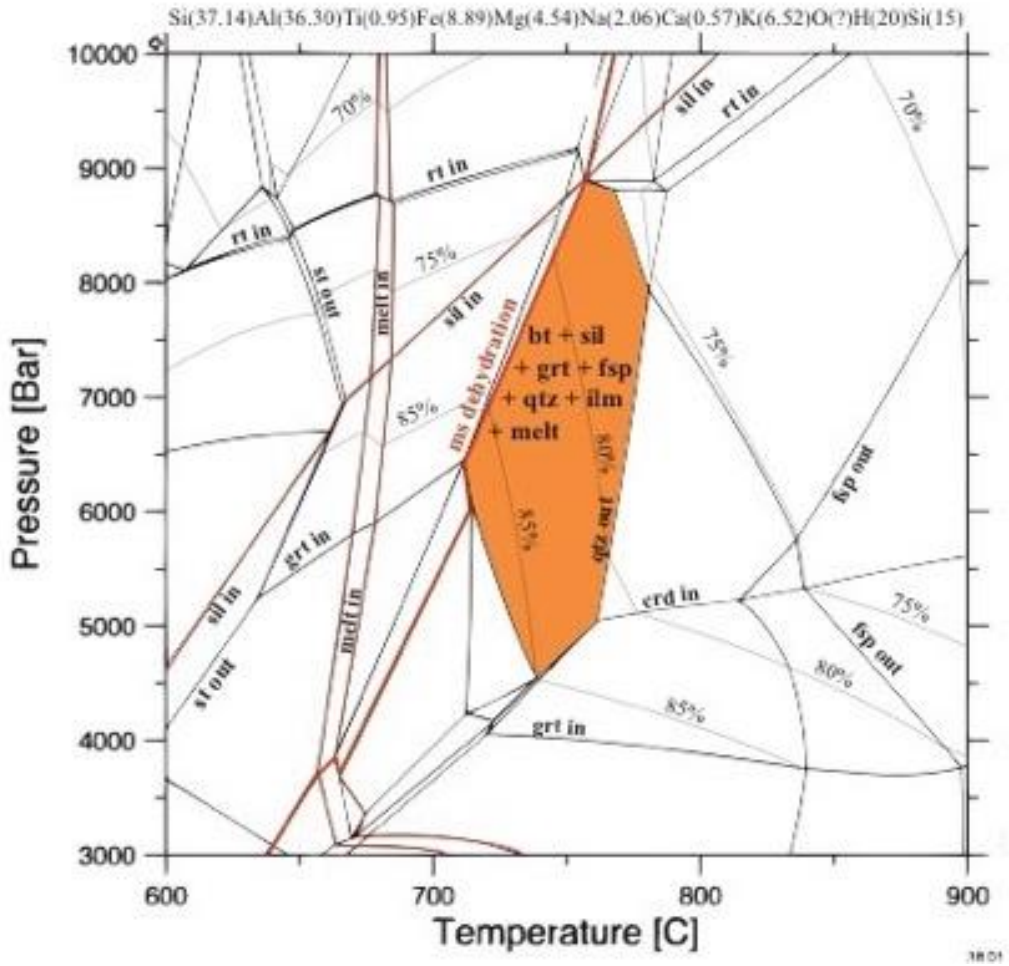

Figure 26: Mineral assemblage diagram for SMC-13-130 with the stable assemblage bt + sil + grt + pl + qtz + ilm + melt highlighted in orange and the atomic proportions used in modeling listed above the plot. Major changes in the stable assemblage are marked in red. Isopleths for the percent almandine in garnet are shown in grey.

SMC-14-031 has the stable assemblage bt + sil + grt + pl + qtz + ilm + melt (Fig. 28). This assemblage is calculated to occur between 5 and 8.5 kbars and 700 and 800 °C. The high temperature limit of this stability field is the disappearance of quartz from the

stable assemblage at ~800 °C. Isolines for the almandine component within the stable assemblage in garnet are between 85 and 65 %.

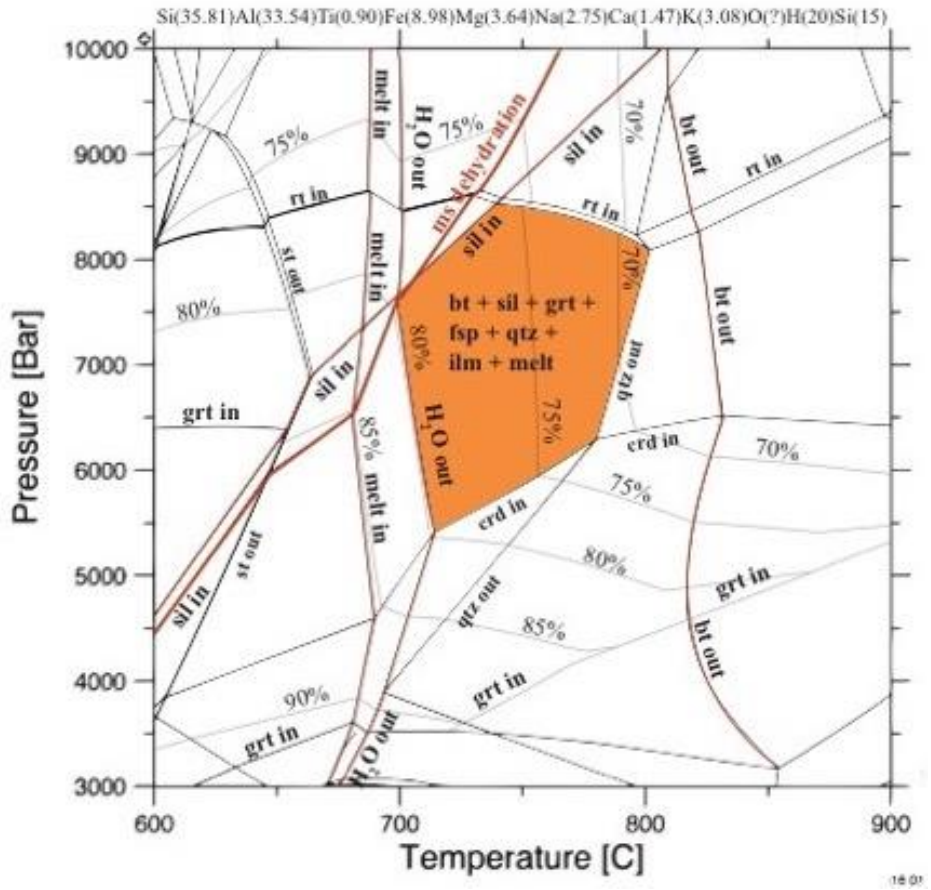

Figure 28: Phase equilibrium model for SMC-14-031 with the stable assemblage bt + sil + grt + fsp + qtz + ilm + melt highlighted in orange. Major changes in the stable assemblage are shown in red. Isopleths for the percent almandine in garnet are shown in grey.

SMC-14-039 has the stable assemblage of bt + sil + grt + ilm + melt (Fig. 27). Plagioclase and potassium feldspar are present only in melt. Melt is inferred by the presence of myrmekites and muscovite symplectites with quartz. The stability of plagioclase as a separate component bounds the low temperature stability of the assemblage. This assemblage occurs between ~4.5 and 9 kbars and 725-850 °C. Isolines for the almandine component in garnet are between 90 and 75 %.

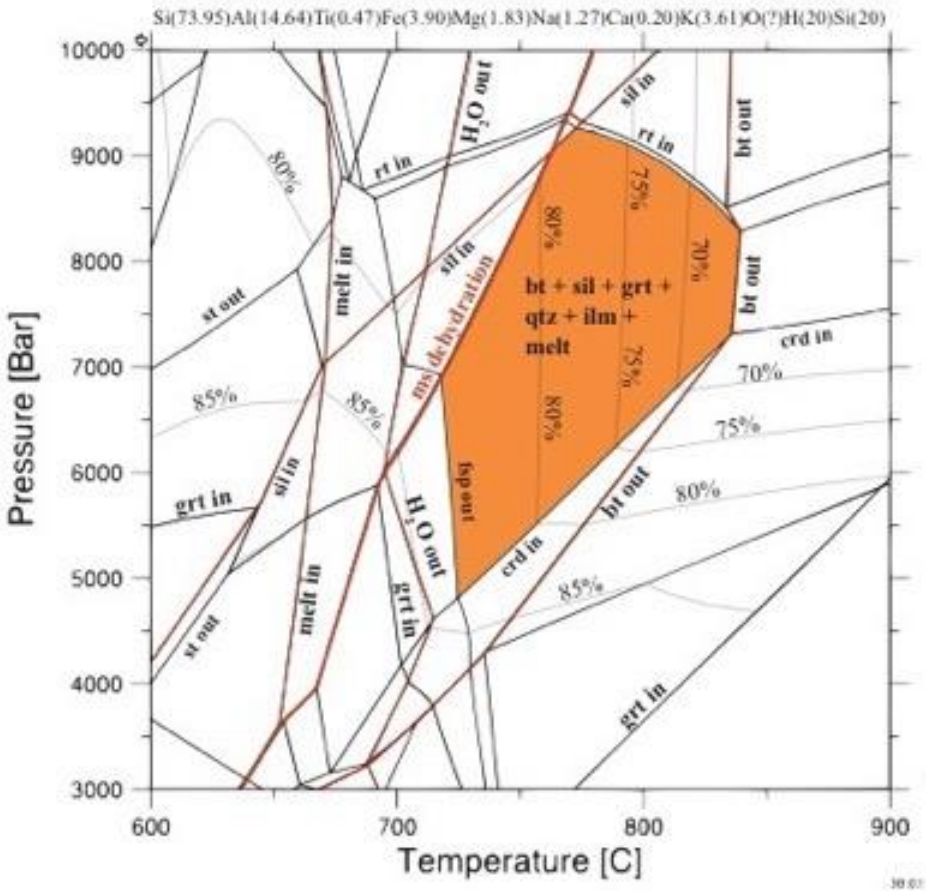

Figure 27: Mineral assemblage diagram for SMC-14-039 with the stable assemblage bt + sil + grt + pl + qtz + ilm + melt highlighted in orange. Major changes in the stable assemblage are shown in red. Isopleths for the percent almandine in garnet are shown in grey.

SMC-14-034 contains the stable assemblage bt + sil + grt + qtz + ilm + melt (Fig. 29). Plagioclase and alkali feldspar are only present in the calculated melt. Plagioclase as a separate component becomes unstable at temperatures as low as 700 °C. The calculated stable assemblage for this sample occurs between ~4.5 and 9 kbars and 725 and 850 °C. Isolines for the almandine component in garnet are between 80 and 70 %.

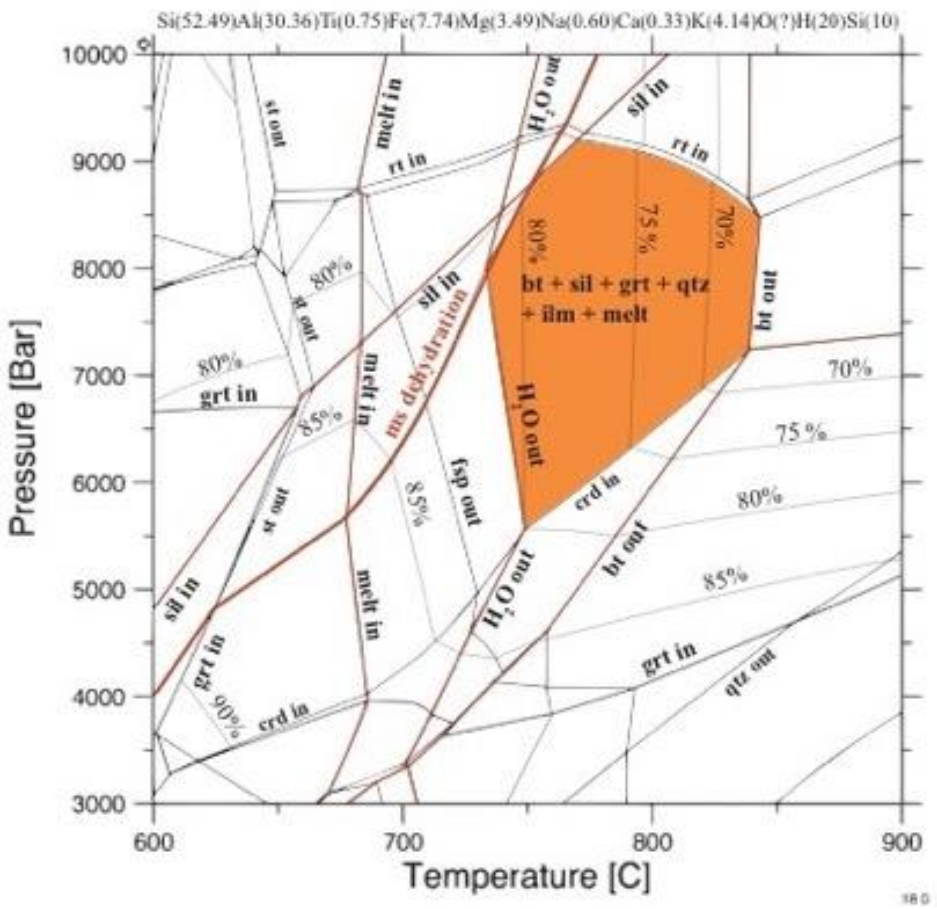

Figure 29: Phase equilibrium model for SMC-14-034 with the stable assemblage bt + sil + grt + fsp + qtz + ilm + melt highlighted in orange. Major changes in the stable assemblage are shown in red. Isopleths for the percent almandine in garnet are marked shown in grey.

SMC-14-035 is different from previous samples because it contains abundant muscovite. However, textural analysis indicates that the muscovite formed after the peak of metamorphism. The stable assemblage is bt + sil + grt + pl + qtz + ilm + melt (Fig. 30). Alkali feldspar is stable up to ~700 °C, but no alkali feldspar occurs in this sample. The calculated stable assemblage for this sample occurs between ~4 and 9 kbars and ~700 and 850 °C. Isolines for the almandine component in garnet are between 70 and 80%.

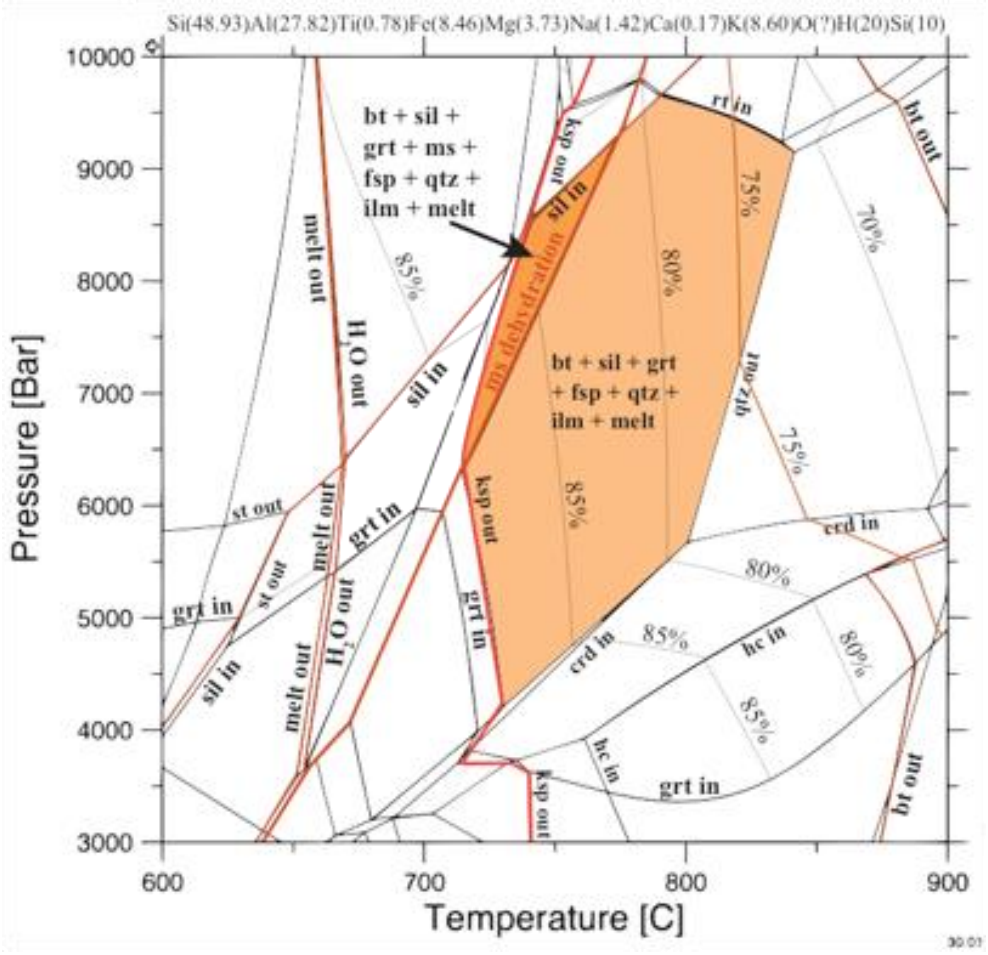

Figure 30: Mineral assemblage diagram for SMC-14-035 with the stable assemblage bt + sil + grt + pl + qtz + ilm + melt highlighted in light orange. The stability field of ms is in dark orange. Major changes in the stable assemblage are shown in red. Isopleths for the percent almandine in garnet are shown in grey.

DISCUSSION

Mineral assemblages of pelitic compositions constrain the P-T conditions with the aid of petrogenetic grids and detailed petrography. The stable peak mineral assemblage for each sample is dominated primarily by biotite, sillimanite, and garnet, indicating conditions above muscovite stability, within the sillimanite zone and below the discontinuous biotite dehydration-melting reaction (e.g. bt + sil + pl + qtz = grt + crd/opx + liquid; Fig. 31; Spear et al., 1999). Included on the petrogenetic grid are calculated garnet isolines of Fe/(Fe+Mg). The Fe/(Fe+Mg) measured for SMC aluminous gneisses range from 0.74 to 0.90, consistent with the fields shown on the grid (Fig. 31).

Textural analysis also helps to constrain P-T conditions. Muscovite crosscuts foliation and occurs in leucosomes. This muscovite is interpreted to have formed after the peak of metamorphism and after deformation. This suggests that the peak assemblage occurred above the muscovite dehydration melting reaction (e.g. ms + pl + qtz = sil + ksp + liquid; Fig. 31; Spear et al., 1999). The presence of leucosomes in the samples indicates that at least some melt did not leave the system. The occurrence of myrmekites and muscovite and quartz symplectites found in granoblastic samples also suggests melt is retained in the rocks (e.g. Anenburg and Katzir, 2013). The muscovite dehydration reaction, biotite dehydration reaction, and the stability field of sillimanite constrain the P-T range of aluminous gneisses to amphibolite to transitional granulite-grade conditions (Fig. 30, Spear, 1999).

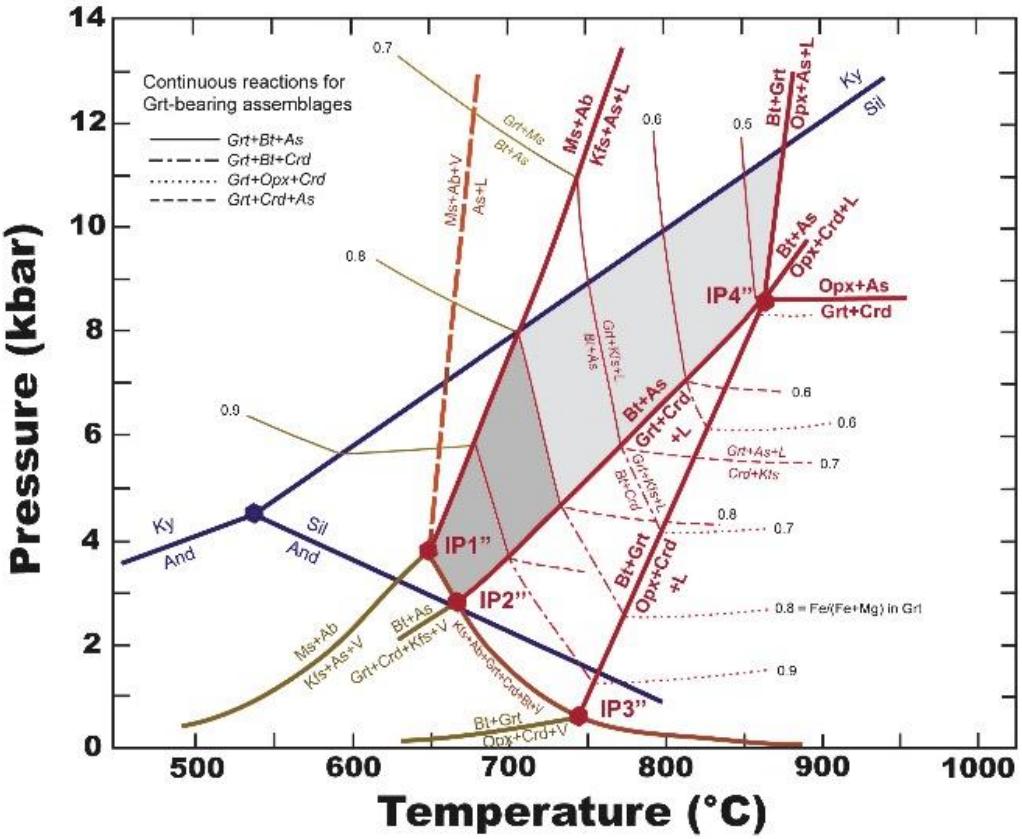

Figure 31: Petrogenetic grid for a pelitic bulk composition Grey field is that of the stable assemblage of SMC aluminous gneisses, bound by the muscovite breakdown reaction, ms + qtz = sil + ksp + liquid, the biotite and sillimanite breakdown reaction, bt + sil = grt + crd + liquid, and the sillimanite to kyanite transition, ky = sil. The darker grey field corresponds to garnet Fe/(Fe+Mg) measured for SMC aluminous gneisses. Petrogenetic grid and garnet isolines from Spear et al, (1999).

A series of continuous biotite dehydration reactions (e.g. bt + sil + pl + qtz = grt + ksp + liquid) exist within the stable assemblage of SMC aluminous gneisses, which enhance the growth of garnet porphyroblasts with increasing metamorphic grade and may contribute modestly to the development of leucosomes (Fig. 31; Spear et al., 1999). The increase in manganese at the garnet rims along with scalloped edges indicates resorption (e.g., Kohn and Spear, 2000). The production of coronas with biotite, plagioclase, and quartz indicate melt these reactions occurred during decompression, forming plagioclase,

quartz, and biotite at the expense of garnet (Fig. 31; e.g. Spear et al., 1999; Storm and Spear, 2005).

Secondary muscovite indicates rehydration of the assemblage at lower temperatures in the muscovite stability field. After peak conditions were reached, the muscovite dehydration melting reaction operated in the reverse (sil + ksp + liquid= ms + pl + qtz), forming muscovite and plagioclase at the expense of alkali feldspar and sillimanite. Some of this muscovite nucleated in the leucosomes generated during prograde metamorphism that trapped liquid. H_2O needed to drive both the muscovite dehydration-melting reaction and the biotite dehydration melting reactions down temperature was likely derived from melt generated during prograde muscovite dehydration, stored in leucosomes.

Two cordierite and hercynite bearing samples, SMC-13-053b and SMC-13-127, collected near the headwall show evidence of a lower pressure metamorphic event overprinting the peak mineral assemblage and are excluded.

The bulk compositions of aluminous gneisses plotted on an AKF ($Al_2O_3 + Fe_2O_3 – K_2O – Na_2O$ – CaO, K_2O, FeO + MgO + MnO) diagram for pelitic bulk compositions at metamorphic conditions consistent with the shaded section in Figure 31 reveals that the bulk chemistry of SMC aluminous gneisses is consistent with the stability of biotite, sillimanite, and garnet (Figs. 31, 32). Two samples however, SMC-14-035 and SMC-14-027, plot outside (or on the border) of this range in the stability field of muscovite, consistent with the abundant muscovite in these samples. Elevated K_2O (5.47 and 6.82 wt. %) may extend the stability of muscovite to higher temperatures.

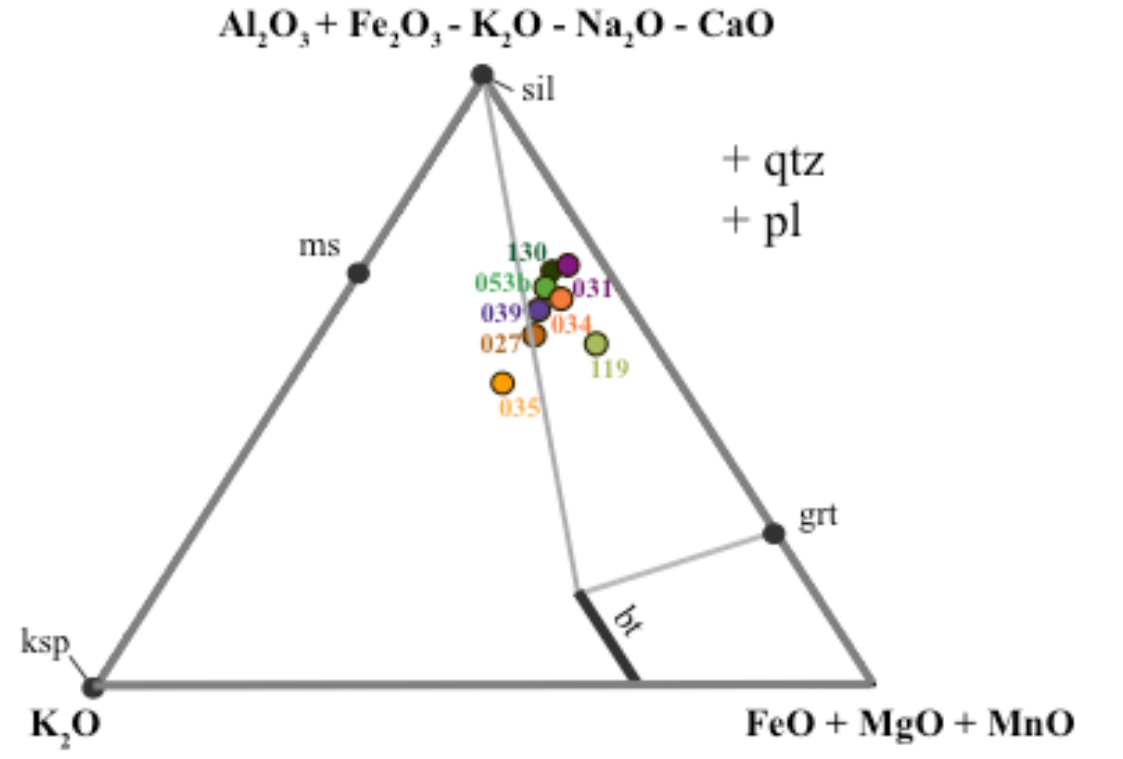

Figure 32: AKF diagram for pelitic bulk compositions for upper amphibolite to lower granulite facies conditions (Spear et al., 1999). Samples fall in the stability field of biotite, garnet, and sillimanite with the exception of SMC-14-035, which falls in the stability field of muscovite.

Metamorphic pathway of SMC aluminous gneisses

Peak conditions for SMC aluminous calculated using classic geothermobarometry vary across the SMC despite all samples having nearly identical peak mineral assemblages. GASP pressures range between 6.5 and 13.5 ± 1.5 kbars and GBPQ pressures range between 5.3 and 10.9 ± 1.2 kbars (Fig. 33). Peak temperatures for each sample are more tightly constrained to between 655 and 777 ± 25 °C (Fig. 24). Additionally, high-pressure conditions may have decreased Ti content in biotite, which decreases apparent temperature (Henry et al., 2005). Most P-T values fall within the range of the stability field of biotite, sillimanite, and garnet on the petrogenetic grid, with

some extending to higher pressure in the kyanite field although no ky is found in these samples (Spear et al., 1999; Fig. 24).

Mineral assemblage diagrams can be used with P-T values calculated using mineral chemistry to refine the P-T conditions and the metamorphic path. Calculated isolines of mineral compositions compared to measured mineral chemistry provide additional constraints on P-T. The percentage of almandine and grossular in garnet cores for each sample is in close agreement with the predictions of garnet composition within the stable assemblage of the models. Such values indicate that garnet retained its peak P-T geochemical signature. However, the percentages of anorthite in plagioclase and the X_{Mg} in biotite (Mg/(Mg + Fe)) measured fall at lower P-T conditions than measured garnet compositions. Consequently, it is suggested that the mineral chemistry of plagioclase and biotite reequilibrated at lower P-T conditions and leads to lower conditions calculated using GASP, GBPQ, GB, and Ti-in-biotite. Reequilibration of plagioclase and biotite may also explain the variation in calculated P-T conditions for samples of similar mineral assemblages.

P-T calculations using plagioclase core data in zoned plagioclase and/or plagioclase inclusions in garnet result in GASP and GB P-T conditions consistent with the locations of garnet compositional isolines in P-T space. This indicates plagioclase cores likely formed under the same P-T conditions as garnet cores. In many samples; however, calculated P-T conditions are lower than the conditions consistent with measured garnet composition. This discrepancy is likely due to either lower P-T conditions of formation of plagioclase and biotite than the conditions of formation for garnet or local reequilibration of plagioclase and biotite at post peak conditions. Where

discrepancy between modeled garnet compositional isolines and calculated P-T values is apparent, P-T conditions likely occur closer in P-T space to the garnet compositional isolines.

Compositional isolines for the anorthite component in plagioclase and the magnesium number in biotite typically plot close together in P-T space, indicating plagioclase and biotite formed under the same P-T conditions. Calculated P-T conditions using garnet and plagioclase rim data coincide with the location of these isolines. The compositional isolines corresponding to garnet rims, however; do not coincide with those for plagioclase and biotite. This discrepancy indicates plagioclase rims and biotite either reequilibrated at post peak conditions or formed at lower P-T conditions than garnet. Mineral assemblage diagrams for SMC samples can be used to constrain post peak reequilibration and define a retrograde path.

Headwall samples

Two Headwall samples were collected within 3000 feet of each other and record similar metamorphic conditions and paths. SMC-13-119, records peak conditions of 9.6 ± 1.5 and 8.1 ± 1.5 kbars and a temperature of 754 °C ± 25 (GB) for inner rim garnet data and plagioclase core data (Fig. 24). These P-T results are within uncertainty of inner rim P-T calculations of SMC-13-118, which records garnet core pressures using garnet core data up to 13.5 ± 1.5 kbars. The compositional isolines for measured almandine (71%) and grossular (7%; Fig. 33; Table 9) components in garnet occur above the peak P-T conditions calculated with GASP and GB of 9.6 ± 1.5 kbars and 754 ± 25 °C (Fig. 24). However, GASP and GB P-T calculations using plagioclase and biotite inclusions in garnet plot near garnet compositional isolines suggesting that these minerals record peak

conditions. After these peak conditions were reached, resetting of matrix plagioclase and biotite occurred, at lower pressures of 5.7 ± 1.5 to 4.6 ± 1.2 kbars and 676 ± 25 °C, within the stability field of muscovite (Fig. 33). These post peak conditions are similar to those in SMC-13-118.

Peak pressure calculations for SMC-13-130 are 7.1 ± 1.5 and 5.9 ± 1.2 kbars and temperatures are 698 ± 25°C, within uncertainty of nearby by SMC-13-128 (Fig. 34). Matrix biotite has a magnesium number of 0.36, which occurs at significantly lower temperature than the corresponding isolines for measured plagioclase and garnet chemistry (Table 11). Plagioclase is ~20-21% anorthite component which is the approximate composition of all plagioclase below ~750 °C (Table 10). The intersection of isolines for the measured almandine (75%) and grossular (4%) components in garnet (Table 9; Fig. 24) occurs at 6.5-7 kbars and 800 °C kbars within the stable assemblage of the mineral assemblage diagram. These data indicate that peak conditions were likely reset. The intersection occurs close to GASP pressures of 7.1 ± 1.5 kbars but at ~100 ° higher temperature than calculated with GB geothermometry. After peak conditions were attained, biotite and plagioclase were reequilibrated at pressures of 6.1 ± 1.2 and 5.3 ± 1.5 kbars and 640 ± 15 °C within the muscovite stability field (Fig. 34).

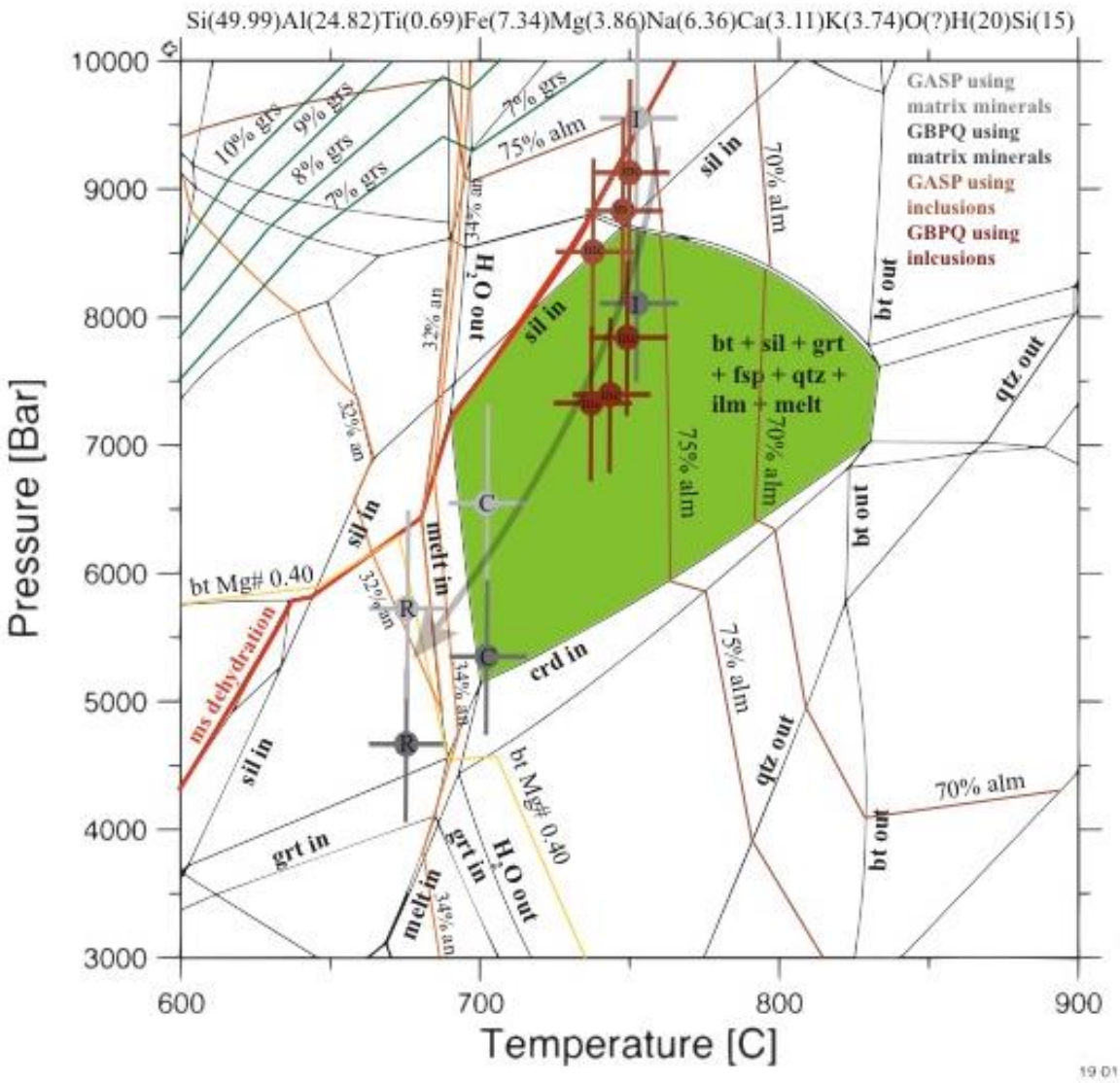

Figure 33: Phase equilibrium model of SMC-13-119 from near the Headwall at Thompson Peak with the P-T range of the stable assemblage in orange. The muscovite dehydration melting reaction is highlighted in red. Isopleths for the percentage of anorthite (% an) in plagioclase, the magnesium number in biotite (bt Mg#), and the percentage of almandine (% alm) and grossular (% grs) in garnet calculated with EMPA are highlighted. GASP (light grey) and GBPQ (dark grey) pressures are plotted with GB temperatures using garnet and plagioclase core (C), inner rim (I), and rim (R) analyses and matrix biotite paired with. P-T calculations using inclusions (inc) are in red with GBPQ pressures in dark red and GASP in light red. The post-peak path is shown with an arrow.

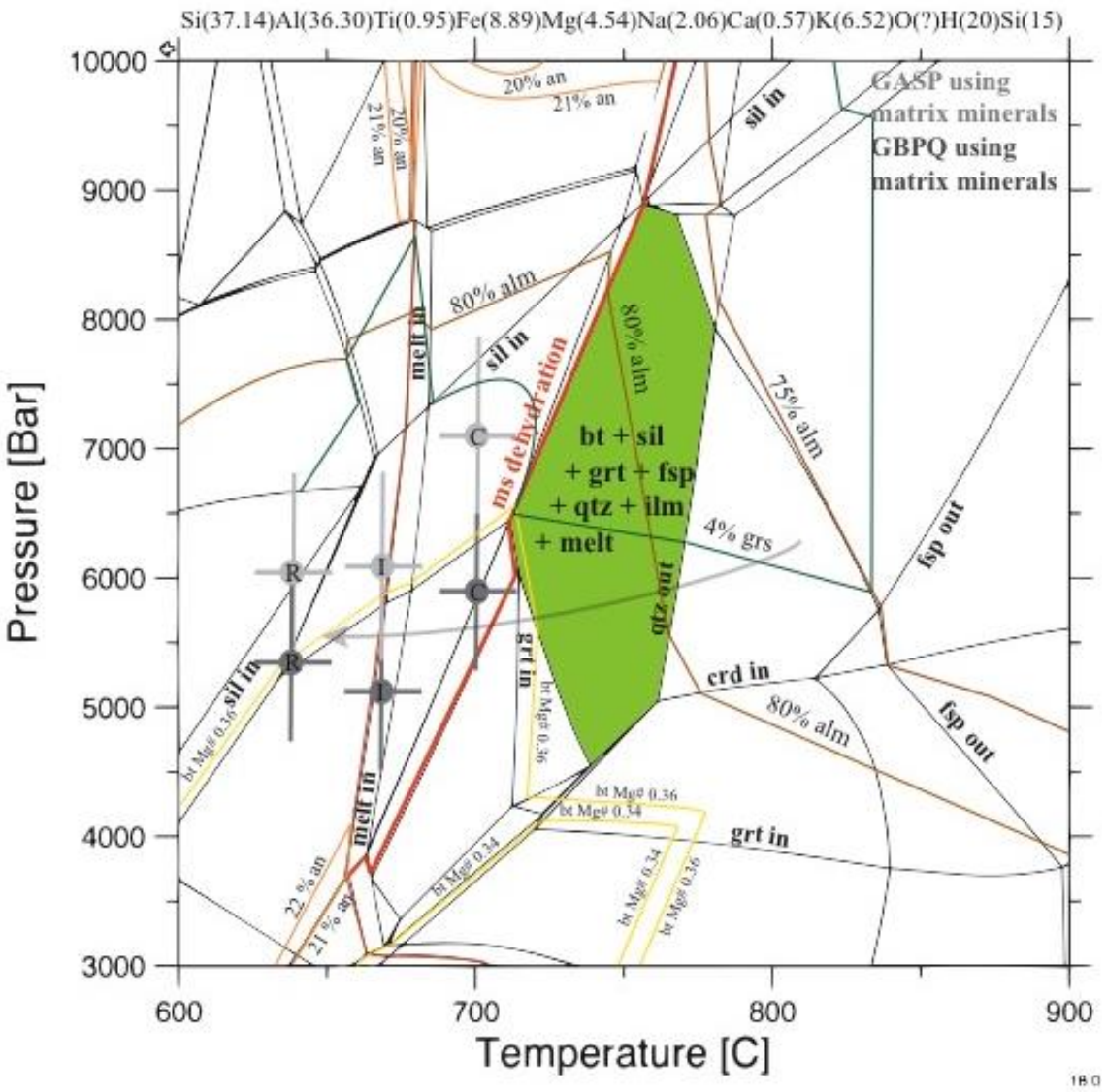

Figure 34: Phase equilibrium model of SMC-13-130 from near the Headwall at Thompson Peak with the P-T range of the stable assemblage outlined in orange. The first appearance of melt and the muscovite dehydration melting reaction are highlighted in red. Isopleths for the percentage of anorthite (% an) in plagioclase, the magnesium number in biotite (bt Mg#), and the percentage of almandine (% alm) and grossular (% grs) in garnet calculated with EMPA are highlighted. GASP (light grey) and GBPQ (dark grey) pressures are plotted with GB temperatures using garnet core (C), inner rim (I), and rim (R) analyses. P-T calculations using inclusions (inc) are in red with GBPQ pressures in dark red and GASP in light red. The post-peak path is shown with an arrow.

Post-peak conditions can be assessed using mineral chemistry from garnet and plagioclase rims. Post-peak conditions calculated for four Headwall samples using garnet and plagioclase rim data and matrix biotite are significantly lower than the peak conditions of 13.5 ± 1.5 kbars and 10.9 ± 1.2 kbars and 777 ± 25 °C.

Calculations using plagioclase and garnet inner rim data and matrix biotite for both SMC-13-119 and SMC-13-118 are within error of each other, recording high pressures between 9 and 11 kbars. The garnet core in SMC-13-119 appears to be reset with a large biotite inclusion, which resulted on low P-T conditions. SMC-13-130 and SMC-13-128 record peak conditions within error of each other between 5.3 and 7.1 kbars and 698 and 716 °C. All headwall samples record similar decompression paths to conditions of ~650 °C and 5-6 kbars (Figs. 33, 34).

Basin samples

For a sample collected from the basin north of Thompson Peak, SMC-14-031, the compositional isolines of grossular (6%) and almandine (70%) coincide near peak GB temperature and the peak GASP pressure (9.1 ± 1.2 kbars) calculated using garnet and plagioclase core data (Fig. 35). Inner rim and rim plagioclase (34-36% anorthite) and the biotite X_{Mg} (0.40) both plot outside of the P-T range of the stable assemblage, indicative of reequilibration the muscovite stability field. These post-peak condtions are recorded in the lower P-T calculations using garnet rims and inner rims (Fig. 35). The retrograde path of SMC-14-031 is similar to that of the Headwall samples.

A second sample collected from the basin, SMC-14-039, records peak pressures of 7.6 ± 1.5 kbars and 6.8 ± 1.2 kbars and GB temperatures of 671 ± 25 °C using inner rim garnet data and averaged (unzoned) plagioclase and biotite data (Fig. 36). This P-T

range exists at lower temperature than the stable assemblage of the sample in the model, within the stability field of muscovite. Garnet inner rim composition is 75% almandine and 4% grossular component corresponding to the calculated compositional isolines of almandine and grossular that intersect at higher P-T conditions of ~9 kbars and ~800 °C. The composition of plagioclase is ~15-16% anorthite which is stable over a wide pressure range below 700 °C. Biotite X_{Mg}=0.34 that is isolated to pressures and temperatures below 6 kbars and 750 °C (Fig. 36). Reequilibration of biotite and plagioclase or formation at post peak conditions results in low calculated P-T conditions. Peak conditions likely occurred where the isolines of grossular and almandine intersect at 9 kbars and 800 °C, similar to SMC-14-031 (Fig. 36).

Goat Lake samples

The P-T path of Goat Lake samples appears to record lower P conditions than others found in the range. SMC-14-034 records peak pressures 5.9 ± 1.2 and 7.5 ± 1.5 kbars and temperatures are 772 ± 25°C using garnet core data and averaged biotite and (unzoned) plagioclase data (Fig. 37). Pressure and temperature decrease slightly towards the rim to 5.6 ± 1.2 and 7.1 ± 1.5 kbars and a temperature 744 ± 25 °C. Measured garnet compositions are ~75% almandine and 4% grossular, on average with a slight increase in almandine from core to rim (Table 9) consistent with the isolines for 75% almandine and 4% grossular that occur in the middle of the field for the stable assemblage calculated in the model (Fig. 37). Plagioclase is ~32-34 % anorthite and biotite has X_{Mg}=0.40. The isolines of these compositions intersect below the P-T range of stable assemblage. The calculated P-T value of SMC-14-034 is in agreement with garnet compositional isolines and likely reflects peak conditions (Fig. 37).

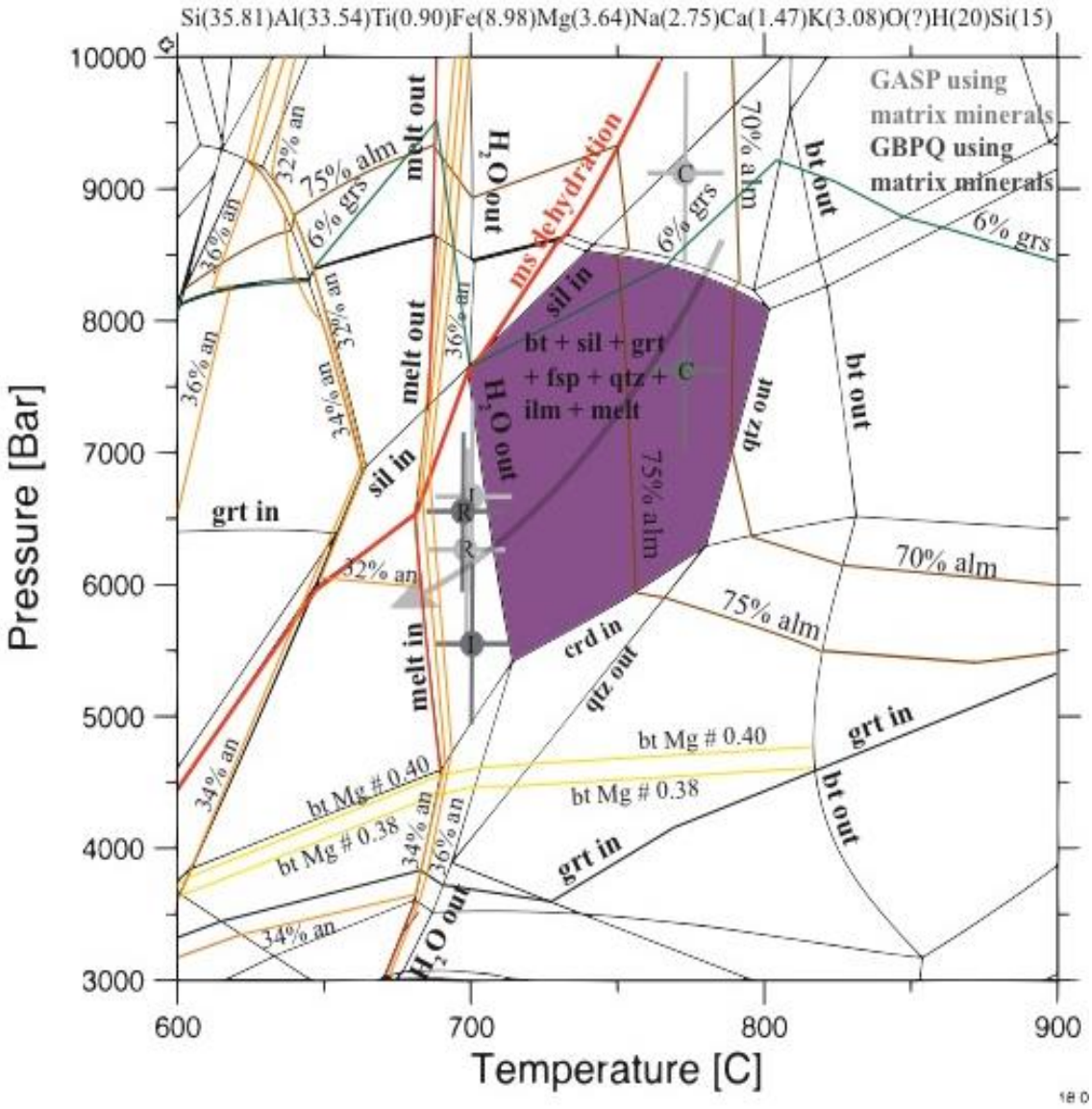

Figure 35: Phase equilibrium model of SMC-14-031 from near Basin with the P-T range of the stable assemblage outlined in orange. The first appearance of melt and the muscovite dehydration melting reaction are highlighted in red. Isopleths for the percentage of anorthite (% an) in plagioclase, the magnesium number in biotite (bt Mg#), and the percentage of almandine (% alm) and grossular (% grs) in garnet calculated with EMPA are highlighted. GASP (light grey) and GBPQ (dark grey) pressures are plotted with GB temperatures using garnet and plagioclase core (C) inner rim (I) and rim (R) analyses paired with matrix biotite. The post-peak path is shown with an arrow.

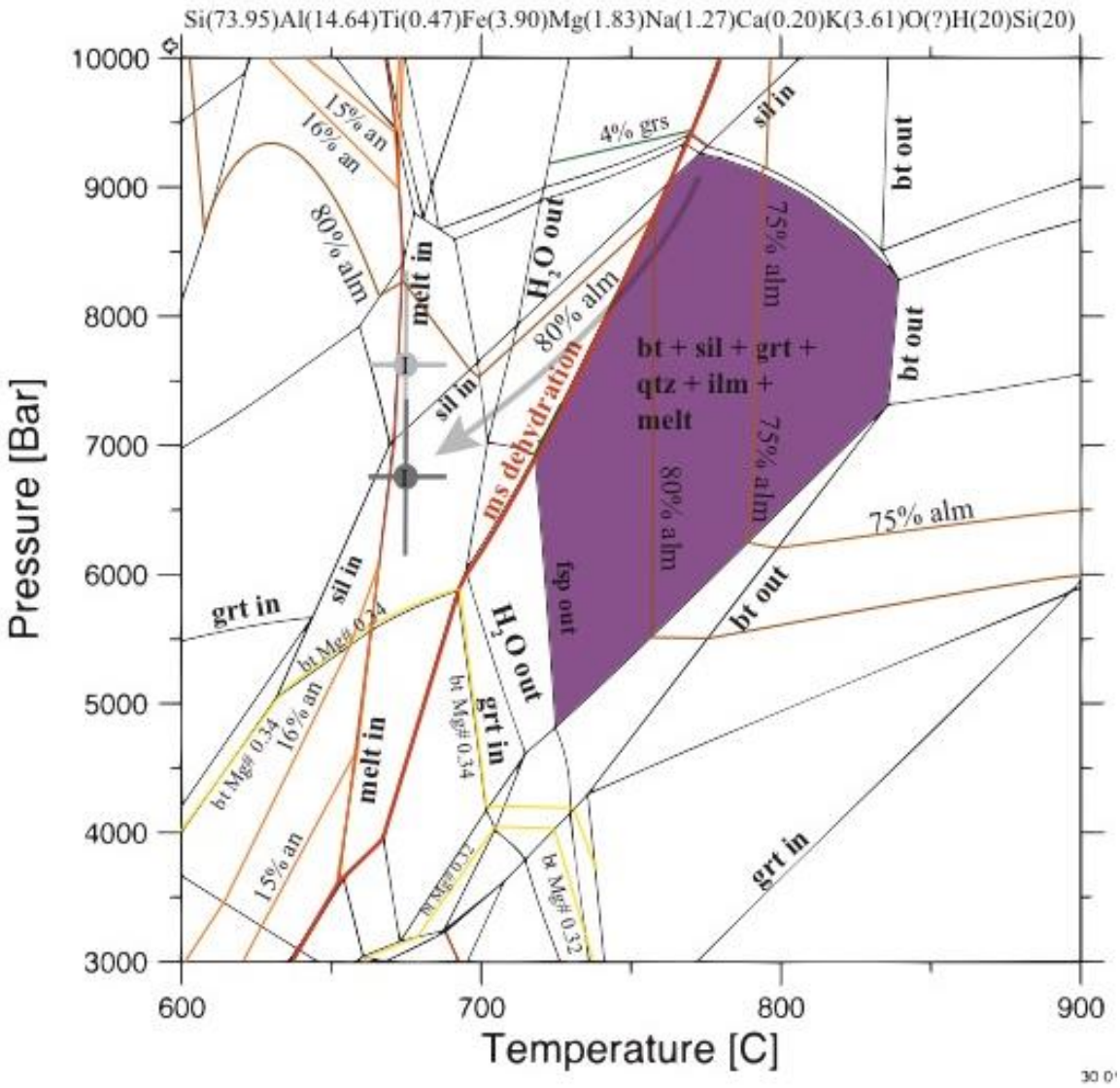

Figure 36: Phase equilibrium model of SMC-14-039 from near the basin in the central SMC with the P-T range of the stable assemblage outlined in orange. The first appearance of melt and the muscovite dehydration melting reaction are highlighted in red. Isopleths for the percentage of anorthite (% an) in plagioclase, the magnesium number in biotite (bt Mg#), and the percentage of almandine (% alm) and grossular (% grs) in garnet calculated with EMPA are highlighted. GASP (light grey) and GBPQ (dark grey) pressures are plotted with GB temperatures using garnet inner rim analyses (I) paired with averaged biotite and plagioclase. The post-peak path is shown with an arrow.

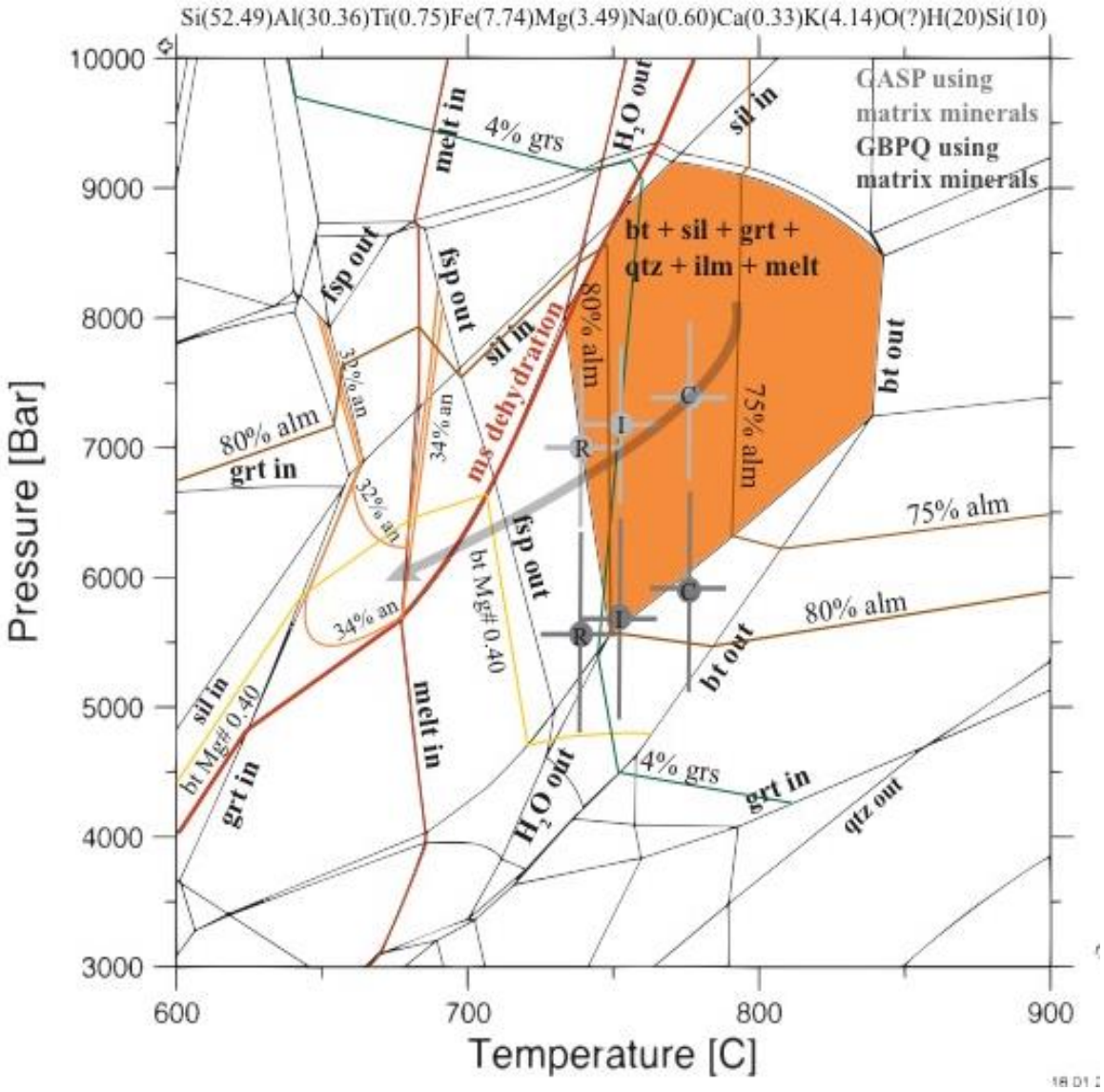

Figure 37: Phase equilibrium model of SMC-14-034 from near Goat Lake with the P-T range of the stable assemblage outlined in orange. The first appearance of melt and the muscovite dehydration melting reaction are highlighted in red. Isopleths for the percentage of anorthite (% an) in plagioclase, the magnesium number in biotite (bt Mg#), and the percentage of almandine (% alm) and grossular (% grs) in garnet calculated with EMPA are highlighted. GASP (light grey) and GBPQ (dark grey) pressures are plotted with GB temperatures using garnet core (C), inner rim (I), and rim (R) analyses. The post-peak path is shown with an arrow.

SMC-14-035, which was collected adjacent to SMC-14-034, records the lowest peak conditions of all samples of 6.4 ± 1.5 and 5.8 ± 1.2 kbars and 668 ± 25 °C in the inner rim (Fig. 38). Peak temperatures were calculated using plagioclase inner rims and plagioclase cores paired with a biotite inclusion in garnet. Peak pressures were calculated garnet inner rims and plagioclase cores with matrix biotite. P-T conditions calculated using garnet core yield conditions are significantly lower than those using inner rim garnet data (Fig. 38). These lower conditions are likely due to late stage fluid infiltration evidenced by several large fractures filled with muscovite and quartz penetrating the garnet. The percentage of almandine in garnet ranges between 75 and 80% and is ~3% grossular, which occurs at higher P-T than the isolines for anorthite in plagioclase (~19%) and the X_{Mg} of biotite (0.39; Tables 9, 10, 11; Fig. 38). Garnet compositional isolines occurs within the stability field of the peak assemblage at 7.5 kbars and 800 °C. Peak conditions for both basin samples likely occurs conditions of ~7.5-8 kbars and ~800 ± 25 °C, evidenced by GASP pressures in SMC-14-034 and the location of the location of garnet compositional isolines (Fig. 38).

Though P-T results for SMC aluminous gneisses calculated with mineral chemistry vary significantly from the Headwall to Goat Lake, phase equilibrium modeling elucidates mineral compositional patterns and partially explains the inconsistent P-T conditions calculated. All SMC samples exhibit the same retrograde path from the peak conditions to reequilibration between 4 and 6 kbars at 600-650 °C in the muscovite stability field. Peak pressure conditions for samples whose compositional isolines do not coincide with calculated GASP pressures are assumed to have experienced significant resetting during the retrograde path. Peak pressure condtions may occur as

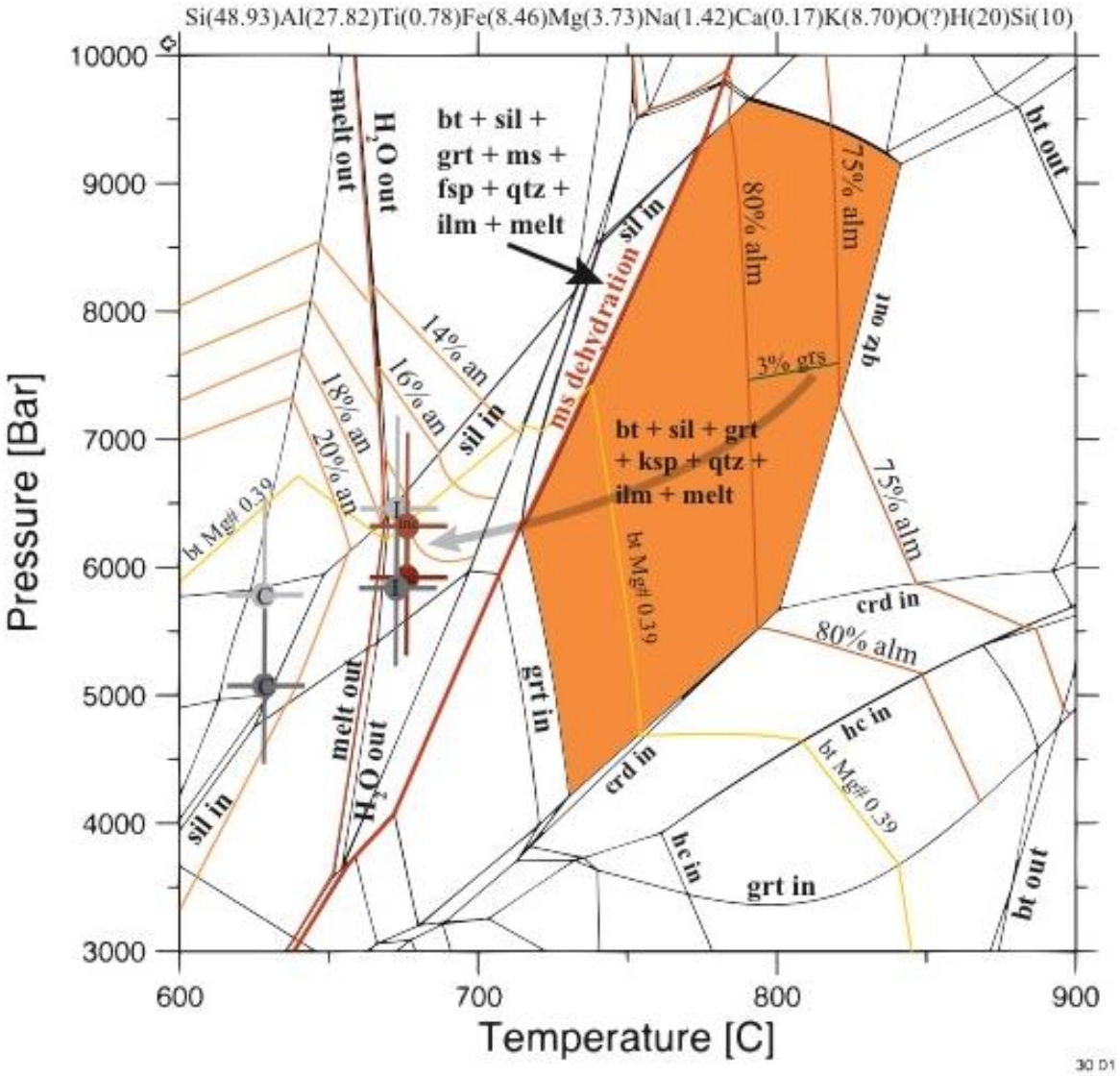

Figure 38: Phase equilibrium model of SMC-14-035 from near Goat Lake with the P-T range of the stable assemblage outlined in orange. The first appearance of melt and the muscovite dehydration melting reaction are highlighted in red. Isopleths for the percentage of anorthite (% an) in plagioclase, the magnesium number in biotite (bt Mg#), and the percentage of almandine (% alm) and grossular (% grs) in garnet calculated with EMPA are highlighted. GASP (light grey) and GBPQ (dark grey) pressures are plotted with GB temperatures using garnet core (C) and inner rim (I). The post-peak path is shown with an arrow. P-T calculations using inclusions (inc) are in red with GBPQ pressures in dark red and GASP in light red.

high as the GASP pressure 13.5 ± 1.5 kbars at the south end of the SMC at the Headwall, recorded for inclusions in a garnet core in SMC-13-118 (Fig. 39). This pressure is outside the stability field of sillimanite, indicating either kyanite was fully transformed during the retrograde path or that the calculation records too high of a pressure. The other two Thompson Peak samples, SMC-13-130 and SMC-13-128 record P-T condition lower than garnet isolines, indicating resetting at post peak condtions from peak conditions of ~9 kbars and 800 °C. Peak pressures for basin samples are also ~9 kbars, supported by a GASP pressure of 9.1 ± 1.5 kbars in SMC-13-031 and garnet compositional data. Peak pressure conditions are 7.5 kbars near Goat Lake, evidenced by a GASP pressure near the intersection of garnet compositional isolines in SMC-14-034 (Fig. 39). SMC-14-035 records lower P-T condtions than other SMC samples and contains abundant alteration minerals. Garnet data, however, are consistent with SMC-14-034, indicating similar peak conditions of ~7.5 kbars followed by resetting at lower conditions of less than 500 °C.

Trends in P-T calculations from core to rim combined with mineral assemblage modeling constitute a partial clockwise metamorphic path consistent with regional metamorphism. Pressure variation from north to south implies variation in burial depth. Burial depth at the Headwall may have been as deep as 39 km assuming a 3 km/kbar pressure gradient. Burial depth decreases to 23 km depth near Goat Lake. Samples, however, span a distance of only ~2 miles. These data indicate that SMC samples record different crustal levels either due to uplift or that they were juxtaposed by faulting. Deformation textures are also consistent with regional metamorphism. Crenulation cleavages and rotated inclusions in garnet indicate two deformation events for each SMC sample.

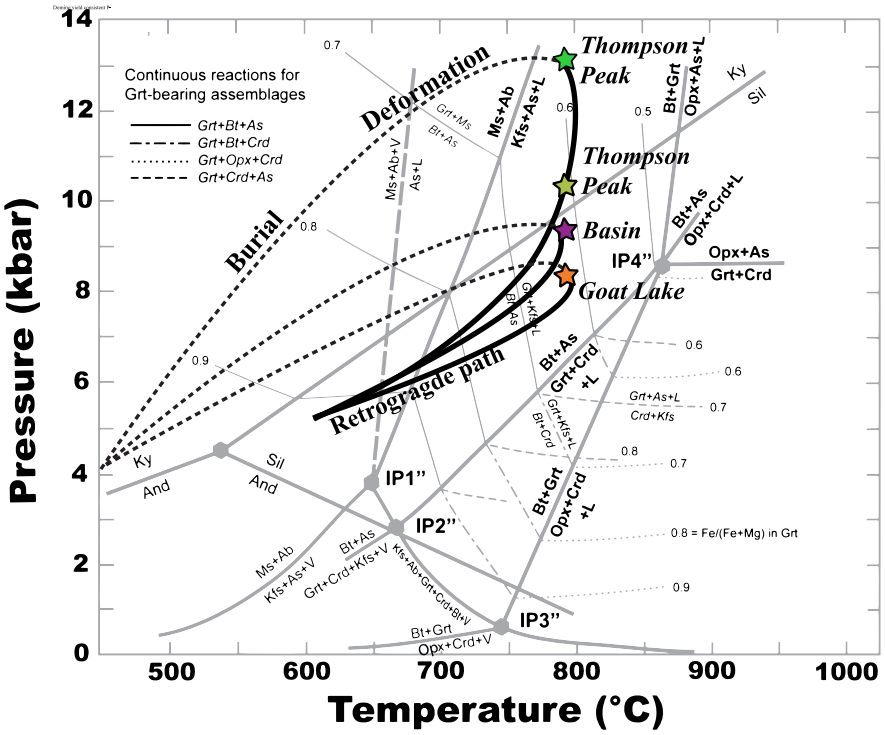

Figure 39: Metamorphic pathway for SMC aluminous gneisses consistent with regional metamorphism caused by burial and uplift record peak pressures from the core of a single headwall sample. Peak pressure decreases gradually north towards Goat Lake. All samples have the same downgrade P-T path (petrogenetic grid from Spear et al., 1999).

P-T conditions for SMC aluminous gneisses are consistent with previous work. Samples from the Headwall near Thompson Peak analyzed by Anderson (1995) and Dutrow et al. (2013) record peak pressures between 6.15 and 11.1 kbars using GASP and between 6.26 and 7.21 kbars using GBPQ. Peak pressures calculated using GBPQ (10.9 ± 1.2 kbars) for SMC-13-118 is within uncertainty of the highest pressure calculated by Anderson (1995) and Dutrow et al. (2013). Temperatures for these samples are between 717 and 747 °C, within uncertainty of temperatures calculated for Thompson Peak samples in this study. A sample from Goat Lake analyzed by Dutrow et al., (2013) records a pressure and temperature within error of those calculated for Goat Lake samples in this study. Temperatures recorded in SMC calc-silicates (750-775 °C) are also

within uncertainty of peak temperatures of aluminous gneisses (Fukai, 2013). The late stage brittle ductile event recorded in calc-silicates is not apparent in aluminous gneisses (Fukai, 2013).

The lithology and P-T conditions of SMC aluminous gneisses are most consistent with those of the Belt-Purcell Supergroup and metasediments in the Great Falls Tectonic Zone. P-T conditions calculated in the Great Falls Tectonic Zone, 600-730°C and 7-11 kbars, are similar to conditions of SMC aluminous gneisses (Cheney et al., 2004; Mueller et al., 2005). Ages of metamorphism, 1.77-2.06 Ga, are consistent with the collision of the Wyoming craton and Medicine Hat block (Mueller et al., 2002; Mueller et al., 2005).

Metamorphic condtions of the Hauser Lake gneiss in the Priest River Complex (7-10 kbars and 675-930 °C) are also similar those of SMC aluminous gneisses. These rocks record metamorphic ages of 1.58 Ga. Metasedimentary rocks in the Priest River complex are interpreted to be those of the Belt-Purcell Supergroup (Doughty et al., 1998).

Some SMC quartzites near Thompson Peak contain 1.70 ± 108 Ma detrital zircons, generally consistent with both the Belt-Purcell Supergroup and the Priest River Complex (Metz, 2010). However, age dating of aluminous gneisses is needed to constrain the relationship between the SMC and the surrounding basement.

Protolith of SMC aluminous gneisses:

The sedimentary protolith of metasediments can be partially constrained by their bulk rock chemistry. The ratio of SiO_2/Al_2O_3 is particularly useful in distinguishing between non-calcareous high SiO_2/Al_2O_3 quartz-rich sandstones and low SiO_2/Al_2O_3 clay-rich shales (Pettijohn, 1972). Wackes and feldspathic and lithic sandstones have intermediate SiO_2/Al_2O_3. This classification scheme can be used as an indicator of

mineralogical maturity (Pettijohn et al., 1972; Herron, 1988). The ratio of Fe_2O_3 to K_2O is useful for distinguishing between lithic fragments and feldspars in sedimentary rocks when all Fe is assumed to be Fe_2O_3 (Herron, 1988). Potassium-rich, iron-poor mineral assemblages are generally more stable in low P-T sedimentary environments whereas high FeO and MgO assemblages are less stable. Therefore, the Fe_2O_3 to K_2O ratio is indicative of mineralogical stability with implications for sedimentary sorting and distance from source (Herron, 1988).

Based on this classification scheme, the protolith of SMC aluminous gneisses are largely categorized as shales, with one iron-rich shale (Fig. 40). NASC also plots in the shale category close to SMC samples but with slightly higher in SiO_2/Al_2O_3 (Table 8). Two silica-rich SMC samples, SMC-14-039 and SMC-14-027, are classified as a litharenite and an arkose, respectively (Fig. 40).

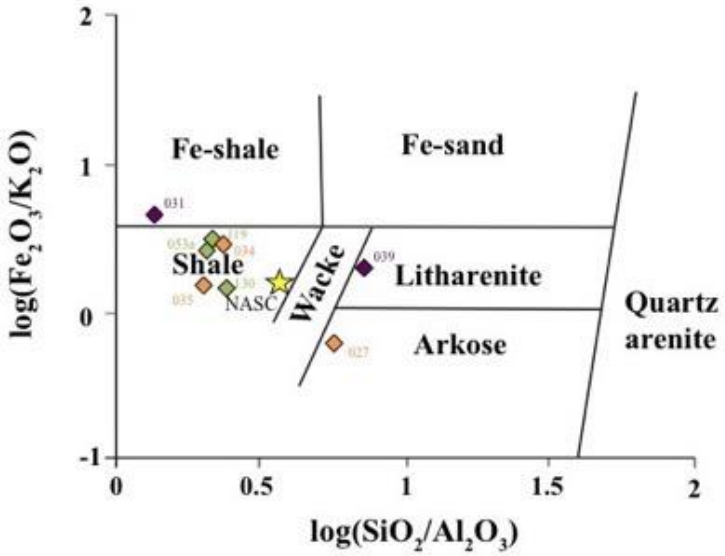

Figure 40: SMC aluminous gneisses plotted in the SandClass system for the geochemical classification of terrigenous sands and shales (Herron, 1988) with NASC (Condie, 1993). Headwall samples are in green, basin samples in purple, and Goat Lake samples in orange.

This sedimentary classification scheme (Fig. 40) requires the assumption that the bulk rock geochemistry represents the original whole rock geochemistry of the samples. Prior to metamorphism, weathering, sorting, and digenesis may have modified the bulk rock geochemistry of SMC samples. The high Al_2O_3 content relative to the other major oxides of SMC samples is consistent with a protolith having undergone weathering or chemical alteration. Weathering trends in silicate rocks leads to the production of clay minerals and loss of alkalis in sedimentary rocks. These changes can be constrained by examining the chemical index of alteration (CIA) of the samples (Nesbitt and Young, 1982). The weathering of feldspar to clay minerals is generally responsible for the depletion in CaO and Na_2O in known as the ideal weathering trend (Nesbitt and Young, 1982; Fig. 41). The origin of the ideal weathering trend has the composition of bulk upper continental crust (UCC; Condie, 1993, Nesbitt and Young, 1982). Depletion in calcium relative to NASC is apparent in all SMC samples, indicating they have experienced some degree chemical alteration. Four samples show weathering along the ideal weathering trend from UCC, indicating a granodiorite or andesite origin. A caveat to this method is that potassium can be enriched by the replacement of kaolinite by illite and the replacement of plagioclase by illite and potassium feldspar, collectively known as the K-metasomatic effect (Fig. 41; Fedo et al., 1995). Potassium metasomatism during weathering and/or metamorphism is apparent for three SMC samples as well as for NASC. However, this deviation from the ideal weathering trend may stem from a more potassium rich, granitic or rhyolitic, sediment source. The impact weathering and alteration must be considered when attempting to reconstruct provenance of metasediments.

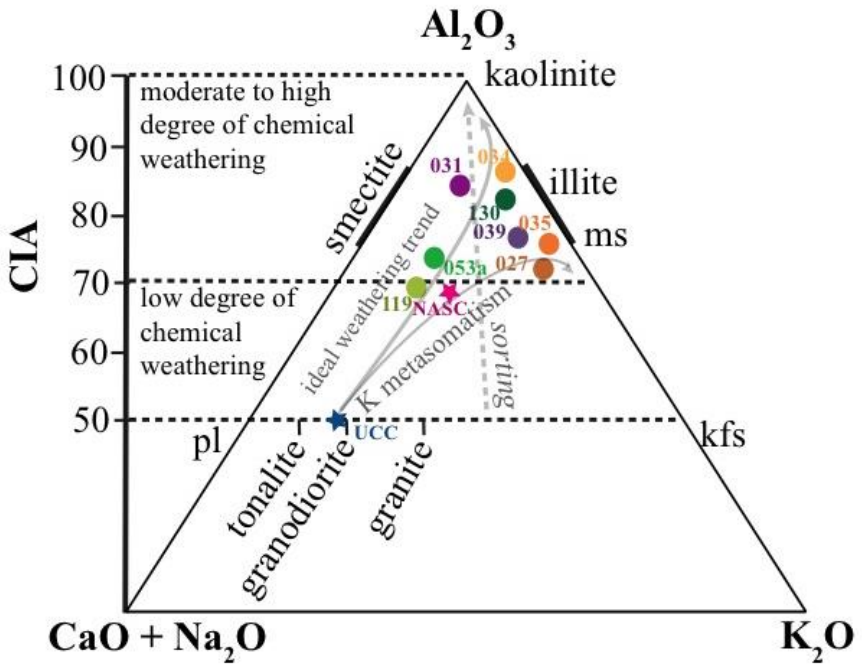

Figure 41: SMC aluminous gneisses plotted with NASC and UCC (Condie, 1993) on an Al_2O_3, $CaO + Na_2O$, K_2O diagram and the corresponding chemical index of alteration (CIA; Nesbitt and Young, 1982). Marked on the diagram is the ideal weathering trend for sedimentary rocks with UCC at the origin and the deviation from this ideal trend due to potassium metasomatism (Nesbitt and Young 1984; Fedo et al., 1995).

The degree of chemical alteration of sediment has implications for paleoclimate (Nesbitt and Young, 1982; Goldberg and Humayun, 2010). Chemical alteration leading to the formation of clay minerals from feldspars is enhanced in humid conditions. Clay-rich muds in tropical regions have CIA values of 80-100. In glacial environments where chemical alteration is low, the CIA ranges from 50-70 (Nesbitt and Young, 1982). The CIA for SMC samples range between ~70 and 90 (Fig. 41), indicating enhanced chemical alteration in humid, tropical to subtropical conditions. CIA molar can distinguish between sediments in tropical and arid climate when plotted against Na_2O/K_2O and Al_2O_3. SMC aluminous gneisses fall in the tropical range using this technique (Fig. 42; Goldberg and Humayun, 2010).

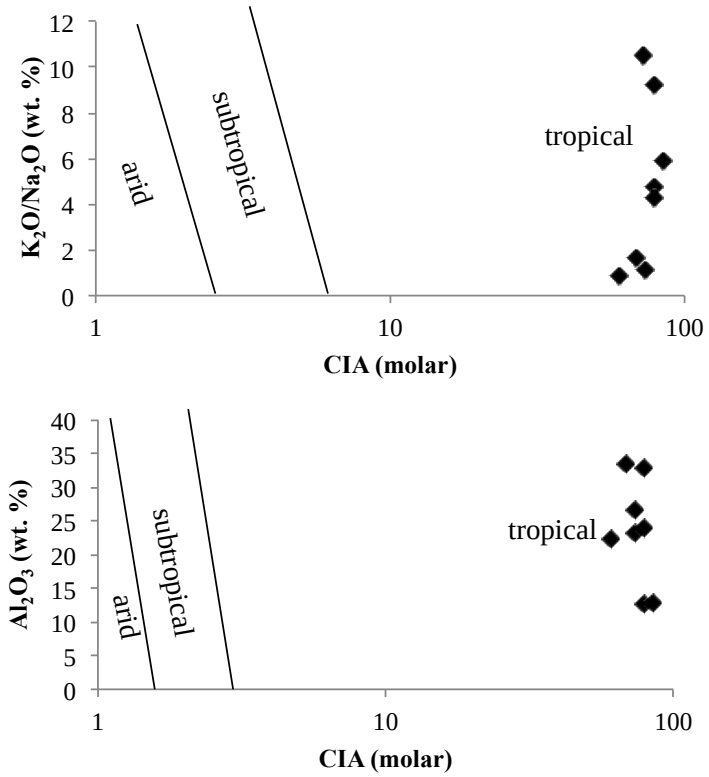

Figure 42: K_2O/Na_2O (top) and Al_2O_3 (bottom) vs. the chemical index of alteration (CIA) for SMC aluminous gneisses to distinguish alteration in arid vs. tropical regions (Nesbitt and Young, 1982; Goldberg and Humayun, 2010).

Tectonic setting of SMC aluminous gneisses:

Whole rock geochemical data of metasediments can be used to infer between tectonic settings. SMC aluminous gneisses share characteristics with sediments deposited in a passive margin environment based of their high ratio of K_2O/Na_2O vs. SiO_2 (Fig. 43; Roser and Korsch, 1986). However, chemical alteration is not accounted for in this classification scheme. A passive margin depositional environment is consistent with the formation of finely laminated shales. Layers of granoblastic quartzofeldspathic minerals and pelitic minerals in SMC aluminous gneisses are interpreted as an artifact of sedimentary layering or generated due to melting. Calc-silicate units east of aluminous gneisses provide evidence for the presence of an ancient shoreline or at least shallower

water (Fukai, 2011). If the units of the SMC are continuous, the protolith of SMC aluminous gneisses likely occurred adjacent to the calcareous sedimentary protolith of SMC calc-silicates but at deeper water depth.

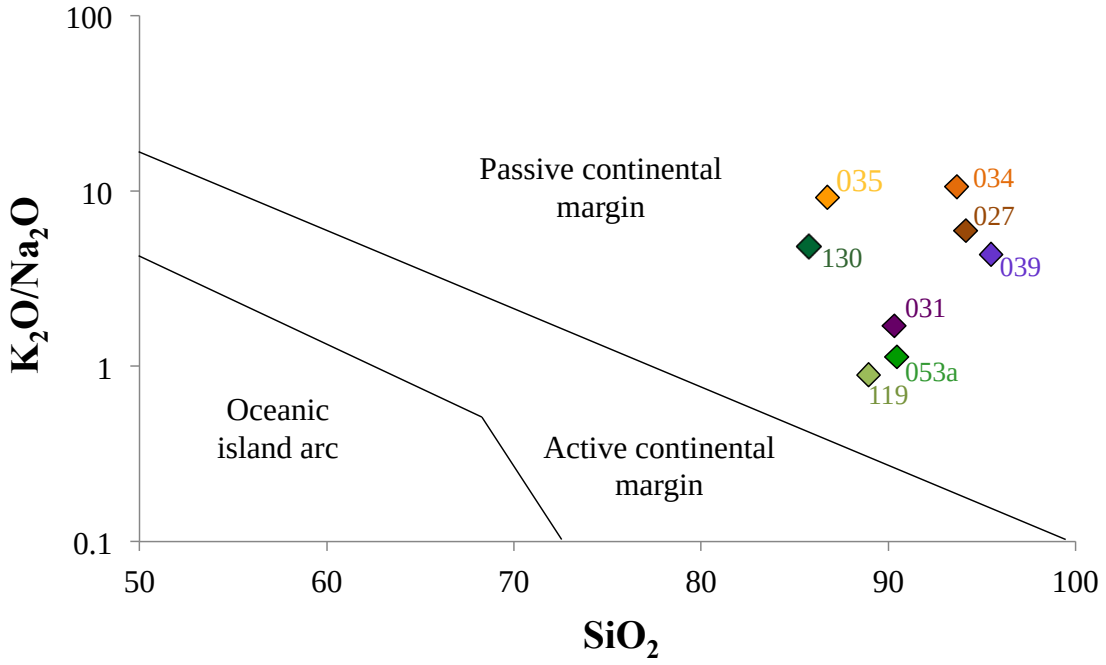

Figure 43: Bulk rock composition of SMC aluminous gneisses on the wt. % K_2O/Na_2O-SiO_2 diagram for tectonic discrimination of sandstone-mudstone suites. Markers are colored as to location: Headwall samples: green, basin: purple, and Iron Creek: orange, (Roser and Korsch, 1986).

SMC aluminous gneisses are likely derived from well-sorted shale deposited in a calm, passive margin environment in humid conditions. The calcium depletion and aluminum enrichment in aluminous gneisses is likely due to enhanced chemical weathering and the production of clay minerals. Variation in whole rock geochemistry and mineral modes across the SMC may be related to provenance, with more potassium rich, granitic/rhyolitic material sourcing the north and more granodioritic/andesitic material sourcing the south. However, these variations could also be related to varying degrees of chemical alteration, metasomatism and/or sorting of the original sediments.

CONCLUSIONS

Petrographic analysis, geothermobarometry results, and phase equilibrium modeling indicate that SMC aluminous gneisses record a high-grade regional metamorphic path. The peak metamorphic mineral assemblage, bt + grt + sil + ilm + zrn + mnz ± pl ± qtz ± kfs ± ap ± xn ± py ± po ± ccp ± gr, constrains P-T to above the muscovite dehydration reaction, below the biotite dehydration-melting reaction, and within the sillimanite zone. Two deformational events are preserved. D1 is recorded as foliation and rotated sillimanite inclusions in garnet suggesting it occurred within the sillimanite zone. D2 is recorded as crenulation cleavages preserved by biotite and sillimanite. Rocks reach sufficiently high temperatures to produce melt, evidenced by leucosomes and myrmekites. This melt was likely due to muscovite dehydration-melting reaction.

Geothermobarometry in conjunction with phase equilibrium modeling elucidates a regional metamorphic pathway for the SMC samples. These modeling studies reveal new information on the SMC metamorphic path and are the first MAD diagrams to be constructed for these rocks. Peak pressure is likely recorded by the GBPQ calculated pressure of 10.9 ± 1.3 kbars. Peak pressures decrease towards the north from 9.6 to 7.5 kbars across the SMC. . Calculated peak temperature is constrained between 665 and 777 ± 25 °C, in close agreement with the location of garnet compositional isolines in P-T space coinciding with mineral chemical data. . Retrogression to ~4-6 kbars and ~600-650 °C followed peak conditions for each sample as suggested by lower T-P conditions recorded at the rim and partial biotite dehydration-melting reactions during retrograde metamorphism, creating coronas of course grained plagioclase, biotite, and quartz and

Mn-richer garnet rims. Local reequilibration of biotite and plagioclase post peak temperatures is suggested by the difference in isolines versus measured compositions. Rehydration in the muscovite stability field led to the post deformational formation of muscovite, overprinting biotite and sillimanite.

The clockwise P-T pathway of SMC-aluminous gneisses is consistent with a compressional tectonic environment, involving burial to middle-lower crustal conditions, two deformational events, and retrogression. The peak pressure decrease across the SMC corresponds to changes in crustal level, suggesting that the SMC records different exhumed levels or is composed of tectonic slices.

Whole rock geochemical analyses suggest SMC aluminous gneisses constitute a section of heavily weathered, mature shale with finely fluctuating amounts of clay and quartzofeldspathic material derived from the weathering of granodioritic to granitic material deposited in a humid passive margin environment. SMC aluminous gneisses may have occurred contemporaneously with adjacent calc-silicates. This depositional setting is inconsistent with that of the Selway Terrane, which is proposed to be composed of Archean juvenile magmatic belts (Foster et al., 2006).

REFERENCES

Anderson, S.D., 1995, Petrology of Precambrian roof pendants: Thompson Peak, Sawtooth Mountains, Idaho. Unpublished Senior Thesis, Baton Rouge, LA, Louisiana State University.

Anenburg, M. and Katzir, Y., 2013, Muscovite dehydration melting in Si-Rich metapelites: microstructural evidence from trondhjemitic migmatites, Roded, Southern Israel: Mineralogy and Petrology, v. 108, p. 137-152.

Bader, T., Franz, L., de Capitani, C. and Zhang, L., 2014, The effect of water activity on calculated phase equilibria and garnet isopleth thermobarometry of granulites with particular reference to Tongbai (east central China): European Journal of Mineralogy, v. 26, p. 5-23.

Bartoli, O., Tajčmanová, L., Cesare, B. and Acosta-Vigil, O., 2013, Phase equilibria constraints on melting of stomatic migmatites from Ronda (S. Spain): insights on the formation of peritectic garnet: Journal of Metamorphic Geology, v. 31, p. 775-789.

Bergeron, P.G., 2012, U-Pb geochronology of detrital zircons in quartzites of the Sawtooth Metamorphic Complex, Sawtooth Range, Idaho, U.S.A. Unpublished Masters Thesis, LSU, Baton Rouge, LA.

Berman, R.G., 1991, Thermobarometry using multi-equilibrium calculations-A new technique, with petrological applications: Canadian Mineralogist, v. 29, p. 833-855.

Boerner, D.E., Craven, J.A., Kurtz, R.D., Ross, G.M. and Jones, F.W., 1997, The Great Falls Tectonic Zone: suture or intracontinental shear zone: Canadian Journal of Earth Sciences, v. 35, p. 175-183.

Brown, M., 2002, Retrograde processes in migmatites and granulites revisited: Journal of Metamorphic Geology, v. 20, p. 25–40.

Büttner, S.H., 2012, Rock Maker: an MS ExcelTM spreadsheet for the calculations of rocks compositions from proportional whole rock analyses, mineral compositions, and modal abundance: Mineralogy and Petrology, v. 104, p. 129-134.

Chamberlain, K.R., Frost, C.D. and Frost, B. R., 2003, Early Archean to Mesoproterozoic evolution of the Wyoming Province: Archean origins to modern lithospheric architecture: Canadian Journal of Earth Sciences, v. 40, p. 1357-1374.

Collet, S. and Faryad, S.W., 2015, Pressure-temperature evolution of Neoproterozoic metamorphism in the Welayati Formation (Kabul Block), Afghanistan: Journal of Asian Earth Sciences, v. 111, p. 698-710.

Cross, W., Iddings, J.P., Pirsson, L.V. and Washington, H.S., 1903, Quantitative Classification of Igneous Rocks: University of Chicago Press.

Doughty, P.T. and Chamberlain, K. R., 2008, Protolith age and timing of Precambrian magmatic and metamorphic events in the Priest River complex, northern Rockies: Canadian Journal of Earth Sciences, v. 45, p. 99-116.

Doughty, P. T., Price, R.A. and Parrish, R.R., 1997, Geology and U-Pb geochronology of Archean basement and Proterozoic cover in the Priest River complex, northwestern United States, and their implications for Cordilleran structure and Precambrian continent reconstructions: Canadian Journal of Earth Sciences, v. 35, p. 39-54.

Doughty, P.T. and Price, R.A., 1999, Tectonic evolution of the Priest River complex, northern Idaho and Washington: A reappraisal of the Newport fault with new insights on metamorphic core complex formation: Tectonics, v. 18, no. 3, p. 375-393.

de Capitani, C., and Petrakakis, K., 2010, The computation of equilibrium assemblage diagrams with Theriak/Domino software: American Mineralogist, v. 95, p. 1006-1016.

Dutrow, B.L., Anderson, S., Henry, D J., Mueller, P. and Giaramita, M., 1995, A new Precambrian crustal province in south-central Idaho? EOS. Transactions of the Am. Geophysical Union 76: F678.

Dutrow, B. L., Foster C.T. and Whittington, J., 2008, Prograde muscovite-rich pseudomorphs as indicators of conditions during metamorphism: An example from NW Maine. American Mineralogist, v. 93, p. 300-314.

Dutrow, B. L., Henry, D.J., Fukai, I. and Metz, K., 2013, Garnet as a reactant during and recorder of mid-crustal metamorphism: Sawtooth Metamorphic Complex, Idaho: AGU Abstracts with Programs, v. 51, p. 2666.

Evans, K.V., Aleinikoff, J.N., Obradovich, J.D. and Fanning, C., 2000, SHRIMP U-Pb geochronology of volcanic rocks, Belt Supergroup, western Montana: evidence for rapid deposition of sedimentary strata Canadian Journal of Earth Sciences, v. 37, p. 1287-1300.

Fedo, C.M., Nesbitt, H.W., and Young, G.M., 1995, Unraveling the effects of potassium metasomatism in sedimentary rocks and paleosols, with implications for paleoweathering conditions and provenance: Geology, v. 23, p. 921–924.

Foster, D.A., Mueller, P.A., Mogk, D.W., Wooden, J.L. and Vogl, J.J., 2006, Proterozoic evolution of the western margin of the Wyoming craton: implications for the tectonic and magmatic evolution of the northern Rocky Mountains: Canadian Journal of Earth Sciences, v. 43, p. 1601-1619.

Frost, C.D., Fruchey, B.L, Chamberlain, K.R. and Frost, B.R, 2006, Archean crustal growth by lateral accretion of juvenile supracrustal belts in the south-central Wyoming Province Canadian Journal of Earth Sciences, v. 43, p. 1533-1555.

Fukai, I., 2013, Metamorphic and Geochemical Signatures of Calc-Silicate Gneisses from the Sawtooth Metamorphic Complex, Idaho, USA: Implications for Crustal Evolution in Western North America. Unpublished Masters Thesis, LSU, Baton Rouge, LA.

Gifford, J.N., Mueller, P.A., Foster, D.A. and Mogk, D.W., 2014, Precambrian Crustal Evolution in the Great Falls Tectonic Zone: Insights from Xenoliths from the Montana Alkali Province The Journal of Geology, v. 122, p. 531-548.

Goldberg, K., Humayun, M., 2010, The Applicability of the Chemical Index of Alteration as a Paleoclimate Indicator: An Example from the Permian of the Paraná Basin, Brazil: Palaeogeography, Palaeoclimatology, Palaeoecology, v. 293, p. 175-183.

Gorman, Andrew R., Clowes, R.M., Ellis, R.M., Henstock, T.J., Spence, G.D., Keller, G.R., Levander, A., Snelson, C.M., Burianyk, M.J.A., Kanasewich, E.R., Asudeh, I., Jajnal, Z. and Miller, K.C., 2002, Deep Probe, imaging the roots of western North America: Canadian Journal of Earth Sciences, v. 39, p. 375-398.

Hallet, B.W. and Spear, F.S., 2014, The P-T History of Anatectic Pelites of the East Humboldt Range, Nevada: Evidence for tectonic Loading, Decompression, and Anatexis: Journal of Petrology, v. 55, p. 3-36.

Herron, M. M., 1988, Geochemical classification of terrigenous sands and shales from core or log data: Journal of Sedimentary Petrology, v. 58, p. 820-829.

Henry, D.J., Guidotti, C.V. and Thomas, J.A., 2005, The Ti-saturation surface for low-to-medium pressure metapelitic biotites: Implications for geothermometry and Ti-substitution mechanisms: American Mineralogist, v. 90, p. 316-328.

Hodges, K. V. and Crowley, P. D.,1985, Error estimation in empirical geothermometry and geobarometry for pelitic systems: American Mineralogist, v. 70, p. 702–709.

Hoffman, P.F., 1988, United Plates of America, the Birth of a Craton - Early Proterozoic Assembly and Growth of Laurentia: Annual Review of Earth and Planetary Sciences, v. 16, p. 543-603.

Holdaway, M.J., Mukhopadhyay, B., Dyar, M.D., Guidotti, C.V. and Dutrow, B.L., 1997, Garnet-biotite geothermometry revised: New Margules parameters and a natural specimen data set from Maine: American Mineralogist, v. 82, p. 582-595.

Holdaway, M. J., 2000, Application of new experimental and garnet Margules data to the garnet-biotite geothermometer: American Mineralogist, v. 85, p. 881-892.

Holdaway, M.J., 2001, Recalibration of the GASP geobarometer in light of recent garnet and plagioclase activity models and versions of the garnet-biotite geothermometer: American Mineralogist, v. 86, p. 1117-1129.

Holland, T.J.B., and Powell, R., 1998, An internally consistent thermodynamic dataset for phases of petrological interest: Journal of Metamorphic Geology, v. 16, p. 309-344.

Holland, T. J. B. and Powell, R., 2011, An improved and extended internally consistent thermodynamic dataset for phases of petrological interest, involving a new equation of state for solids: Journal of Metamorphic Geology, v. 29, p. 333-383.

Hollocher, K., 2011, Calculation of a CIPW norm from bulk chemical analysis. ExcelTM spreadsheet program, Union College, Schenectady, NY.

Johnson, D.M., Hooper, P.R., and Conrey, R.M., 1999, XRF analysis of rocks and minerals for major and trace elements on a single low dilution Li-tetraborate fused bead: Advances in X-Ray analysis, v. 41, p. 843-867.

Kellogg, K.S. and Mogk, D.W., 2009, Structural development of high-temperature mylonites in the Archean Wyoming province, northwestern Madison Range, Montana: Rocky Mountain Geology, v. 44, p. 85-102.

Kohn, M.J., Catlos, E.J., Ryerson, F.J. and Harrison, T.M., 2016, Pressure-temperature-time path discontinuity in the Main Central thrust zone, central Nepal: Geology v. 29, no. 7, p. 571-574.

Kohn, M.J. and Spear, F., 2016, Retrograde net transfer reaction insurance for pressure-temperature estimates: Geology, v. 28, p. 1127-1130.

Lemieux, Sophie, Ross, Gerald M. and Cook, Frederick A., 2000, Crustal geometry and tectonic evolution of the Archean basement beneath the southern Alberta Plains, from new seismic reflection and potential field studies: Canadian Journal of Earth Sciences, v. 37, p. 1473-1491.

Lund, K ,2003, Metamorphic rocks of central Idaho: A progress report. Blet Symposium III: Idaho Bureau of Mines and Geology, v. 3, p. 116-132.

Maley, T., 1987, Exploring Idaho Geology. Mineral Land Publications, Boise, ID, p. 232

Ma, Chong, Bergeron, P., Foster, D., Dutrow, B., Mueller, P. and Allen, C., 2015, Detrital Zircon Geochronology of the Sawtooth Metamorphic Complex, Idaho: Evidence for Lower Paleozoic Shelf Strata within the Idaho Batholith: Geosphere. Unpublished Manuscript.

McCombs, J.A., Dahl, P.S. and Hamilton, M.A., 2003, U-Pb ages of Neoarchean granitoids from the Black Hills, South Dakota, USA: implications for crustal evolution in the Archean Wyoming province: Precambrian Research, v. 130, p. 161-184.

Metz, K., 2010, Metamorphic Rocks in the Sawtooth Mountains, Idaho, USA: A Window into the Precambrian Basement of Southwest Laurentia. Unpublished Masters Thesis, LSU, Baton Rouge, LA.

Mogk, D.W., Mueller, P.A., and Wooden, J.L., 1992, The Nature of Archean Terrane Boundaries - an Example from the Northern Wyoming Province. Precambrian Research, v. 55, p. 155-168.

Moulas, E., Tajčmanová, L., Vrijmoed, J.C. and Podladchikov, Y., 2015, Mechanically-v. diffusion-controlled metamorphic microstructure: a symplectite example from Rhodope Metamorphic Complex (Greece): Journal of Metamorphic Geology, v. 33, p. 849-858.

Mueller, P.A., Burger, H.R., Wooden, J.L., Brady, J.B., Cheney, J.T., Harms, T.A., Heatherington, A.L. and Mogk, D.W., 2005, Paleoproterozoic Metamorphism in the Northern Wyoming Province: Implications for the Assembly of Laurentia The Journal of Geology, v. 113, p. 169-179.

Mueller, P. A., Foster, D.A., Mogk, D.W., and Wooden, J.L., 2004, New insights into the Proterozoic evolution of the western margin of Laurentia and their tectonic implications. Geological Society of America, Abstracts with Programs, v. 36 p. 404.

Mueller, P.A. and Frost, C.D., 2006, The Wyoming Province: a distinctive Archean craton in Laurentian North America: Canadian Journal of Earth Sciences, v. 43, p. 1391-1397.

Mueller, P.A., Heatherington, A.L., Kelly, D.M., Wooden, J.L., Mogk, D.W., 2002, Paleoproterozoic crust within the Great Falls tectonic zone: Implications for the assembly of southern Laurentia Geology, v. 30, no. 2, p. 127-130.

Mueller, P. A., Burger, H.R., Wooden, J.L., Brady, J.B., Cheney, J.T., Harms, T.A., Heatherington, A.L., and Mogk, D.W., 2005, Paleoproterozoic metamorphism in the Northern Wyoming province Implications for the assembly of Laurentia. Journal of Geology, v. 113, 169-179.

Mueller, P., Mogk, D., Henry, D., Foster, D., Tyler, B. Grip, T., Hanson, M., Kotash, A., Maloney, P., Philbrick, K. and Ware, B., 2014, Mesoarchean plutonism in the south snowy block (Yellowstone National Park): New evidence for an old arc: Northwest Geology, v. 43, p. 91-98.

Mueller, P.A., Mogk, D.W., Henry, D.J., Wooden, J.L., Mogk, D.W. and Foster, D.A., 2014, The Plume to Plate Transition: Hadean and Archean Crustal Evolution in the Northern Wyoming Province, U.S.A., in Yildirim Dilek, H. F., ed., Evolution of Archean Crust and Early Life Netherlands: Springer Netherlands p. 23-54.

Mueller, P.A., Wooden, J.L., Mogk, D.W. and Foster, D.A., 2011, Paleoproterozoic evolution of the Farmington zone: Implications for terrane accretion in southwestern Laurentia: Lithosphere, v. 3, p. 401-408.

Mueller, P.A., Wooden, J.L., Mogk, D.W., Henry, D.J. and Bowes, D.R., 2010, Rapid growth of an Archean coninent by arc magmatism Precambrian Research v. 183, p. 70-88.

Mueller, P.A., Wooden, J.L. and Nutman, A.P., 1992, 3.96 Ga zircons from an Archean quartzite, Beartooth Mountains, Montana: Geology, v. 20, p. 327-330.

Nesbitt, H.W., and Young, G.M., 1982, Early Proterozoic climates and plate motions inferred from major element chemistry of lutites: Nature, v. 299, p. 715–717.

Nesbitt, H.W., and Young, G.M., 1989, Formation and diagenesis of weathering profiles: Journal of Geology, v. 97, p. 129–147.

Pettijohn, F.J., Potter, P.E., and Siever, R., 1972, Sand and Sandstone: New York, Springer-Verlag, p. 618.

Petrík, I., Janák, M., 2002, Migmatites and leucogranites produced by muscovite dehydration melting on the example of the Strážovské Vrchy Mts. (Suchy Core), Western Carpathians: Geolines, v. 14, p. 74– 75.

Pownall, J. M., 2015, UHT metamorphism on Seram, eastern Indonesia: reaction microstructures and P-T evolution of spinel bearing garnet-sillimanite granulites from the Kobipoto Complex: Journal of Metamorphic Geology, v. 33, p. 909-935.

Powell, R. and Holland, T.J.B., 1988, An internally consistent thermodynamic dataset with uncertainties and correlations: 3: application methods, worked examples and a computer program: Journal of Metamorphic Geology, v. 6, p. 173-204.

Powell, R. and Holland, T., 2010, Using Equilibrium Thermodynamics to Understand Metamorphism and Metamorphic Rocks: Elements, v. 6, p. 309-314.

Reid, R.R., 1963, Reconnaissance geology of the Sawtooth range: Idaho Bureau of Mines, v. 129.

Roser, B. P. & Korsch, R. J., 1986, Determination of tectonic setting of sandstone-mudstone suites using SiO_2 content and K_2O/Na_2O ratio: Journal of Geology, v. 94, p. 635-650.

Ross, G.M., Eaton and D.W., 2001, Proterozoic tectonic accretion and growth of western Laurentia: results from Lithoprobe studies in northern Alberta: Canadian Journal of Earth Sciences, v. 39, p. 313-339.

Ross, G.M., Patchett, P.J., Hamilton, M., Heaman, L., DeCelles, P.G., Rosenburg, E. and Giovanni, M.K., 2005, Evolution of the Cordilleran orogen (southwestern Alberta, Canada) inferred from detrital mineral geochronology, geochemistry, and Nd isotopes in the foreland basin: GSA Bulletin, v. 117, p. 747-763.

Ross, G.M., Parrish, R.R. and Dudás, F.Ö, 1991, Provenance of the Bonner Formation (Belt Supergroup), Montana: Insights from U-Pb and Sm-Nd analyses of detrital minerals: Geology, v. 19, p. 340-343.

Ross, G.M. and Villeneuve, M., 2003, Provenance of the Mesoproterozoic (1.45 Ga) Belt basin (western North America): Another piece in the pre-Rodinia paleogeographic puzzle: GSA Bulletin, v. 115, p. 1191-1217.

Ross, G. M., 1991, Tectonic setting of the Windemere Supergroup revisited: Geology, v. 19, p. 1125-1128.

Spear, F.S., Kohn, M.J. and Cheney, J.T., 1999, P-T paths from anatectic pelites: Contributions to Mineralogy and Petrology, v. 134, p. 17-32.

Stewart, E.D., Link, P.K., Fanning, M., Frost, C.D. and McCurry, M., 2010, Paleogeographic implications of non-North American sediment in the Mesoproterozoic upper Belt Supergroup and Lemhi Group, Idaho and Montana, USA: Geology, v. 38, p. 927-930.

Stipp, M., Holger, S., Renée, H. and Stefan, S.M., 2004, The eastern Tonale fault zone: a 'natural laboratory' for crystal plastic deformation of quartz over a range from 250 to 700 °C: Journal of Structural Geology, v. 24, p. 1861-1884.

Storm, L.C. and Spear, F.S., 2005, Pressure, temperature and cooling rates of granulite facies migmatitic pelites from the southern Adirondack Highlands, New York: Journal of Metamorphic Geology, v. 23, p. 107-130.

Vernon, R.H., 1987, Growth and concentration of fibrous sillimanite related to heterogeneous deformation in K-feldspar-sillimanite metapelites: Journal of Metamorphic Geology, v. 5, p. 51-68.

White, R.W., Powell, R., Holland, T.J.B., Johnson, T.E. and Green, E.C.R., 2014, New mineral activity-composition relations for thermodynamic calculations in metapelitic systems: Journal of Metamorphic Geology, v. 32, p. 261-286.

Whitmeyer, S.J. and Karlstrom, K.E., 2007, Tectonic model for the Proterozoic growth of North America: Geosphere, v. 3, p. 220-259.

Whitney, D.L. and Evans, B.W., 2010, Abbreviations for names of rock-forming minerals: American Mineralogist, v. 95, p. 185-187.

Whittington, J.K., 2002, Muscovite pseudomorphs after staurolite as a record of fluid infiltration during prograde metamorphism. Unpublished M.S. Thesis, LSU, Baton Rouge, LA. Williams, T.J., Piccoli, P.M., Candela, P.A., and Simon, A., 2004, Minerals and reactions in miarolitic cavities in the Eocene Sawtooth Batholiths, south-central Idaho: Geological Society of America Abstracts with Programs, v. 36, p. 69.

Wu, C-M. and Cheng, B-H., 2006, Valid garnet-biotite (GB) geothermometry and garnet-aluminum silicate-plagioclase-quartz (GASP) geobarometry in metapelitic rocks: Lithos, v. 89, p. 1-23.

Wu, C-M., Zhang, J. and Ren, L-D., 2004, Empirical Garnet-Biotite-Plagioclase-Quartz (GBPQ) Geobarometry in Medium-to High-Grade Metapelites: Journal of Petrology, v. 45, p. 1907-1921.

Wu, C-M, Zhang, J, and Ren, L-D, 2004, Empirical Garnet-Biotite-Plagioclase-Quartz (GBPQ) geobarometry in medium- to high-grade metapelites: Journal of Petrology, v. 45, p. 1907-1921.

APPENDIX A: EMPA ANALYSES-GARNET

Garnet						
Sample #	SMC-13-130	SMC-13-130	SMC-13-130	SMC-13-130	SMC-13-130	SMC-13-130
Analysis pt. #	G1-01	G1-02	G1-03	G1-04	G1-05	G1-06
SiO2	36.830	36.960	37.180	36.900	36.840	36.960
Al2O3	21.010	20.980	21.010	20.820	20.860	21.040
TiO2	0.024	0.001	0.005	0.000	0.000	0.008
Cr2O3	0.040	0.034	0.029	0.026	0.033	0.013
FeO (calculated)	0.000	0.000	0.000	0.000	0.000	0.000
MnO	32.450	33.410	33.400	32.730	32.700	33.540
MgO	5.360	3.980	5.110	5.160	5.250	4.500
CaO	2.280	2.680	2.360	2.370	2.370	2.530
Total	1.189	1.033	1.079	1.133	1.107	1.124
Structural formula based on 12 oxygens						
Z (iv) site: Si	3.000	3.000	3.000	3.000	3.000	2.998
Z (tet) site total	3.000	3.000	3.000	3.000	3.000	3.000
Al (total)	2.018	2.012	2.001	2.001	2.005	2.011
Fe2+ (total)	2.216	2.278	2.259	2.236	2.233	2.276
Mg2+(total)	0.277	0.326	0.285	0.289	0.289	0.306
Y (vi) site: Al	2.018	2.012	2.001	2.001	2.005	2.009
Cr3+	0.003	0.002	0.002	0.002	0.002	0.001
Si	0.007	0.013	0.007	0.014	0.008	0.000
Y (vi) site total	2.029	2.028	2.011	2.017	2.016	2.011
X-site (viii) Fe2+	2.216	2.278	2.259	2.236	2.233	2.276
Mn2+	0.371	0.275	0.350	0.357	0.363	0.309
Mg	0.277	0.326	0.285	0.289	0.289	0.306
Ca	0.104	0.090	0.094	0.099	0.097	0.098
Calculated % garnet species						

(APPENDIX A: CONTINUED)

Garnet							
Sample #	SMC-13-130	SMC-13-130	SMC-13-130	SMC-13-130	SM-13-130	SMC-13-130	SMC-13-130
Analysis pt. #	G2-01	G2-02	G2-03	G2-04	G2-05	G2-06	G2-07
SiO2	36.940	36.960	37.100	37.010	37.160	36.930	36.940
Al2O3	0.004	0.000	0.000	0.004	0.000	0.000	0.002
TiO2	0.005	0.015	0.000	0.015	0.028	0.024	0.017
Cr2O3	0.000	0.222	0.000	0.432	0.000	0.070	0.000
FeO (calculated)	32.760	33.970	33.990	33.721	34.450	33.437	33.080
MnO	5.450	3.720	3.320	3.950	2.330	4.580	5.230
MgO	2.280	2.800	2.930	2.880	3.320	2.550	2.330
CaO	1.318	1.144	1.186	1.095	1.309	1.201	1.238
Total	99.827	99.941	99.666	100.296	99.857	99.831	99.986
Z (iv) site: Si	2.997	2.987	3.000	2.981	2.992	2.992	2.992
Z (tet) site total	3.000	3.000	3.000	3.000	3.000	3.000	3.000
Al (total)	2.014	2.012	2.014	2.013	2.017	2.010	2.019
Fe2+ (total)	2.223	2.296	2.300	2.271	2.319	2.266	2.241
Mg2+(total)	0.276	0.337	0.353	0.346	0.398	0.308	0.281
Y (vi) site: Al	2.011	1.999	2.014	1.994	2.008	2.002	2.010
Cr3+	0.000	0.001	0.000	0.001	0.002	0.002	0.001
Si	0.000	0.000	0.001	0.000	0.000	0.000	0.000
Y (vi) site total	2.012	2.014	2.015	2.021	2.010	2.008	2.012
X-site (viii) Fe2+	2.223	2.296	2.300	2.271	2.319	2.266	2.241
Mn2+	0.375	0.255	0.227	0.269	0.159	0.314	0.359
Mg	0.276	0.337	0.353	0.346	0.398	0.308	0.281
Ca	0.115	0.099	0.103	0.094	0.113	0.104	0.107
Calculated % garnet species							
Almandine	74.094	76.540	76.652	75.705	77.312	75.528	74.688
Pyrope	9.192	11.246	11.778	11.525	13.281	10.268	9.377
Spessartine	12.484	8.489	7.583	8.981	5.296	10.478	11.959
Grossular	3.792	3.256	3.427	3.091	3.675	3.399	3.522

(APPENDIX A: CONTINUED)

Garnet

Sample #	SMC-13-119	SMC-13-119	SMC-13-119	SMC-13-119	SMC-13-119	SMC-13-119	SMC-13-119
Analysis pt. #	G-01	G-02	G-03	G-04	G-05	G-06	G-07
SiO2	37.570	37.380	37.870	37.740	37.550	36.900	37.370
Al2O3	21.430	21.080	21.440	21.350	21.250	21.180	21.210
TiO2	0.016	0.001	0.007	0.014	0.000	0.012	0.000
Cr2O3	0.000	0.245	0.000	0.000	0.062	0.399	0.000
FeO (calculated)	30.440	33.009	32.350	32.890	33.694	33.251	33.930
MnO	1.640	2.510	1.470	1.470	1.800	3.940	2.420
MgO	4.410	3.350	4.630	4.380	4.000	2.610	3.570
CaO	3.580	2.490	2.360	2.090	1.770	1.740	1.500
Total	99.100	100.083	100.127	99.943	100.143	100.032	100.000
Z (iv) site: Si	3.000	2.996	3.000	3.000	2.998	2.980	2.998
Z (tet) site total	3.000	3.000	3.000	3.000	3.000	3.000	3.000
Al (total)	2.016	1.992	2.003	2.003	2.000	2.018	2.005
Fe2+ (total)	2.034	2.213	2.146	2.191	2.249	2.245	2.276
Mg2+(total)	0.525	0.400	0.547	0.520	0.476	0.314	0.427
Y (vi) site: Al	2.016	1.988	2.003	2.003	1.997	1.997	2.003
Cr3+	0.001	0.000	0.000	0.001	0.000	0.001	0.000
Si	0.002	0.000	0.003	0.006	0.000	0.000	0.000
Y (vi) site total	2.020	2.004	2.007	2.010	2.002	2.022	2.003
X-site (viii) Fe2+	2.034	2.213	2.146	2.191	2.249	2.245	2.276
Mn2+	0.111	0.170	0.099	0.099	0.122	0.269	0.164
Mg	0.525	0.400	0.547	0.520	0.476	0.314	0.427
Ca	0.307	0.214	0.201	0.178	0.151	0.151	0.129
% garnet specie							
Almandine	67.813	73.750	71.520	73.028	74.980	74.849	75.879
Pyrope	17.513	13.342	18.246	17.336	15.867	10.473	14.232
Spessartine	3.700	5.680	3.291	3.306	4.057	8.982	5.481
Grossular	10.167	6.583	6.663	5.903	4.934	4.979	4.298

(APPENDIX A: CONTINUED)

Garnet						
Sample #	SMC-14-034	SMC-14-034	SMC-14-034	SMC-14-034	SMC-14-034	SMC-14-034
Analysis pt. #	G-01	G-02	G-03	G-04	G-05	G-06
SiO2	37.610	37.810	37.530	37.520	37.940	37.770
Al2O3	21.450	21.460	21.670	21.380	21.520	21.480
TiO2	0.008	0.000	0.003	0.012	0.031	0.003
Cr2O3	0.361	0.000	0.210	0.113	0.000	0.002
FeO (calculated)	33.575	33.190	33.041	34.038	33.000	33.418
MnO	0.987	0.908	0.938	0.987	0.995	0.873
MgO	4.720	4.980	5.010	4.410	5.150	4.960
CaO	1.560	1.540	1.530	1.540	1.530	1.580
Total	100.287	99.918	99.939	100.009	100.167	100.091
Z (iv) site: Si	2.985	3.000	2.979	2.991	3.000	2.996
Z (tet) site total	3.000	3.000	3.000	3.000	3.000	3.000
Al (total)	2.008	2.007	2.029	2.009	2.006	2.008
Fe2+ (total)	2.228	2.205	2.194	2.269	2.184	2.217
Mg2+(total)	0.558	0.590	0.593	0.524	0.608	0.586
Y (vi) site: Al	1.993	2.007	2.008	2.001	2.006	2.003
Cr3+	0.000	0.000	0.000	0.001	0.002	0.000
Si	0.000	0.003	0.000	0.000	0.003	0.000
Y (vi) site total	2.016	2.012	2.021	2.009	2.011	2.004
X-site (viii) Fe2+	2.228	2.205	2.194	2.269	2.184	2.217
Mn2+	0.066	0.061	0.063	0.067	0.067	0.059
Mg	0.558	0.590	0.593	0.524	0.608	0.586
Ca	0.133	0.131	0.130	0.132	0.130	0.134
Calculated % garnet species						
Almandine	74.281	73.486	73.123	75.649	72.804	73.886
Pyrope	18.614	19.655	19.764	17.471	20.253	19.548
Spessartine	2.211	2.036	2.103	2.222	2.224	1.954
Grossular	4.349	4.368	4.310	4.320	4.229	4.450

(APPENDIX A: CONTINUED)

Garnet							
Sample #	SMC-14-034	SMC-14-031	SMC-14-031	SMC-14-031	SMC-14-031	SMC-14-031	SMC-14-031
Analysis pt. #	G-07	G-01	G-02	G-03	G-04	G-05	G-06
SiO2	37.700	37.390	37.000	37.270	37.500	37.720	37.570
Al2O3	21.450	21.220	21.000	21.210	21.370	21.350	21.410
TiO2							
Cr2O3	0.009	0.000	0.010	0.018	0.025	0.000	0.018
FeO (calculated)	0.257	0.123	0.222	0.562	0.229	0.473	0.000
MnO	33.699	34.069	34.340	34.454	34.234	32.534	34.020
MgO	1.037	1.490	1.620	1.900	1.500	1.288	1.280
CaO	4.690	3.850	3.440	3.510	4.020	4.680	4.190
Total	1.550	1.770	1.670	1.520	1.500	2.300	1.620
	100.409	99.912	99.313	100.464	100.378	100.373	100.133
Z (iv) site: Si	2.989	2.995	2.992	2.981	2.989	2.988	2.995
Z (tet) site total	3.000	3.000	3.000	3.000	3.000	3.000	3.000
Al (total)	2.006	2.004	2.002	2.003	2.008	1.995	2.011
Fe2+ (total)	2.234	2.282	2.322	2.305	2.282	2.155	2.268
Mg2+(total)	0.554	0.460	0.415	0.419	0.478	0.553	0.498
Y (vi) site: Al	1.994	1.998	1.994	1.984	1.997	1.983	2.006
Cr3+	0.001	0.000	0.001	0.001	0.002	0.000	0.001
Si	0.000	0.000	0.000	0.000	0.000	0.000	0.000
Y (vi) site total	2.011	2.006	2.009	2.020	2.012	2.013	2.009
X-site (viii) Fe2+	2.234	2.282	2.322	2.305	2.282	2.155	2.268
Mn2+	0.070	0.101	0.111	0.129	0.101	0.086	0.086
Mg	0.554	0.460	0.415	0.419	0.478	0.553	0.498
Ca	0.132	0.152	0.145	0.130	0.128	0.195	0.138
Calculated % garnet species							
Almandine	74.478	76.069	77.402	76.835	76.058	71.837	75.602
Pyrope	18.477	15.323	13.821	13.953	15.921	18.420	16.598
Spessartine	2.321	3.369	3.698	4.291	3.375	2.881	2.882
Grossular	4.310	5.063	4.721	3.981	4.191	5.902	4.483

(APPENDIX A: CONTINUED)

Garnet					
Sample #	SMC-13-128	SMC-13-128	SMC-13-128	SMC-13-128	SMC-13-128
Analysis pt. #	G1-01	G1-02	G1-03	G1-04	G1-05
SiO2	37.200	37.240	37.210	37.260	37.120
Al2O3	21.240	21.210	21.300	21.310	21.010
TiO2	0.028	0.000	0.006	0.016	0.000
Cr2O3	0.111	0.000	0.687	0.698	0.000
FeO (calculated)	33.230	33.830	34.022	33.852	32.860
MnO	4.910	3.620	2.470	2.710	5.240
MgO	2.690	3.050	3.540	3.400	2.540
CaO	1.164	1.151	1.296	1.480	1.218
Total	100.581	100.103	100.530	100.726	99.998
Z (iv) site: Si	2.989	2.998	2.975	2.976	3.000
Z (tet) site total	3.000	3.000	3.000	3.000	3.000
Al (total)	2.012	2.012	2.011	2.009	2.002
Fe2+ (total)	2.233	2.278	2.275	2.261	2.223
Mg2+(total)	0.322	0.366	0.422	0.405	0.306
Y (vi) site: Al	2.002	2.010	1.986	1.985	2.002
Cr3+	0.002	0.000	0.000	0.001	0.000
Si	0.000	0.000	0.000	0.000	0.003
Y (vi) site total	2.011	2.010	2.028	2.028	2.005
X-site (viii) Fe2+	2.233	2.278	2.275	2.261	2.223
Mn2+	0.334	0.247	0.167	0.183	0.359
Mg	0.322	0.366	0.422	0.405	0.306
Ca	0.100	0.099	0.111	0.127	0.106
Calculated % garnet species					
Almandine	74.442	75.919	75.840	75.364	74.098
Pyrope	10.742	12.201	14.066	13.493	10.210
Spessartine	11.140	8.228	5.576	6.110	11.967
Grossular	3.227	3.304	3.660	4.103	3.517

(APPENDIX A: CONTINUED)

Garnet Normalization

Sample #	SMC-13-128	SMC-13-128	SMC-13-128	SMC-13-128	SMC-13-128	SMC-13-128
Analysis pt. #	G2-01	G2-02	G2-03	G2-04	G2-05	G2-06
SiO2	37.180	37.170	36.990	36.920	37.030	37.150
Al2O3	21.200	21.200	21.150	21.040	21.100	21.150
TiO2	0.015	0.020	0.000	0.013	0.000	0.017
Cr2O3	0.176	0.387	0.098	0.299	0.536	0.000
FeO (calculated)	33.441	32.782	33.412	33.571	32.598	31.990
MnO	5.410	5.240	5.310	5.290	5.460	5.180
MgO	2.190	2.510	2.140	2.030	2.430	2.320
CaO	1.275	1.480	1.279	1.254	1.420	1.312
Total	100.887	100.804	100.392	100.425	100.574	99.125
Z (iv) site: Si	2.990	2.984	2.989	2.987	2.982	3.000
Z (tet) site total	3.000	3.000	3.000	3.000	3.000	3.000
Al (total)	2.010	2.008	2.015	2.008	2.006	2.025
Fe2+ (total)	2.249	2.201	2.258	2.271	2.196	2.182
Mg2+(total)	0.263	0.300	0.258	0.245	0.292	0.282
Y (vi) site: Al	2.000	1.992	2.004	1.995	1.988	2.025
Cr3+	0.001	0.001	0.000	0.001	0.000	0.001
Si	0.000	0.000	0.000	0.000	0.000	0.030
Y (vi) site total	2.011	2.017	2.011	2.014	2.020	2.056
X-site (viii) Fe2+	2.249	2.201	2.258	2.271	2.196	2.182
Mn2+	0.368	0.356	0.363	0.362	0.372	0.358
Mg	0.263	0.300	0.258	0.245	0.292	0.282
Ca	0.110	0.127	0.111	0.109	0.123	0.115
Calculated % garnet species						
Almandine	74.961	73.361	75.265	75.713	73.187	72.724
Pyrope	8.751	10.013	8.593	8.161	9.725	9.401
Spessartine	12.282	11.876	12.115	12.083	12.415	11.926
Grossular	3.615	4.134	3.651	3.557	3.931	3.767

(APPENDIX A: CONTINUED)

Garnet							
Sample #	SMC-13-128	SMC-13-128	SMC-14-035	SMC-14-035	SMC-14-035	SMC-14-035	SMC-14-035
Analysis pt. #	G3-01	G3-02	G-01	G-02	G-03	G-04	G-05
SiO2	37.060	36.950	36.930	37.090	36.790	37.330	37.090
Al2O3	20.990	21.040	21.020	21.030	20.960	21.260	21.020
TiO2	0.020	0.321	0.047	0.017	0.013	0.039	0.008
Cr2O3	0.000	0.299	0.215	0.000	0.908	0.000	0.416
FeO (calculated)	32.930	32.941	34.086	33.890	33.813	34.380	33.616
MnO	5.550	5.560	3.880	3.400	4.150	2.480	4.270
MgO	2.420	2.400	2.600	2.850	2.520	3.200	2.720
CaO	1.140	1.040	1.198	1.156	1.179	1.199	1.218
Total	100.122	100.551	100.006	99.433	100.363	99.908	100.358
Z (iv) site: Si	2.998	2.981	2.988	3.000	2.972	3.000	2.989
Z (tet) site total	3.000	3.000	3.000	3.000	3.000	3.000	3.000
Al (total)	2.001	2.002	2.005	2.008	2.000	2.015	1.998
Fe2+ (total)	2.228	2.222	2.306	2.300	2.285	2.315	2.266
Mg2+(total)	0.292	0.289	0.314	0.345	0.304	0.384	0.327
Y (vi) site: Al	1.999	1.982	1.993	2.008	1.973	2.015	1.987
Cr3+	0.001	0.020	0.003	0.001	0.001	0.002	0.000
Si	0.000	0.000	0.000	0.009	0.000	0.006	0.000
Y (vi) site total	2.001	2.021	2.011	2.019	2.031	2.025	2.013
X-site (viii) Fe2+	2.228	2.222	2.306	2.300	2.285	2.315	2.266
Mn2+	0.380	0.380	0.266	0.234	0.284	0.169	0.291
Mg	0.292	0.289	0.314	0.345	0.304	0.384	0.327
Ca	0.099	0.090	0.104	0.100	0.102	0.103	0.105
Calculated % garnet species							
Almandine	74.261	74.074	76.881	76.654	76.153	77.181	75.518
Pyrope	9.728	9.620	10.453	11.491	10.117	12.806	10.892
Spessartine	12.676	12.662	8.863	7.789	9.466	5.639	9.715
Grossular	3.191	1.974	3.222	3.296	2.666	3.324	3.142

(APPENDIX A: CONTINUED)

Garnet						
Sample #	SMC-14-039	SMC-14-039	SMC-14-039	SMC-14-039	SMC-14-039	SMC-14-039
Analysis pt. #	G-01	G-02	G-03	G-04	G-05	G-06
SiO2	37.030	36.940	37.130	37.090	37.000	37.390
Al2O3	21.080	21.120	21.040	21.130	21.110	21.080
TiO2	0.027	0.120	0.000	0.046	0.035	0.029
Cr2O3	0.153	1.104	0.301	0.000	0.762	0.000
FeO (calculated)	33.382	33.176	33.759	34.000	33.464	33.950
MnO	4.950	4.990	4.630	4.240	4.690	4.190
MgO	2.350	2.350	2.380	2.250	2.350	2.530
CaO	1.322	1.369	1.332	1.293	1.440	1.460
Total	100.295	101.171	100.572	100.062	100.857	100.646
Z (iv) site: Si	2.991	2.964	2.992	3.000	2.975	3.000
Z (tet) site total	3.000	3.000	3.000	3.000	3.000	3.000
Al (total)	2.008	2.003	2.000	2.014	2.004	1.996
Fe2+ (total)	2.255	2.226	2.275	2.302	2.250	2.282
Mg2+(total)	0.283	0.281	0.286	0.272	0.282	0.303
Y (vi) site: Al	1.999	1.967	1.991	2.014	1.980	1.996
Cr3+	0.002	0.008	0.000	0.003	0.002	0.002
Si	0.000	0.000	0.000	0.003	0.000	0.005
Y (vi) site total	2.010	2.041	2.010	2.021	2.028	2.003
X-site (viii) Fe2+	2.255	2.226	2.275	2.302	2.250	2.282
Mn2+	0.339	0.339	0.316	0.291	0.319	0.285
Mg	0.283	0.281	0.286	0.272	0.282	0.303
Ca	0.114	0.118	0.115	0.112	0.124	0.126
Calculated % garnet species						
Almandine	75.167	74.210	75.832	76.743	75.012	76.057
Pyrope	9.432	9.370	9.530	9.053	9.390	10.103
Spessartine	11.289	11.305	10.533	9.693	10.647	9.507
Grossular	3.729	3.184	3.602	3.592	3.738	4.098

(APPENDIX A: CONTINUED)

Garnet						
Sample #	SMC-13-118	SMC-13-118	SMC-13-118	SMC-13-118	SMC-13-118	SMC-13-118
Analysis pt. #	G1-01	G1-02	G1-03	G1-04	G1-05	G1-06
Comment	37.910	37.870	37.810	37.340	37.200	37.600
SiO2	21.480	21.510	21.420	21.240	21.210	21.340
Al2O3	0.017	0.030	0.004	0.017	0.000	0.000
TiO2	0.014	0.028	0.042	0.000	0.027	0.015
Cr2O3	0.290	0.672	0.700	0.677	0.064	0.012
FeO (calculated)	29.719	28.956	30.250	31.431	32.843	32.859
MnO	2.680	2.950	2.550	3.080	4.430	2.600
MgO	4.240	4.020	4.100	3.230	2.920	3.680
CaO	4.180	4.840	3.960	3.400	1.520	2.270
Total	100.530	100.875	100.836	100.414	100.213	100.376
Z (iv) site: Si	2.991	2.980	2.982	2.980	2.992	2.997
Z (tet) site total	3.000	3.000	3.000	3.000	3.000	3.000
Al (total)	1.999	1.998	1.995	2.001	2.011	2.005
Fe2+ (total)	1.961	1.906	1.995	2.098	2.209	2.190
Mg2+(total)	0.499	0.472	0.482	0.384	0.350	0.437
Y (vi) site: Al	1.990	1.978	1.977	1.981	2.003	2.002
Cr3+	0.001	0.002	0.003	0.000	0.002	0.001
Si	0.000	0.000	0.000	0.000	0.000	0.000
Y (vi) site total	2.009	2.022	2.021	2.023	2.008	2.003
X-site (viii) Fe2+	1.961	1.906	1.995	2.098	2.209	2.190
Mn2+	0.179	0.197	0.170	0.208	0.302	0.176
Mg	0.499	0.472	0.482	0.384	0.350	0.437
Ca	0.353	0.408	0.335	0.291	0.131	0.194
Calculated % garnet species						
Almandine	65.367	63.518	66.510	69.923	73.636	73.008
Pyrope	16.624	15.719	16.069	12.809	11.670	14.575
Spessartine	5.970	6.554	5.678	6.939	10.059	5.851
Grossular	11.471	12.954	10.403	9.206	4.280	6.415

(APPENDIX A: CONTINUED)

Garnet			
Sample #	SMC-13-118	SMC-13-118	SMC-13-118
Analysis pt. #	G2-01	G2-02	G2-03
SiO2	36.950	37.060	37.010
Al2O3	21.030	21.130	20.960
TiO2	0.033	0.020	0.027
Cr2O3	0.372	1.090	0.607
FeO (calculated)	32.575	32.629	32.564
MnO	4.600	4.670	5.160
MgO	2.880	2.860	2.610
CaO	1.430	1.450	1.420
Total	99.889	100.909	100.365
Z (iv) site: Si	2.985	2.969	2.984
Z (tet) site total	3.000	3.000	3.000
Al (total)	2.004	2.001	1.995
Fe2+ (total)	2.201	2.186	2.196
Mg2+(total)	0.347	0.342	0.314
Y (vi) site: Al	1.990	1.969	1.979
Cr3+	0.002	0.001	0.002
Si	0.000	0.000	0.000
Y (vi) site total	2.015	2.037	2.018
X-site (viii) Fe2+	2.201	2.186	2.196
Mn2+	0.315	0.317	0.352
Mg	0.347	0.342	0.314
Ca	0.124	0.124	0.123
Calculated % garnet species			
Almandine	73.367	72.869	73.198
Pyrope	11.562	11.385	10.458
Spessartine	10.493	10.563	11.747
Grossular	3.965	3.384	3.408

APPENDIX B: EMPA ANALYSES-PLAGIOCLASE

Plagioclase

Sample #	SMC-14-035	SMC-14-035	SMC-14-035	SMC-14-035	SMC-14-039	SMC-14-039	SMC-14-039	SMC-14-039	SMC-14-039
Analysis pt. #	plag1	plag2-01	plag2-02	plag2-03	Plag1-01	plag1-02	plag1-03	plag2-04	plag2-05
SiO_2	65.53	64.19	63.83	63.76	65.04	64.63	64.86	64.54	65.55
Al_2O_3	22.24	23.20	23.43	23.03	22.66	22.72	22.70	22.88	22.96
FeO	0.07	0.04	0.02	0.06	0.02	0.03	bd	bd	bd
CaO	2.87	3.92	4.17	3.86	3.25	3.41	3.33	3.49	3.51
BaO	bd	0.02	0.03	bd	bd	0.03	bd	bd	bd
Na_2O	10.06	9.42	9.33	9.41	9.80	9.67	9.62	9.56	9.46
K_2O	0.21	0.15	0.18	0.15	0.07	0.07	0.06	0.09	0.08
Total	100.98	100.94	101.00	100.27	100.84	100.56	100.57	100.56	101.56
	Structural formula based on 8 oxygens								
T (iv) site: Si	2.858	2.808	2.794	2.808	2.840	2.833	2.839	2.828	2.840
Al	1.143	1.196	1.209	1.195	1.166	1.174	1.171	1.181	1.172
Fe^{3+}									
T site total	4.002	4.004	4.003	4.004	4.007	4.006	4.010	4.009	4.012
Fe2+	0.003	0.001	0.001	0.002	0.001	0.001	bd	bd	bd
Ca	0.134	0.184	0.196	0.182	0.152	0.160	0.156	0.164	0.163
Ba		0.000	0.001			0.001			
Na	0.851	0.799	0.792	0.804	0.830	0.822	0.816	0.812	0.795
K	0.011	0.008	0.010	0.009	0.004	0.004	0.004	0.005	0.004
M-site total	0.996	0.991	0.998	0.994	0.986	0.986	0.976	0.981	0.962
Main feldspar components									
albite (mol%)	85.39	80.59	79.32	80.81	84.18	83.32	83.64	82.78	82.63
anorthite (mol%)	13.46	18.53	19.59	18.32	15.43	16.24	16.00	16.70	16.94
orthoclase (mol%)	1.15	0.85	1.03	0.88	0.39	0.39	0.37	0.52	0.43
celsian (mol%)	bd	0.03	0.06	bd	bd	0.06	bd	bd	bd

(APPENDIX B: CONTINUED)

Plagioclase

Sample #	SMC-13-118	SMC-13-118	SMC-13-118	SMC-13-118	SMC-13-118	SMC-13-118	SMC-13-118	SMC-13-118	SMC-13-118
Analysis pt. #	plag1-01	plag1-02	plag1-03	plag1-04	gplag-01	gplag-02	gplag-03	gplag-04	plag2-05
SiO_2	61.09	60.70	60.58	60.61	54.32	55.35	55.27	55.09	60.54
Al_2O_3	25.08	25.25	25.21	25.29	29.50	28.61	29.09	28.55	25.33
FeO	0.04	0.03	bd	bd	bd	0.04	0.11	0.09	0.02
CaO	6.28	6.52	6.53	6.40	11.40	10.51	10.80	10.37	6.54
BaO	0.09	0.17	bd	bd	bd	0.03	bd	bd	0.02
Na_2O	7.90	7.90	7.75	7.81	4.92	5.45	5.35	5.54	7.75
K_2O	0.09	0.07	0.07	0.14	0.04	0.05	0.04	0.08	0.11
Total	100.57	100.64	100.14	100.25	100.18	100.05	100.66	99.72	100.31
T (iv) site: Si	2.700	2.685	2.688	2.687	2.444	2.489	2.472	2.486	2.684
Al	1.306	1.317	1.318	1.321	1.564	1.516	1.534	1.519	1.323
Fe^{3+}									
T site total	4.006	4.002	4.007	4.008	4.008	4.005	4.006	4.005	4.007
Fe2+	0.001	0.001	bd	bd	bd	0.002	0.004	0.004	0.001
Ca	0.297	0.309	0.310	0.304	0.550	0.506	0.518	0.501	0.311
Ba	0.002	0.003	bd	bd	bd	0.001	bd	bd	0.000
Na	0.677	0.678	0.667	0.671	0.429	0.475	0.464	0.485	0.666
K	0.005	0.004	0.004	0.008	0.002	0.003	0.002	0.005	0.006
M-site total	0.981	0.994	0.981	0.983	0.981	0.985	0.984	0.991	0.983
Main feldspar components									
albite (mol%)	69.01	68.21	67.94	68.29	43.76	48.23	47.16	48.93	67.73
anorthite (mol%)	30.32	31.11	31.64	30.92	56.03	51.40	52.61	50.61	31.58
orthoclase (mol%)	0.51	0.38	0.42	0.79	0.21	0.31	0.22	0.46	0.66
celsian (mol%)	0.16	0.30	bd	bd	bd	0.06	bd	bd	0.03

(APPENDIX B: CONTINUED)

Plagioclase

Sample #	SMC-13-118	SMC-13-118	SMC-13-118	SMC-13-118	SMC-13-118	SMC-13-128	SMC-13-128	SMC-13-128	SMC-13-128
Analysis pt. #	plag2-06	plag2-07	plag3-08	plag3-09	plag4-10	plag1-02	plag1-03	plag1-04	plag2-05
SiO_2	61.88	63.43	62.60	62.67	62.33	63.55	63.85	63.28	63.47
Al_2O_3	23.78	24.20	24.02	24.20	24.38	23.90	23.82	24.01	23.83
FeO	0.00	0.01	0.01	bd	0.01	0.01	bd	0.01	0.01
CaO	4.76	5.14	5.10	5.16	5.40	4.79	4.72	4.85	4.78
BaO	0.04	bd	0.06	0.12	0.02	bd	bd	0.01	bd
Na_2O	8.70	8.60	8.56	8.61	8.34	8.68	8.70	8.66	8.70
K_2O	0.10	0.08	0.07	0.09	0.10	0.11	0.16	0.10	0.10
Total	99.26	101.46	100.42	100.85	100.59	101.04	101.25	100.92	100.90
T (iv) site: Si	2.759	2.765	2.759	2.753	2.744	2.778	2.785	2.771	2.779
Al	1.250	1.243	1.248	1.253	1.265	1.232	1.225	1.239	1.230
Fe^{3+}									
T site total	4.009	4.008	4.007	4.006	4.009	4.010	4.010	4.011	4.009
Fe2+	0.000	0.000	0.000	bd	0.001	0.000	bd	0.000	0.000
Ca	0.227	0.240	0.241	0.243	0.255	0.224	0.221	0.228	0.224
Ba	0.001	bd	0.001	0.002	0.000	bd	bd	0.000	bd
Na	0.752	0.727	0.732	0.733	0.712	0.736	0.736	0.735	0.739
K	0.006	0.004	0.004	0.005	0.006	0.006	0.009	0.006	0.006
M-site total	0.986	0.971	0.978	0.983	0.973	0.966	0.965	0.969	0.969
Main feldspar components									
albite (mol%)	76.28	74.83	74.83	74.57	73.19	76.13	76.23	75.90	76.25
anorthite (mol%)	23.06	24.71	24.64	24.70	26.19	23.22	22.85	23.49	23.15
orthoclase (mol%)	0.58	0.46	0.43	0.51	0.58	0.65	0.92	0.59	0.60
celsian (mol%)	0.07	bd	0.11	0.21	0.04	bd	bd	0.02	bd

(APPENDIX B: CONTINUED)

Plagioclase

Sample #	SMC-13-128	SMC-13-128	SMC-13-128	SMC-13-128	SMC-13-128	SMC-13-128	SMC-13-128	SMC-13-128	SMC-13-128
Analysis pt. #	plag2-06	plag2-07	plag3-08	plag3-09	plag3-10	plag3-11	plag4-12	plag4-13	plag4-14
SiO_2	64.07	64.24	63.64	63.86	63.32	63.48	61.71	62.10	62.22
Al_2O_3	23.88	23.99	24.47	24.27	24.20	24.37	24.55	24.40	23.94
FeO	0.01	0.01	bd	0.04	bd	0.03	0.02	0.04	0.02
CaO	4.74	4.74	5.11	5.13	5.11	5.16	5.59	5.43	5.16
BaO	0.04	bd	0.03	bd	bd	0.05	0.06	bd	bd
Na_2O	8.75	8.78	8.62	8.54	8.51	8.51	8.33	8.44	8.59
K_2O	0.10	0.10	0.08	0.09	0.10	0.09	0.06	0.08	0.08
Total	101.59	101.85	101.96	101.92	101.24	101.69	100.32	100.49	100.01
T (iv) site: Si	2.786	2.785	2.760	2.769	2.765	2.761	2.728	2.738	2.755
Al	1.224	1.226	1.251	1.240	1.245	1.249	1.279	1.268	1.249
Fe^{3+}									
T site total	4.009	4.010	4.011	4.010	4.010	4.010	4.007	4.007	4.004
Fe2+	0.000	0.000	bd	0.001	bd	0.001	0.001	0.001	0.001
Ca	0.221	0.220	0.237	0.238	0.239	0.240	0.265	0.257	0.245
Ba	0.001	bd	0.001	bd	bd	0.001	0.001	bd	bd
Na	0.738	0.738	0.725	0.718	0.720	0.718	0.714	0.722	0.737
K	0.006	0.005	0.005	0.005	0.005	0.005	0.003	0.004	0.004
M-site total	0.965	0.963	0.967	0.961	0.965	0.964	0.983	0.983	0.987
Main feldspar components									
albite (mol%)	76.44	76.59	74.92	74.70	74.66	74.45	72.63	73.44	74.74
anorthite (mol%)	22.88	22.85	24.54	24.80	24.78	24.95	26.93	26.11	24.81
orthoclase (mol%)	0.60	0.56	0.47	0.50	0.56	0.52	0.34	0.44	0.45
celsian (mol%)	0.07	bd	0.06	bd	bd	0.08	0.10	bd	bd

(APPENDIX B: CONTINUED)

Sample #	SMC-13-128	SMC-13-128	SMC-13-128	SMC-13-128	SMC-13-128	SMC-13-128	SMC-13-128	SMC-13-128	SMC-13-128
Analysis pt. #	plag5-15	plag5-16	plag5-17	plag6-18	plag6-19	plag6-20	gplag1-21	gplag1-22	gplag1-23
SiO_2	62.73	61.68	61.94	62.40	63.40	62.73	58.18	57.87	60.19
Al_2O_3	23.87	24.45	24.23	24.04	23.61	23.94	27.26	27.23	25.79
FeO	0.01	0.03	bd	bd	0.01	0.02	0.19	0.10	0.31
CaO	4.87	5.42	5.34	5.01	4.61	4.78	8.53	8.63	7.00
BaO	0.04	0.02	0.05	0.02	0.03	0.06	0.02	0.01	0.12
Na_2O	8.76	8.37	8.35	8.74	8.86	8.72	6.56	6.40	7.61
K_2O	0.10	0.08	0.09	0.07	0.08	0.07	0.08	0.09	0.06
Total	100.38	100.05	99.99	100.28	100.61	100.32	100.82	100.32	101.08
T (iv) site: Si	2.766	2.732	2.744	2.755	2.785	2.766	2.582	2.580	2.657
Al	1.240	1.276	1.265	1.251	1.222	1.244	1.426	1.431	1.342
Fe^{3+}									
T site total	4.006	4.009	4.009	4.006	4.007	4.010	4.007	4.010	3.999
Fe2+	0.000	0.001	bd	bd	0.000	0.001	0.007	0.004	0.011
Ca	0.230	0.257	0.253	0.237	0.217	0.226	0.406	0.412	0.331
Ba	0.001	0.000	0.001	0.000	0.001	0.001	0.000	0.000	0.002
Na	0.749	0.719	0.717	0.748	0.754	0.745	0.564	0.553	0.651
K	0.006	0.005	0.005	0.004	0.005	0.004	0.005	0.005	0.004
M-site total	0.985	0.981	0.976	0.989	0.977	0.976	0.975	0.970	0.988
Main feldspar components									
albite (mol%)	75.99	73.28	73.45	75.61	77.24	76.34	57.89	57.00	65.92
anorthite (mol%)	23.35	26.22	25.96	23.95	22.21	23.13	41.60	42.47	33.51
orthoclase (mol%)	0.59	0.46	0.51	0.40	0.49	0.43	0.47	0.52	0.37
celsian (mol%)	0.07	0.03	0.08	0.03	0.06	0.10	0.04	0.01	0.20

(APPENDIX B: CONTINUED)

Plagioclase

Sample #	SMC-13-130	SMC-13-130	SMC-13-130	SMC-13-130	SMC-13-130	SMC-13-130	SMC-13-130	SMC-13-130	SMC-13-130	SMC-13-130
Analysis pt. #	plag1-01	plag1-02	plag1-03	plag1-04	plag1-05	plag2-06	plag2-07	plag2-08	plag2-09	gplag1-10
SiO_2	62.93	63.13	63.21	63.81	63.97	62.50	63.91	65.16	64.79	64.79
Al_2O_3	23.10	23.18	23.17	22.66	22.86	23.52	23.01	22.22	22.47	23.02
FeO	0.15	0.01	0.00	bd	0.03	0.03	bd	0.03	0.08	0.32
CaO	4.22	4.25	4.16	3.63	3.70	4.58	4.00	3.12	3.30	3.72
BaO	0.05	0.03	bd	0.05	0.28	0.02	bd	bd	0.02	bd
Na_2O	9.19	9.15	9.19	9.46	9.47	8.93	9.21	9.74	9.71	9.52
K_2O	0.12	0.11	0.12	0.15	0.14	0.11	0.12	0.13	0.10	0.07
Total	99.75	99.87	99.85	99.75	100.45	99.69	100.25	100.39	100.47	101.43
T (iv) site: Si	2.792	2.794	2.797	2.823	2.816	2.774	2.812	2.857	2.842	2.820
Al	1.208	1.209	1.208	1.181	1.186	1.230	1.193	1.148	1.162	1.181
Fe^{3+}										
T site total	3.999	4.003	4.005	4.004	4.002	4.004	4.006	4.005	4.003	4.001
Fe2+	0.005	0.000	0.000	bd	0.001	0.001	bd	0.001	0.003	0.012
Ca	0.201	0.202	0.197	0.172	0.175	0.218	0.189	0.147	0.155	0.173
Ba	0.001	0.001	bd	0.001	0.005	0.000			0.000	
Na	0.790	0.785	0.788	0.811	0.808	0.768	0.786	0.828	0.826	0.803
K	0.007	0.006	0.007	0.008	0.008	0.006	0.007	0.007	0.006	0.004
M-site total	0.998	0.994	0.992	0.993	0.996	0.993	0.981	0.981	0.987	0.981
Main feldspar components										
albite (mol%)	79.17	79.01	79.45	81.74	81.18	77.40	80.07	84.35	83.69	81.93
anorthite (mol%)	20.09	20.28	19.87	17.33	17.53	21.94	19.22	14.93	15.72	17.69
orthoclase (mol%)	0.66	0.65	0.68	0.84	0.81	0.62	0.71	0.71	0.56	0.37
celsian (mol%)	0.08	0.06	bd	0.08	0.48	0.04	bd	bd	0.03	bd

(APPENDIX B: CONTINUED)

Plagioclase

Sample #	SMC-13-130	SMC-13-130	SMC-13-130	SMC-13-130	SMC-13-130	SMC-13-130	SMC-13-130	SMC-13-130	SMC-13-130	SMC-13-130
Analysis pt. #	plag3-11	plag3-12	plag3-13	plag3-14	plag3-15	plag4-16	plag4-17	plag4-18	plag4-19	plag4-20
SiO_2	64.50	64.36	63.99	62.46	63.15	62.43	63.14	63.09	63.35	63.33
Al_2O_3	22.91	22.89	23.16	24.27	23.02	23.06	23.00	23.25	23.14	23.28
FeO	0.10	0.15	0.00	bd	0.32	0.06	bd	0.06	bd	bd
CaO	3.72	3.73	4.13	5.28	3.98	4.07	4.14	4.29	4.25	4.30
BaO	bd	bd	bd	bd	0.03	bd	0.05	0.05	0.04	0.04
Na_2O	9.54	9.53	9.21	8.55	9.28	9.14	9.04	8.91	9.09	9.11
K_2O	0.09	0.06	0.08	0.06	0.10	0.09	0.22	0.20	0.18	0.16
Total	100.86	100.73	100.58	100.62	99.88	98.84	99.59	99.86	100.05	100.22
T (iv) site: Si	2.822	2.820	2.808	2.748	2.797	2.791	2.802	2.793	2.798	2.793
Al	1.181	1.182	1.198	1.259	1.202	1.215	1.203	1.213	1.205	1.210
Fe^{3+}										
T site total	4.003	4.002	4.005	4.007	3.999	4.006	4.004	4.006	4.003	4.004
Fe2+	0.004	0.006	0.000	bd	0.012	0.002	bd	0.002	bd	bd
Ca	0.174	0.175	0.194	0.249	0.189	0.195	0.197	0.203	0.201	0.203
Ba	bd	bd	bd	bd	0.000	bd	0.001	0.001	0.001	0.001
Na	0.809	0.810	0.783	0.729	0.797	0.792	0.778	0.765	0.779	0.779
K	0.005	0.004	0.005	0.003	0.006	0.005	0.012	0.011	0.010	0.009
M-site total	0.989	0.988	0.982	0.982	0.992	0.992	0.988	0.980	0.990	0.992
Main feldspar components										
albite (mol%)	81.84	81.92	79.76	74.31	80.33	79.85	78.74	77.99	78.62	78.54
anorthite (mol%)	17.64	17.72	19.77	25.36	19.04	19.65	19.93	20.75	20.31	20.49
orthoclase (mol%)	0.52	0.36	0.47	0.33	0.58	0.50	1.26	1.16	1.00	0.91
celsian (mol%)	bd	bd	bd	bd	0.05	bd	0.08	0.09	0.07	0.07

(APPENDIX B: CONTINUED)

Plagioclase

Sample #	SMC-13-130	SMC-13-119	SMC-13-119	SMC-13-119	SMC-13-119	SMC-13-119	SMC-13-119	SMC-13-119	SMC-13-119	SMC-13-119
Analysis pt. #	plag4-21	plag1-01	plag1-02	plag1-03	plag1-04	plag1-05	plag2-06	plag2-07	plag2-08	gplag1-09
SiO_2	62.21	60.13	60.50	60.70	60.00	59.68	59.44	58.94	60.70	59.35
Al_2O_3	23.89	26.13	25.44	25.25	25.58	25.79	25.41	25.95	25.35	25.97
FeO	bd	0.01	0.71	0.02	0.02	0.03	0.05	bd	0.22	0.04
CaO	4.88	6.58	6.59	6.53	6.78	7.23	6.74	7.09	6.50	7.34
BaO	0.02	6.95	0.09	bd	0.09	bd	bd	1.99	bd	0.23
Na_2O	8.83	7.84	7.79	7.66	7.62	7.17	7.70	7.45	7.86	7.39
K_2O	0.09	0.12	0.10	0.13	0.14	0.11	0.11	0.14	0.14	0.08
Total	99.92	107.76	101.21	100.29	100.23	100.01	99.45	101.56	100.77	100.40
T (iv) site: Si	2.757	2.616	2.670	2.689	2.666	2.656	2.663	2.628	2.682	2.641
Al	1.248	1.340	1.323	1.319	1.340	1.353	1.341	1.363	1.320	1.362
Fe^{3+}										
T site total	4.005	3.955	3.993	4.008	4.006	4.009	4.004	3.991	4.002	4.002
Fe2+	bd	0.000	0.026	0.001	0.001	0.001	0.002	bd	0.008	0.001
Ca	0.232	0.307	0.312	0.310	0.323	0.345	0.323	0.339	0.308	0.350
Ba	0.000	0.118	0.001	bd	0.002	bd	bd	0.035	bd	0.004
Na	0.759	0.661	0.667	0.658	0.657	0.619	0.669	0.644	0.673	0.637
K	0.005	0.006	0.006	0.007	0.008	0.006	0.006	0.008	0.008	0.005
M-site total	0.996	1.093	0.985	0.975	0.989	0.970	0.998	1.025	0.989	0.996
Main feldspar components										
albite (mol%)	76.18	60.51	67.66	67.45	66.40	63.82	66.99	62.80	68.08	64.00
anorthite (mol%)	23.27	28.06	31.63	31.78	32.65	35.56	32.40	33.03	31.11	35.13
orthoclase (mol%)	0.51	0.59	0.56	0.77	0.79	0.62	0.61	0.79	0.81	0.47
celsian (mol%)	0.04	10.84	0.15	bd	0.16	bd	bd	3.39	bd	0.39

(APPENDIX B: CONTINUED)

Plagioclase

Sample #	SMC-13-119	SMC-13-119	SMC-13-119	SMC-13-119	SMC-13-119	SMC-13-119	SMC-13-119	SMC-13-119	SMC-13-119	SMC-13-119
Analysis pt. #	gplag1-10	gplag2-11	gplag2-12	plag3-13	plag3-14	plag3-15	plag3-16	plag4-17	plag4-18	plag4-19
SiO_2	59.24	58.47	57.98	60.96	60.28	59.46	60.03	60.01	60.11	60.41
Al_2O_3	26.03	26.13	26.16	25.19	25.37	25.45	25.31	25.20	25.29	25.18
FeO	0.26	0.05	0.06	0.01	0.02	bd	0.02	0.08	bd	bd
CaO	7.42	7.81	7.81	6.37	6.68	6.68	6.57	6.59	6.64	6.42
BaO	0.02	bd	bd	0.02	bd	bd	bd	0.13	bd	0.09
Na_2O	7.29	7.03	6.95	7.93	7.68	7.65	7.78	7.84	7.63	7.78
K_2O	0.08	0.08	0.08	0.11	0.10	0.11	0.10	0.07	0.10	0.14
Total	100.35	99.57	99.03	100.59	100.12	99.35	99.81	99.91	99.77	100.03
T (iv) site: Si	2.636	2.622	2.615	2.693	2.678	2.664	2.676	2.676	2.679	2.687
Al	1.365	1.381	1.390	1.312	1.328	1.344	1.330	1.324	1.328	1.320
Fe^{3+}										
T site total	4.001	4.003	4.005	4.005	4.006	4.008	4.006	4.001	4.007	4.006
Fe2+	0.010	0.002	0.002	0.000	0.001	bd	0.001	0.003	bd	bd
Ca	0.354	0.375	0.377	0.302	0.318	0.321	0.314	0.315	0.317	0.306
Ba	0.000	bd	bd	0.000	bd	bd	bd	0.002	bd	0.002
Na	0.629	0.611	0.608	0.679	0.661	0.665	0.672	0.678	0.659	0.671
K	0.005	0.005	0.004	0.006	0.006	0.006	0.006	0.004	0.006	0.008
M-site total	0.988	0.991	0.989	0.987	0.985	0.991	0.992	0.999	0.982	0.987
Main feldspar components										
albite (mol%)	63.67	61.67	61.42	68.81	67.15	67.03	67.79	67.86	67.12	68.00
anorthite (mol%)	35.81	37.86	38.14	30.55	32.28	32.35	31.63	31.52	32.28	31.01
orthoclase (mol%)	0.48	0.47	0.44	0.61	0.57	0.62	0.58	0.39	0.60	0.83
celsian (mol%)	0.04	bd	bd	0.03	bd	bd	bd	0.22	bd	0.16

(APPENDIX B: CONTINUED)

Plagioclase

Sample #	SMC-13-119	SMC-13-119	SMC-14-034	SMC-14-034	SMC-14-034	SMC-14-034	SMC-14-034	SMC-14-034	SMC-14-034
Analysis pt. #	plag4-20	plag4-21	plag1-01	plag1-02	plag1-03	plag2-04	plag2-05	plag2-06	plag2-07
SiO_2	60.69	60.43	59.79	59.85	60.16	59.52	59.39	59.01	60.34
Al_2O_3	25.01	25.14	25.37	25.41	25.46	25.13	25.15	25.09	25.25
FeO	0.04	0.02	0.09	0.08	0.11	0.03	0.02	0.02	0.04
CaO	6.31	6.43	6.84	6.79	6.74	6.52	6.67	6.58	6.56
BaO	0.05	bd	bd	0.02	0.01	0.02	bd	bd	0.05
Na_2O	7.84	7.80	7.53	7.48	7.48	7.58	7.55	7.57	7.60
K_2O	0.15	0.16	0.18	0.18	0.20	0.19	0.21	0.20	0.20
Total	100.10	99.99	99.81	99.82	100.16	98.98	98.99	98.46	100.05
T (iv) site: Si	2.696	2.688	2.668	2.670	2.673	2.676	2.671	2.669	2.683
Al	1.309	1.318	1.334	1.336	1.333	1.331	1.333	1.337	1.323
Fe^{3+}									
T site total	4.005	4.005	4.003	4.006	4.007	4.007	4.005	4.006	4.007
Fe2+	0.002	0.001	0.003	0.003	0.004	0.001	0.001	0.001	0.002
Ca	0.300	0.306	0.327	0.325	0.321	0.314	0.321	0.319	0.313
Ba	0.001	bd	bd	0.000	0.000	0.000	bd	bd	0.001
Na	0.675	0.673	0.652	0.647	0.644	0.661	0.658	0.664	0.655
K	0.009	0.009	0.010	0.010	0.011	0.011	0.012	0.011	0.012
M-site total	0.985	0.988	0.989	0.982	0.977	0.986	0.992	0.994	0.980
Main feldspar components									
albite (mol%)	68.55	68.05	65.88	65.86	65.98	67.02	66.38	66.78	66.85
anorthite (mol%)	30.49	31.00	33.07	33.04	32.86	31.86	32.41	32.08	31.89
orthoclase (mol%)	0.87	0.95	1.05	1.06	1.14	1.08	1.22	1.15	1.17
celsian (mol%)	0.09	bd	bd	0.04	0.02	0.04	bd	bd	0.09

(APPENDIX B: CONTINUED)

Plagioclase

Sample #	SMC-14-034	SMC-14-034	SMC-14-034	SMC-14-034	SMC-14-034	SMC-14-034	SMC-14-031	SMC-14-031	SMC-14-031
Analysis pt. #	plag2-09	plag2-10	plag3-11	plag3-12	plag3-13	plag3-14	gplag1-01	gplag1-02	gplag1-03
SiO_2	60.28	60.25	59.67	59.72	60.08	59.73	58.18	58.35	58.77
Al_2O_3	25.35	25.39	25.22	25.23	25.17	25.21	26.49	26.48	26.34
FeO	0.03	0.02	0.00	0.02	0.02	0.05	0.06	0.03	0.10
CaO	6.62	6.64	6.58	6.58	6.65	6.61	8.03	8.09	7.78
BaO	bd	bd	bd	bd	bd	0.01	bd	0.07	0.05
Na_2O	7.54	7.64	7.49	7.63	7.57	7.54	6.90	6.90	7.01
K_2O	0.19	0.19	0.17	0.17	0.18	0.11	0.09	0.08	0.07
Total	100.01	100.13	99.13	99.35	99.68	99.26	99.74	100.00	100.12
T (iv) site: Si	2.680	2.677	2.677	2.675	2.681	2.676	2.606	2.608	2.621
Al	1.328	1.330	1.333	1.332	1.324	1.331	1.399	1.395	1.384
Fe^{3+}									
T site total	4.009	4.007	4.010	4.007	4.005	4.008	4.005	4.003	4.005
Fe2+	0.001	0.001	0.000	0.001	0.001	0.002	0.002	0.001	0.004
Ca	0.315	0.316	0.316	0.316	0.318	0.317	0.385	0.387	0.372
Ba	bd	bd	bd	bd	bd	0.000	bd	0.001	0.001
Na	0.650	0.658	0.651	0.663	0.655	0.655	0.599	0.598	0.606
K	0.011	0.011	0.010	0.010	0.010	0.006	0.005	0.005	0.004
M-site total	0.976	0.985	0.977	0.988	0.983	0.979	0.990	0.991	0.983
Main feldspar components									
albite (mol%)	66.59	66.83	66.65	67.07	66.60	66.92	60.56	60.33	61.69
anorthite (mol%)	32.31	32.10	32.36	31.96	32.33	32.42	38.95	39.09	37.84
orthoclase (mol%)	1.10	1.07	0.99	0.97	1.06	0.65	0.50	0.46	0.39
celsian (mol%)	bd	bd	bd	bd	bd	0.01	bd	0.12	0.08

(APPENDIX B: CONTINUED)

Plagioclase

Sample #	SMC-14-031	SMC-14-031	SMC-14-031	SMC-14-031	SMC-14-031	SMC-14-031	SMC-14-031	SMC-14-031	SMC-14-031	SMC-14-031
Analysis pt. #	gplag1-04	gplag1-05	gplag1-06	plag2-07	plag2-08	plag2-09	plag3-10	plag3-11	plag3-12	plag4-13
SiO_2	59.83	59.75	59.30	60.60	60.80	60.22	61.03	61.10	61.05	60.44
Al_2O_3	25.79	25.62	25.82	25.05	25.02	25.05	25.14	25.19	25.24	25.76
FeO	0.04	0.06	0.06	0.02	0.02	0.08	0.02	0.00	bd	0.09
CaO	7.05	7.00	7.25	6.33	6.19	6.34	6.26	6.36	6.27	6.81
BaO	0.05	bd	bd	bd	bd	0.01	bd	bd	bd	0.05
Na_2O	7.57	7.49	7.35	7.84	8.03	7.81	7.96	7.80	7.98	7.65
K_2O	0.08	0.09	0.07	0.11	0.09	0.07	0.08	0.09	0.06	0.07
Total	100.41	100.01	99.85	99.95	100.15	99.58	100.49	100.54	100.60	100.87
T (iv) site: Si	2.655	2.660	2.647	2.694	2.697	2.688	2.698	2.698	2.695	2.667
Al	1.349	1.344	1.358	1.312	1.308	1.318	1.310	1.311	1.313	1.340
Fe^{3+}										
T site total	4.005	4.005	4.005	4.007	4.006	4.006	4.007	4.009	4.008	4.007
Fe2+	0.001	0.002	0.002	0.001	0.001	0.003	0.001	0.000	bd	0.003
Ca	0.335	0.334	0.347	0.302	0.294	0.303	0.296	0.301	0.297	0.322
Ba	0.001	bd	bd	bd	bd	0.000	bd	bd	bd	0.001
Na	0.651	0.647	0.636	0.676	0.691	0.676	0.682	0.668	0.683	0.655
K	0.005	0.005	0.004	0.006	0.005	0.004	0.004	0.005	0.004	0.004
M-site total	0.992	0.986	0.987	0.983	0.990	0.984	0.983	0.974	0.983	0.981
Main feldspar components										
albite (mol%)	65.65	65.58	64.46	68.73	69.77	68.72	69.39	68.57	69.47	66.70
anorthite (mol%)	33.79	33.87	35.14	30.66	29.72	30.83	30.16	30.90	30.16	32.81
orthoclase (mol%)	0.48	0.55	0.40	0.61	0.51	0.43	0.45	0.53	0.37	0.40
celsian (mol%)	0.08	bd	bd	bd	bd	0.02	bd	bd	bd	0.09

(APPENDIX B: CONTINUED)

Plagioclase

Sample #	SMC-14-031	SMC-14-031	SMC-14-031	SMC-14-031	SMC-14-031	SMC-14-031	SMC-14-031	SMC-14-031	SMC-14-031	SMC-14-031
Analysis pt. #	plag4-14	plag4-15	plag5-16	plag5-17	plag5-18	plag5-19	plag5-20	plag6-21	plag6-22	plag6-23
SiO_2	60.82	60.76	60.51	60.84	60.48	60.97	60.47	60.61	60.67	60.98
Al_2O_3	25.28	25.27	25.10	25.21	25.13	25.31	25.17	25.32	25.35	25.20
FeO	0.02	0.11	0.02	0.03	0.02	0.01	0.12	0.02	0.00	0.02
CaO	6.39	6.45	6.47	6.43	6.52	6.33	6.35	6.43	6.50	6.32
BaO	0.02	bd	bd	bd	bd	0.01	0.02	0.02		
Na_2O	7.81	7.78	7.76	7.91	7.74	7.87	7.74	7.87	7.83	8.09
K_2O	0.09	0.07	0.10	0.09	0.10	0.11	0.05	0.10	0.10	0.07
Total	100.44	100.44	99.96	100.51	99.99	100.61	99.91	100.37	100.45	100.68
T (iv) site: Si	2.691	2.689	2.690	2.691	2.689	2.692	2.689	2.685	2.685	2.692
Al	1.318	1.318	1.315	1.314	1.317	1.317	1.319	1.322	1.322	1.311
Fe^{3+}										
T site total	4.009	4.007	4.006	4.005	4.005	4.009	4.009	4.007	4.007	4.004
Fe2+	0.001	0.004	0.001	0.001	0.001	0.000	0.004	0.001	0.000	0.001
Ca	0.303	0.306	0.308	0.305	0.311	0.299	0.303	0.305	0.308	0.299
Ba	0.000	bd	bd	bd	bd	0.000	0.000	0.000		
Na	0.670	0.668	0.669	0.678	0.667	0.674	0.667	0.676	0.672	0.693
K	0.005	0.004	0.006	0.005	0.006	0.006	0.003	0.006	0.006	0.004
M-site total	0.978	0.977	0.983	0.988	0.983	0.979	0.973	0.987	0.986	0.995
Main feldspar components										
albite (mol%)	68.47	68.32	68.07	68.63	67.85	68.79	68.60	68.48	68.17	69.57
anorthite (mol%)	30.96	31.30	31.36	30.83	31.58	30.57	31.10	30.92	31.27	30.03
orthoclase (mol%)	0.53	0.38	0.57	0.54	0.57	0.63	0.27	0.56	0.56	0.40
celsian (mol%)	0.04	bd	bd	bd	bd	0.01	0.03	0.04		

APPENDIX C: EMPA ANALYSES-BIOTITE

Biotite								
Sample #	SMC-14-031	SMC-14-031	SMC-14-031	SMC-14-031	SMC-14-031	SMC-14-031	SM-14-031	SMC-14-031
Analysis pt. #	b1-01	b1-02	b1-03	b1-04	b1-05	b2-06	b2-07	b2-08
SiO_2	34.42	34.63	34.58	34.49	34.44	34.14	34.60	34.73
Al_2O_3	18.80	18.94	18.53	18.63	18.71	18.87	18.97	19.49
TiO_2	2.61	2.69	2.94	2.44	2.82	2.90	2.70	2.65
Cr_2O_3	0.04	0.03	0.06	0.06	0.05	0.01	0.05	0.05
FeO	21.46	20.88	21.82	21.71	21.11	20.41	20.80	20.29
MnO	0.05	0.05	0.09	0.08	0.08	0.05	0.10	0.06
MgO	7.67	7.60	7.67	8.04	7.71	7.53	7.66	7.55
CaO	bd	bd	0.01	bd	0.01	0.00	0.00	bd
BaO	0.17	0.25	0.18	0.17	0.17	0.18	0.26	0.28
Na_2O	0.22	0.21	0.21	0.21	0.23	0.23	0.23	0.23
K_2O	9.00	8.99	8.97	8.88	8.98	8.91	9.02	9.13
F	0.22	0.21	0.16	0.14	0.19	0.22	0.22	0.23
Cl	0.07	0.07	0.07	0.08	0.07	0.07	0.07	0.07
H2O (calculated)	3.74	3.74	3.78	3.78	3.75	3.70	3.74	3.75
T (iv) site: Si	5.352	5.377	5.351	5.351	5.355	5.352	5.367	5.366
Al	2.648	2.623	2.649	2.649	2.645	2.648	2.633	2.634
Al (total)	3.445	3.466	3.379	3.407	3.429	3.486	3.468	3.549
R (vi) site: Al	0.797	0.842	0.730	0.758	0.784	0.838	0.835	0.915
Ti	0.305	0.314	0.342	0.285	0.330	0.342	0.315	0.308
Cr^{3+}	0.005	0.004	0.007	0.007	0.006	0.002	0.006	0.007
Fe2+	2.790	2.711	2.824	2.817	2.745	2.676	2.698	2.622
Mn^{2+}	0.007	0.006	0.012	0.011	0.010	0.007	0.013	0.008
Mg	1.778	1.759	1.769	1.860	1.787	1.760	1.771	1.739
A (XII) site: Ca	bd	bd	0.002	bd	0.001	0.000	0.000	bd
Ba	0.011	0.015	0.011	0.010	0.010	0.011	0.016	0.017
Na	0.067	0.064	0.064	0.063	0.069	0.071	0.069	0.070
K	1.785	1.781	1.771	1.758	1.781	1.782		

(APPENDIX C: CONTINUED)

Biotite

Sample #	SMC-14-031	SMC-14-031	SMC-14-031	SMC-14-031	SMC-14-031	SMC-14-031	SMC-14-031	SMC-14-031
Analysis pt. #	b3-09	b3-10	b3-11	b4-12	b4-13	b4-14	b5-15	b5-16
SiO_2	34.79	34.52	34.61	34.36	34.05	34.19	34.06	34.36
Al_2O_3	18.81	18.66	18.53	18.85	18.79	18.86	18.67	18.57
TiO_2	2.85	2.87	2.95	2.95	2.94	2.85	2.87	2.78
Cr_2O_3	0.03	bd	0.05	0.01	0.07	0.06	0.06	0.06
FeO	20.79	21.20	20.99	20.46	20.49	21.15	20.85	20.83
MnO	0.08	0.08	0.06	0.05	0.06	0.08	0.08	0.10
MgO	7.72	7.66	7.80	7.65	7.51	7.55	7.70	7.81
CaO	0.01	0.00	0.01	0.00	bd	0.00	bd	bd
BaO	0.12	0.21	0.22	0.14	0.28	0.14	0.19	0.20
Na_2O	0.23	0.23	0.24	0.26	0.23	0.25	0.23	0.22
K_2O	9.12	9.02	9.02	8.92	8.92	8.91	8.95	9.09
F	0.23	0.17	0.22	0.18	0.20	0.27	0.27	0.25
Cl	0.07	0.07	0.07	0.07	0.07	0.07	0.07	0.07
H2O (calculated)	3.75	3.76	3.74	3.74	3.71	3.70	3.68	3.71
T (iv) site: Si	5.382	5.362	5.370	5.360	5.342	5.332	5.333	5.360
Al	2.618	2.638	2.630	2.640	2.658	2.668	2.667	2.640
Al (total)	3.430	3.416	3.389	3.465	3.474	3.466	3.445	3.414
R (vi) site: Al	0.812	0.778	0.759	0.825	0.816	0.798	0.778	0.774
Ti	0.332	0.335	0.344	0.346	0.347	0.334	0.338	0.326
Cr^{3+}	0.003		0.006	0.001	0.008	0.007	0.008	0.007
Fe2+	2.690	2.754	2.724	2.669	2.688	2.758	2.730	2.717
Mn^{2+}	0.011	0.011	0.008	0.006	0.008	0.011	0.011	0.013
Mg	1.780	1.774	1.804	1.779	1.756	1.755	1.797	1.816
A (XII) site: Ca	0.002	0.000	0.002	0.000	bd	0.000	bd	bd
Ba	0.007	0.013	0.014	0.008	0.017	0.008	0.011	0.012
Na	0.068	0.070	0.071	0.078	0.071	0.077	0.070	0.065
K	1.800	1.787	1.786	1.775	1.785	1.773	1.788	1.809

(APPENDIX C: CONTINUED)

Biotite

Sample #	SMC-14-031	SMC-14-031	SMC-14-034	SMC-14-034	SMC-14-034	SMC-14-034	SMC-14-034	SMC-14-034
Analysis pt. #	b5-17	b5-18	b1-01	b1-01	b2-03	b2-04	b2-05	b2-06
SiO_2	34.38	34.25	34.72	34.64	34.90	34.11	34.42	34.25
Al_2O_3	18.64	18.77	18.16	18.54	18.64	18.11	18.29	18.08
TiO_2	2.87	2.84	3.19	2.76	2.59	3.40	3.13	3.29
Cr_2O_3	0.05	0.06	0.02	0.04	0.07	0.04	0.06	0.04
FeO	20.81	20.83	21.15	21.16	20.79	21.10	20.92	21.27
MnO	0.05	0.08	0.09	0.06	0.07	0.09	0.08	0.10
MgO	7.61	7.54	7.66	7.92	7.90	7.57	7.71	7.56
CaO	bd	0.01	bd	bd	bd	bd	0.00	0.01
BaO	0.11	0.09	0.03	0.08	0.08	0.07	0.11	0.05
Na_2O	0.21	0.23	0.18	0.19	0.20	0.19	0.19	0.19
K_2O	9.03	9.03	9.04	8.96	9.02	9.01	9.04	8.89
F	0.22	0.24	0.12	0.21	0.29	0.19	0.17	0.24
Cl	0.07	0.07	0.20	0.17	0.17	0.18	0.17	0.18
H2O (calculated)	3.72	3.71	3.75	3.72	3.69	3.69	3.72	3.67
T (iv) site: Si	5.368	5.353	5.398	5.377	5.410	5.346	5.371	5.364
Al	2.632	2.647	2.602	2.623	2.590	2.654	2.629	2.636
Al (total)	3.430	3.457	3.328	3.392	3.405	3.345	3.363	3.337
R (vi) site: Al	0.799	0.810	0.726	0.769	0.815	0.692	0.734	0.701
Ti	0.337	0.334	0.373	0.322	0.302	0.401	0.367	0.387
Cr^{3+}	0.006	0.007	0.003	0.005	0.009	0.004	0.007	0.005
Fe2+	2.717	2.722	2.750	2.747	2.695	2.766	2.730	2.786
Mn^{2+}	0.007	0.010	0.012	0.008	0.010	0.012	0.011	0.013
Mg	1.771	1.757	1.775	1.833	1.825	1.769	1.793	1.765
A (XII) site: Ca	bd	0.001	bd	bd	bd	bd	0.000	0.001
Ba	0.007	0.006	0.002	0.005	0.005	0.004	0.007	0.003
Na	0.065	0.070	0.053	0.056	0.060	0.059	0.056	0.057
K	1.799	1.800	1.793	1.774	1.784	1.802	1.799	1.776

(APPENDIX C: CONTINUED)

Biotite

Sample #	SMC-14-034	SMC-14-034	SMC-14-034	SMC-13-130	SMC-13-130	SMC-13-130	SMC-13-130	SMC-13-130
Analysis pt. #	b2-07	b2-08	b2-09	gb1-01	b2-02	b2-03	b2-04	b2-05
SiO_2	34.90	35.08	34.82	34.01	34.17	34.62	33.90	34.12
Al_2O_3	18.25	18.45	18.48	19.33	18.73	18.68	18.22	18.25
TiO_2	3.01	2.62	2.92	2.04	2.07	2.15	2.09	2.47
Cr_2O_3	0.05	0.05	0.05	0.00	0.01	0.04	0.02	0.05
FeO	21.21	20.88	20.99	23.04	22.89	22.55	22.89	22.65
MnO	0.11	0.10	0.07	0.13	0.10	0.09	0.12	0.12
MgO	7.77	8.04	7.71	6.28	7.01	7.22	7.01	7.01
CaO	0.00	0.00	bd	0.00	bd	bd	0.01	0.00
BaO	bd	0.04	0.06	0.07	0.18	0.17	0.20	0.12
Na_2O	0.18	0.19	0.17	0.19	0.22	0.21	0.15	0.25
K_2O	9.04	8.92	9.08	9.18	8.73	8.81	8.94	8.86
F	0.22	0.30	0.20	0.36	0.40	0.40	0.52	0.55
Cl	0.17	0.18	0.17	0.18	0.18	0.15	0.17	0.16
H2O (calculated)	3.72	3.69	3.73	3.60	3.59	3.62	3.50	3.50
T (iv) site: Si	5.407	5.427	5.401	5.342	5.366	5.397	5.373	5.372
Al	2.593	2.573	2.599	2.658	2.634	2.603	2.627	2.628
Al (total)	3.333	3.364	3.378	3.578	3.466	3.432	3.403	3.387
R (vi) site: Al	0.740	0.792	0.779	0.920	0.832	0.828	0.776	0.759
Ti	0.351	0.305	0.341	0.241	0.244	0.252	0.249	0.292
Cr^{3+}	0.006	0.006	0.006	0.001	0.001	0.005	0.003	0.007
Fe2+	2.748	2.702	2.723	3.026	3.006	2.940	3.034	2.983
Mn^{2+}	0.014	0.013	0.009	0.017	0.014	0.012	0.016	0.016
Mg	1.795	1.854	1.783	1.470	1.641	1.678	1.656	1.645
A (XII) site: Ca	0.000	0.001	bd	0.000	bd	bd	0.002	0.000
Ba	bd	0.003	0.004	0.004	0.011	0.011	0.012	0.008
Na	0.053	0.056	0.051	0.057	0.066	0.062	0.045	0.077
K	1.787	1.761	1.797	1.839	1.749	1.752	1.808	1.780

(APPENDIX C: CONTINUED)

Biotite

Sample #	SMC-13-130	SMC-13-130	SMC-13-130	SMC-13-130	SMC-13-130	SMC-13-130	SMC-13-130	SMC-13-130
Analysis pt. #	b2-06	b2-07	b2-08	b3-09	b3-10	b3-11	gb3-12	gb2-13
SiO_2	34.46	33.99	34.12	34.55	34.40	34.24	34.11	34.25
Al_2O_3	18.63	18.69	18.54	18.75	18.36	18.53	18.15	18.15
TiO_2	2.07	1.76	2.05	2.07	2.70	2.32	2.78	2.95
Cr_2O_3	0.04	0.00	0.05	0.05	0.03	0.07	0.04	0.03
FeO	22.45	22.19	22.54	22.12	22.37	22.58	21.87	21.59
MnO	0.13	0.12	0.12	0.09	0.11	0.15	0.18	0.14
MgO	7.12	7.28	7.08	7.41	7.02	7.16	7.44	7.43
CaO	0.02	bd	0.00	bd	bd	0.00	bd	0.00
BaO	0.02	0.09	0.09	0.09	0.10	0.13	0.16	0.13
Na_2O	0.20	0.21	0.18	0.21	0.17	0.14	0.18	0.17
K_2O	8.93	9.01	9.17	8.87	9.12	8.91	9.03	9.05
F	0.46	0.42	0.29	0.33	0.36	0.40	0.43	0.30
Cl	0.19	0.17	0.17	0.17	0.19	0.17	0.13	0.14
H2O (calculated)	3.56	3.55	3.63	3.64	3.61	3.60	3.58	3.64
T (iv) site: Si	5.399	5.373	5.372	5.393	5.381	5.366	5.358	5.370
Al	2.601	2.627	2.628	2.607	2.619	2.634	2.642	2.630
Al (total)	3.440	3.482	3.441	3.449	3.385	3.423	3.360	3.354
R (vi) site: Al	0.838	0.855	0.813	0.843	0.766	0.789	0.717	0.725
Ti	0.244	0.209	0.243	0.243	0.318	0.273	0.328	0.348
Cr^{3+}	0.005	0.000	0.006	0.006	0.003	0.009	0.005	0.004
Fe2+	2.941	2.934	2.968	2.888	2.926	2.960	2.873	2.831
Mn^{2+}	0.018	0.017	0.016	0.012	0.015	0.020	0.024	0.019
Mg	1.663	1.716	1.662	1.724	1.637	1.673	1.742	1.737
A (XII) site: Ca	0.003	bd	0.001	bd	bd	0.000	bd	0.000
Ba	0.001	0.006	0.006	0.005	0.006	0.008	0.010	0.008
Na	0.060	0.063	0.055	0.065	0.051	0.042	0.055	0.053
K	1.785	1.817	1.842	1.766	1.820	1.782	1.809	1.810

(APPENDIX C: CONTINUED)

Biotite

Sample #	SMC-13-130	SMC-13-130	SMC-13-130	SMC-13-130	SMC-13-130	SMC-13-130	SMC-13-130	SMC-13-128
Analysis pt. #	b4-14	b4-15	b4-16	b4-17	b5-18	b5-19	b5-20	gbl-01
SiO_2	34.45	34.22	34.26	34.46	34.17	34.01	34.25	33.64
Al_2O_3	18.52	18.41	18.38	18.55	18.11	18.35	18.59	17.25
TiO_2	2.07	2.12	1.76	1.85	2.67	2.18	2.19	2.53
Cr_2O_3	0.01	0.05	0.04	0.02	0.07	0.06	0.02	0.07
FeO	22.32	22.44	23.12	22.61	22.83	22.84	22.32	24.19
MnO	0.14	0.13	0.10	0.14	0.12	0.14	0.10	0.13
MgO	7.35	7.46	7.42	7.48	6.74	7.03	7.12	6.11
CaO	bd	bd	0.02	bd	bd	bd	bd	bd
BaO	0.15	0.07	0.12	0.14	0.10	0.07	0.58	0.19
Na_2O	0.22	0.25	0.23	0.20	0.19	0.18	0.23	0.12
K_2O	8.95	8.86	8.83	8.96	9.07	9.05	8.80	9.04
F	0.50	0.49	0.58	0.49	0.52	0.32	0.39	0.08
Cl	0.18	0.18	0.21	0.18	0.15	0.15	0.17	0.20
H2O (calculated)	3.55	3.54	3.49	3.56	3.52	3.61	3.59	3.65
T (iv) site: Si	5.395	5.371	5.379	5.390	5.381	5.364	5.378	5.399
Al	2.605	2.629	2.621	2.610	2.619	2.636	2.622	2.601
Al (total)	3.418	3.406	3.401	3.419	3.361	3.411	3.440	3.263
R (vi) site: Al	0.813	0.777	0.780	0.809	0.742	0.776	0.818	0.662
Ti	0.244	0.250	0.208	0.218	0.316	0.259	0.259	0.305
Cr^{3+}	0.002	0.006	0.005	0.002	0.009	0.007	0.002	0.009
Fe2+	2.923	2.946	3.036	2.957	3.007	3.013	2.931	3.247
Mn^{2+}	0.018	0.017	0.013	0.019	0.016	0.018	0.013	0.018
Mg	1.716	1.746	1.737	1.744	1.582	1.653	1.667	1.462
A (XII) site: Ca	bd	bd	0.004	bd	bd	bd	bd	bd
Ba	0.009	0.004	0.008	0.008	0.006	0.004	0.035	0.012
Na	0.066	0.077	0.071	0.061	0.058	0.055	0.071	0.037
K	1.788	1.774	1.769	1.788	1.822	1.821	1.763	1.851

(APPENDIX C: CONTINUED)

Biotite

Sample #	SMC-13-128	SMC-13-128	SMC-13-128	SMC-13-128	SMC-13-128	SMC-13-128	SMC-13-128	SMC-13-128
Analysis pt. #	gb2-02	gb2-03	gb2-04	b3-05	b3-06	b3-07	b3-08	b3-09
SiO_2	33.77	33.64	33.67	34.35	34.20	34.25	34.26	34.28
Al_2O_3	17.81	17.52	18.33	18.56	18.63	18.76	18.99	18.76
TiO_2	2.34	2.83	1.69	2.55	2.78	2.00	1.94	2.08
Cr_2O_3	0.04	0.03	0.04	0.03	0.01	0.03	0.04	0.04
FeO	23.47	23.85	24.70	22.23	22.10	21.82	22.15	22.04
MnO	0.12	0.09	0.08	0.10	0.10	0.09	0.10	0.11
MgO	6.42	6.06	5.99	7.27	7.20	7.48	7.27	7.46
CaO	0.01	0.01	0.01	bd	0.01	bd	0.01	0.00
BaO	0.14	0.25	0.23	0.10	0.19	0.16	0.14	0.22
Na_2O	0.11	0.15	0.15	0.26	0.24	0.21	0.16	0.22
K_2O	8.95	8.95	8.91	8.85	8.81	8.98	9.19	8.88
F	0.24	0.22	0.15	0.29	0.13	0.17	0.12	0.35
Cl	0.23	0.22	0.20	0.14	0.14	0.14	0.15	0.14
H2O (calculated)	3.59	3.59	3.64	3.67	3.74	3.70	3.74	3.63
T (iv) site: Si	5.392	5.380	5.371	5.366	5.345	5.375	5.361	5.367
Al	2.608	2.620	2.629	2.634	2.655	2.625	2.639	2.633
Al (total)	3.352	3.302	3.446	3.417	3.432	3.470	3.502	3.462
R (vi) site: Al	0.744	0.682	0.818	0.783	0.777	0.845	0.864	0.829
Ti	0.281	0.340	0.203	0.300	0.327	0.236	0.228	0.245
Cr^{3+}	0.005	0.004	0.004	0.004	0.001	0.004	0.005	0.005
Fe2+	3.134	3.190	3.295	2.904	2.889	2.864	2.899	2.886
Mn^{2+}	0.017	0.012	0.011	0.013	0.013	0.012	0.013	0.015
Mg	1.528	1.445	1.425	1.693	1.678	1.750	1.696	1.741
A (XII) site: Ca	0.002	0.001	0.001	bd	0.001	bd	0.001	0.001
Ba	0.009	0.016	0.014	0.006	0.012	0.010	0.009	0.014
Na	0.034	0.047	0.046	0.078	0.072	0.065	0.048	0.065
K	1.823	1.826	1.813	1.764	1.757	1.798	1.835	1.774

(APPENDIX C: CONTINUED)

Biotite

Sample #	SMC-13-128	SMC-13-128	SMC-13-128	SMC-13-128	SMC-13-128	SMC-13-128	SMC-13-128	SMC-13-128
Analysis pt. #	b3-10	b3-11	b3-12	b3-13	b3-14	b4-15	b4-16	b4-17
SiO_2	34.20	34.14	34.34	34.30	34.20	34.50	34.69	34.11
Al_2O_3	18.90	18.90	18.59	18.65	18.56	18.17	18.32	18.51
TiO_2	1.84	1.97	2.21	2.19	2.19	2.70	2.69	2.44
Cr_2O_3	0.02	0.04	0.04	0.04	0.05	0.03	0.03	0.07
FeO	21.99	21.68	22.30	22.17	21.94	22.40	22.59	22.50
MnO	0.11	0.09	0.10	0.13	0.08	0.13	0.11	0.10
MgO	7.61	7.68	7.49	7.48	7.61	7.16	7.12	7.21
CaO	bd	bd	bd	0.00	bd	bd	bd	0.01
BaO	0.17	0.23	0.17	0.08	0.22	0.13	0.14	0.20
Na_2O	0.19	0.19	0.24	0.24	0.22	0.20	0.21	0.22
K_2O	9.04	9.01	8.92	8.95	8.97	8.98	9.03	8.88
F	0.27	0.26	0.10	0.18	0.31	0.18	0.17	0.30
Cl	0.17	0.15	0.15	0.16	0.14	0.14	0.14	0.14
H2O (calculated)	3.66	3.66	3.75	3.71	3.64	3.71	3.74	3.65
T (iv) site: Si	5.357	5.351	5.365	5.364	5.362	5.394	5.395	5.349
Al	2.643	2.649	2.635	2.636	2.638	2.606	2.605	2.651
Al (total)	3.489	3.491	3.423	3.437	3.429	3.348	3.358	3.421
R (vi) site: Al	0.846	0.842	0.788	0.801	0.791	0.742	0.753	0.769
Ti	0.217	0.232	0.260	0.258	0.258	0.317	0.315	0.288
Cr^{3+}	0.003	0.005	0.005	0.005	0.006	0.003	0.004	0.009
Fe2+	2.881	2.842	2.914	2.899	2.876	2.929	2.938	2.950
Mn^{2+}	0.015	0.012	0.014	0.018	0.010	0.017	0.015	0.013
Mg	1.777	1.794	1.744	1.744	1.778	1.669	1.651	1.685
A (XII) site: Ca	bd	bd	bd	0.000	bd	bd	bd	0.001
Ba	0.011	0.014	0.010	0.005	0.013	0.008	0.008	0.012
Na	0.057	0.057	0.074	0.073	0.066	0.061	0.063	0.067
K	1.806	1.801	1.778	1.785	1.794	1.791	1.791	1.776

(APPENDIX C: CONTINUED)

Biotite

Sample #	SMC-13-128	SMC-13-128	SMC-13-128	SMC-13-128	SMC-13-128	SMC-13-128	SMC-13-128	SMC-13-128
Analysis pt. #	b4-18	b4-19	b4-20	b4-21	b4-22	gb3-23	b5-24	b5-25
SiO_2	34.64	34.11	34.50	34.41	34.60	34.23	34.22	34.18
Al_2O_3	18.15	18.25	18.56	18.70	18.70	19.02	17.74	17.66
TiO_2	2.72	2.69	2.35	2.21	2.00	1.62	2.46	2.78
Cr_2O_3	0.06	0.01	0.06	0.05	0.04	0.04	0.01	0.06
FeO	22.68	22.95	22.30	21.99	22.07	23.23	22.87	22.63
MnO	0.07	0.11	0.13	0.13	0.09	0.07	0.10	0.09
MgO	6.94	6.91	7.26	7.15	7.34	6.07	7.27	6.83
CaO	bd	bd	bd	0.01	0.00	0.02	0.01	0.01
BaO	0.05	0.26	0.23	0.21	0.28	0.25	0.23	0.30
Na_2O	0.24	0.19	0.18	0.16	0.16	0.13	0.16	0.21
K_2O	8.94	9.09	9.05	9.12	9.07	8.92	9.08	8.91
F	0.34	0.26	0.32	0.25	0.36	0.11	0.27	0.21
Cl	0.15	0.15	0.15	0.15	0.14	0.11	0.15	0.14
H2O (calculated)	3.64	3.66	3.66	3.67	3.64	3.71	3.64	3.66
T (iv) site: Si	5.410	5.352	5.382	5.389	5.405	5.417	5.393	5.409
Al	2.590	2.648	2.618	2.611	2.595	2.583	2.607	2.591
Al (total)	3.341	3.375	3.412	3.452	3.443	3.547	3.295	3.294
R (vi) site: Al	0.752	0.727	0.794	0.841	0.847	0.964	0.687	0.703
Ti	0.319	0.317	0.276	0.260	0.235	0.192	0.292	0.331
Cr^{3+}	0.007	0.001	0.007	0.006	0.005	0.005	0.001	0.007
Fe2+	2.962	3.012	2.909	2.880	2.883	3.074	3.014	2.995
Mn^{2+}	0.009	0.015	0.017	0.017	0.012	0.009	0.013	0.012
Mg	1.616	1.616	1.688	1.669	1.709	1.432	1.708	1.611
A (XII) site: Ca	bd	bd	bd	0.001	0.000	0.003	0.001	0.001
Ba	0.003	0.016	0.014	0.013	0.017	0.015	0.014	0.019
Na	0.074	0.057	0.055	0.048	0.048	0.041	0.049	0.064
K	1.781	1.820	1.801	1.822	1.807	1.801	1.825	1.799

(APPENDIX C: CONTINUED)

Biotite

Sample #	SMC-13-128	SMC-13-128	SMC-13-128	SMC-13-128	SMC-13-128	SMC-13-128	SMC-13-119	SMC-13-119
Analysis pt. #	b5-26	b5-27	b5-28	b5-29	b5-30	b5-31	grt in-b1	grt in-b2
SiO_2	34.29	34.59	34.63	34.28	34.22	34.08	35.16	35.00
Al_2O_3	17.72	18.17	18.51	18.92	18.44	18.55	19.63	18.96
TiO_2	2.90	2.94	2.55	1.83	2.61	2.63	2.04	2.57
Cr_2O_3	0.05	0.03	0.04	0.05	0.07	0.02	0.03	0.02
FeO	23.36	22.49	21.96	21.84	22.35	22.19	19.29	20.41
MnO	0.14	0.06	0.11	0.11	0.09	0.11	0.06	0.08
MgO	6.93	7.09	7.36	7.73	7.45	6.82	8.72	8.27
CaO	bd	bd	bd	0.00	0.00	bd	0.01	0.01
BaO	0.15	0.19	0.19	0.14	0.23	0.29	0.12	0.23
Na_2O	0.19	0.30	0.18	0.21	0.25	0.17	0.23	0.20
K_2O	8.93	8.86	9.09	8.96	8.94	9.13	9.11	9.07
F	0.15	0.23	0.31	0.13	0.09	0.24	0.15	0.34
Cl	0.14	0.14	0.15	0.15	0.14	0.16	0.12	0.12
H2O (calculated)	3.72	3.70	3.67	3.73	3.77	3.66	3.81	3.71
T (iv) site: Si	5.378	5.389	5.390	5.361	5.341	5.361	5.394	5.387
Al	2.622	2.611	2.610	2.639	2.659	2.639	2.606	2.613
Al (total)	3.276	3.336	3.396	3.487	3.392	3.439	3.550	3.439
R (vi) site: Al	0.654	0.726	0.786	0.848	0.733	0.800	0.944	0.826
Ti	0.342	0.344	0.298	0.215	0.306	0.311	0.235	0.297
Cr^{3+}	0.006	0.004	0.005	0.006	0.009	0.003	0.003	0.002
Fe2+	3.064	2.930	2.859	2.856	2.917	2.919	2.475	2.627
Mn^{2+}	0.019	0.007	0.014	0.015	0.012	0.014	0.008	0.010
Mg	1.620	1.647	1.708	1.802	1.733	1.599	1.994	1.897
A (XII) site: Ca	bd	bd	bd	0.001	0.000	bd	0.001	0.001
Ba	0.009	0.012	0.011	0.009	0.014	0.018	0.007	0.014
Na	0.059	0.091	0.054	0.063	0.076	0.053	0.067	0.060
K	1.787	1.761	1.805	1.788	1.780	1.832	1.783	1.781

(APPENDIX C: CONTINUED)

Biotite

Sample #	SMC-13-119	SMC-13-119	SMC-13-119	SMC-13-119	SMC-13-119	SMC-13-119	SMC-13-119
Analysis pt. #	grt in-b3	grt in-b4	b5	b6	b7	b8	b9
SiO_2	34.65	34.22	34.67	34.74	34.36	34.14	34.54
Al_2O_3	19.27	18.71	18.79	18.68	18.83	18.75	18.81
TiO_2	2.62	2.69	2.63	2.68	2.52	2.56	2.98
Cr_2O_3	bd	0.03	0.04	0.05	0.04	0.05	0.07
FeO	20.16	20.55	20.74	20.54	21.07	21.18	20.94
MnO	0.10	0.06	0.10	0.09	0.10	0.12	0.14
MgO	8.22	8.17	7.68	7.72	7.74	7.64	7.91
CaO	bd	0.00	0.00	bd	bd	0.00	bd
BaO	0.11	0.25	0.18	bd	0.28	0.17	bd
Na_2O	0.18	0.18	0.18	0.14	0.21	0.22	0.14
K_2O	8.90	9.04	9.21	9.29	9.26	9.14	9.26
F	0.27	0.23	0.11	0.21	0.29	0.24	0.16
Cl	0.13	0.13	0.11	0.12	0.13	0.14	0.12
H2O (calculated)	3.72	3.70	3.78	3.73	3.68	3.69	3.77
T (iv) site: Si	5.353	5.337	5.388	5.404	5.349	5.340	5.338
Al	2.647	2.663	2.612	2.596	2.651	2.660	2.662
Al (total)	3.509	3.439	3.441	3.425	3.455	3.457	3.426
R (vi) site: Al	0.862	0.776	0.829	0.829	0.805	0.797	0.763
Ti	0.304	0.316	0.307	0.314	0.295	0.301	0.346
Cr^{3+}		0.004	0.005	0.007	0.004	0.006	0.008
Fe2+	2.605	2.680	2.695	2.672	2.743	2.771	2.706
Mn^{2+}	0.013	0.008	0.014	0.012	0.013	0.015	0.019
Mg	1.893	1.900	1.779	1.790	1.796	1.782	1.822
A (XII) site: Ca	bd	0.000	0.000	bd	bd	0.000	bd
Ba	0.006	0.015	0.011	bd	0.017	0.010	bd
Na	0.054	0.053	0.055	0.043	0.064	0.066	0.043
K	1.754	1.799	1.826	1.844	1.839	1.824	1.826

(APPENDIX C: CONTINUED)

Biotite

Sample #	SMC-13-119	SMC-13-119	SMC-13-119	SMC-13-119	SMC-13-119	SMC-13-119	SMC-13-118	SMC-13-118
Analysis pt. #	b10	b11	b12	b13	b14	b15	b1-01	b1-02
SiO_2	34.41	34.55	34.28	34.78	34.69	34.59	34.19	34.34
Al_2O_3	18.73	19.00	18.53	18.76	18.74	18.70	18.20	18.36
TiO_2	2.99	2.86	2.83	2.88	3.02	2.78	2.69	2.80
Cr_2O_3	0.05	0.03	0.03	0.04	0.01	0.06	0.03	0.06
FeO	20.84	20.18	20.51	21.15	20.94	20.83	20.72	20.56
MnO	0.12	0.13	0.13	0.10	0.12	0.08	0.17	0.18
MgO	7.80	7.84	7.78	7.99	7.99	7.98	8.33	8.19
CaO	bd	0.01	bd	0.03	0.03	bd	0.01	0.01
BaO	0.22	0.09	0.11	0.15	0.18	0.21	0.23	0.35
Na_2O	0.17	0.20	0.18	0.27	0.24	0.19	0.16	0.18
K_2O	9.25	9.22	9.16	8.98	8.90	9.12	9.07	8.98
F	0.23	0.11	0.16	0.21	0.27	0.28	0.32	0.21
Cl	0.13	0.14	0.13	0.13	0.13	0.12	0.12	0.12
H2O (calculated)	3.72	3.78	3.72	3.76	3.73	3.71	3.65	3.71
T (iv) site: Si	5.339	5.360	5.367	5.356	5.352	5.361	5.351	5.357
Al	2.661	2.640	2.633	2.644	2.648	2.639	2.649	2.643
Al (total)	3.425	3.474	3.419	3.405	3.407	3.416	3.357	3.376
R (vi) site: Al	0.764	0.833	0.786	0.760	0.759	0.776	0.708	0.733
Ti	0.349	0.334	0.333	0.334	0.350	0.324	0.317	0.328
Cr^{3+}	0.007	0.003	0.003	0.005	0.001	0.008	0.004	0.007
Fe2+	2.704	2.618	2.685	2.724	2.702	2.700	2.712	2.682
Mn^{2+}	0.015	0.017	0.017	0.013	0.015	0.010	0.022	0.023
Mg	1.804	1.813	1.816	1.834	1.838	1.844	1.944	1.905
A (XII) site: Ca	bd	0.002	bd	0.005	0.005	bd	0.002	0.002
Ba	0.013	0.005	0.006	0.009	0.011	0.013	0.014	0.021
Na	0.051	0.060	0.054	0.081	0.073	0.056	0.048	0.054
K	1.831	1.825	1.830	1.764	1.752	1.803	1.811	1.787

(APPENDIX C: CONTINUED)

Biotite

Sample #	SMC-13-118	SMC-13-118	SMC-13-118	SMC-13-118	SMC-13-118	SMC-13-118	SMC-13-118
Analysis pt. #	b1-03	b1-04	b1-05	b1-06	gb1-07	gb2-08	gb2-09
SiO_2	34.11	33.93	34.04	34.30	34.35	34.44	34.20
Al_2O_3	18.58	18.46	18.29	18.49	19.21	18.77	18.42
TiO_2	3.36	3.28	2.59	2.67	2.18	2.73	2.76
Cr_2O_3	0.07	0.05	0.03	0.07	0.03	0.05	0.07
FeO	20.81	20.95	20.45	20.75	20.60	20.74	20.53
MnO	0.16	0.13	0.16	0.13	0.10	0.11	0.15
MgO	7.72	7.82	8.32	8.32	8.29	8.12	7.93
CaO	0.01	0.00	0.01	0.01	0.00	0.01	0.00
BaO	0.08	0.23	0.19	0.05	0.22	0.31	0.12
Na_2O	0.19	0.20	0.17	0.20	0.13	0.24	0.19
K_2O	9.17	9.01	9.22	9.12	8.99	8.90	9.22
F	0.12	0.25	0.38	0.23	0.25	0.24	0.20
Cl	0.12	0.12	0.12	0.11	0.11	0.11	0.12
H2O (calculated)	3.76	3.69	3.61	3.71	3.71	3.72	3.70
T (iv) site: Si	5.310	5.301	5.345	5.340	5.337	5.343	5.357
Al	2.690	2.699	2.655	2.660	2.663	2.657	2.643
Al (total)	3.409	3.399	3.385	3.393	3.518	3.432	3.401
R (vi) site: Al	0.719	0.701	0.729	0.733	0.854	0.776	0.758
Ti	0.393	0.385	0.306	0.313	0.255	0.319	0.325
Cr^{3+}	0.008	0.006	0.004	0.009	0.004	0.006	0.009
Fe2+	2.709	2.737	2.685	2.702	2.677	2.691	2.690
Mn^{2+}	0.021	0.017	0.021	0.017	0.013	0.014	0.020
Mg	1.792	1.821	1.947	1.931	1.920	1.878	1.852
A (XII) site: Ca	0.001	0.001	0.002	0.002	0.000	0.001	0.001
Ba	0.005	0.014	0.012	0.003	0.014	0.019	0.008
Na	0.058	0.061	0.051	0.061	0.040	0.071	0.057
K	1.821	1.796	1.847	1.812	1.782	1.762	1.843

(APPENDIX C: CONTINUED)

Biotite

Sample #	SMC-13-118	SMC-13-118	SMC-13-118	SMC-13-118	SMC-13-118	SMC-13-118	SMC-13-118
Analysis pt. #	gb2-10	b2-11	b2-12	b2-13	b2-14	b3-15	b3-16
SiO_2	34.28	34.73	35.01	34.79	34.29	34.67	34.21
Al_2O_3	18.38	18.46	18.43	18.26	18.29	18.24	18.36
TiO_2	2.65	2.89	3.12	2.88	2.82	2.74	2.77
Cr_2O_3	0.06	0.06	0.05	0.01	0.03	0.06	0.08
FeO	20.80	21.00	20.37	20.39	20.64	20.89	20.93
MnO	0.12	0.13	0.15	0.13	0.15	0.14	0.17
MgO	8.25	8.05	8.15	8.11	8.10	7.99	8.08
CaO	0.01	0.01	0.02	0.01	0.01	0.01	0.00
BaO	0.15	0.27	0.26	0.26	0.29	0.06	0.20
Na_2O	0.17	0.24	0.26	0.23	0.20	0.13	0.18
K_2O	9.14	8.83	9.05	9.00	9.01	9.27	9.06
F	0.27	0.18	0.17	0.30	0.30	0.16	0.29
Cl	0.12	0.12	0.12	0.13	0.11	0.12	0.13
H2O (calculated)	3.68	3.76	3.78	3.69	3.67	3.75	3.67
T (iv) site: Si	5.350	5.374	5.393	5.408	5.361	5.396	5.343
Al	2.650	2.626	2.607	2.592	2.639	2.604	2.657
Al (total)	3.381	3.367	3.346	3.345	3.370	3.346	3.379
R (vi) site: Al	0.730	0.741	0.739	0.753	0.731	0.743	0.722
Ti	0.311	0.336	0.361	0.337	0.332	0.321	0.325
Cr^{3+}	0.007	0.008	0.006	0.001	0.004	0.007	0.010
Fe2+	2.715	2.718	2.624	2.651	2.699	2.719	2.734
Mn^{2+}	0.015	0.017	0.020	0.017	0.020	0.018	0.022
Mg	1.919	1.857	1.872	1.879	1.888	1.854	1.881
A (XII) site: Ca	0.002	0.002	0.002	0.002	0.001	0.001	0.001
Ba	0.009	0.016	0.016	0.016	0.018	0.003	0.012
Na	0.053	0.071	0.077	0.068	0.061	0.040	0.055
K	1.820	1.743	1.779	1.785	1.797	1.841	1.805

(APPENDIX C: CONTINUED)

Biotite

Sample #	SMC-13-118	SMC-13-118	SMC-13-118	SMC-13-118	SMC-13-118	SMC-13-118	SMC-13-118
Analysis pt. #	b3-17	b3-18	b4-19	b4-20	b4-21	b4-22	b4-23
SiO_2	34.22	34.54	34.60	34.11	34.41	34.29	34.21
Al_2O_3	17.98	18.48	18.30	18.26	18.28	18.36	18.18
TiO_2	2.81	2.81	2.81	2.73	2.75	2.78	2.61
Cr_2O_3	0.05	0.09	0.06	0.07	0.02	0.06	0.05
FeO	21.07	20.72	20.92	21.05	20.22	20.38	20.12
MnO	0.17	0.15	0.13	0.12	0.11	0.14	0.10
MgO	7.79	8.07	7.88	8.02	8.51	8.53	8.44
CaO	bd	bd	0.00	bd	0.01	0.01	0.01
BaO	0.30	0.19	0.06	0.34	0.20	0.06	0.17
Na_2O	0.16	0.20	0.22	0.18	0.20	0.27	0.22
K_2O	9.19	9.16	9.12	9.10	9.11	8.93	8.88
F	0.27	0.28	0.20	0.21	0.18	0.23	0.18
Cl	0.13	0.12	0.12	0.11	0.11	0.12	0.12
H2O (calculated)	3.65	3.70	3.73	3.70	3.73	3.71	3.70
T (iv) site: Si	5.377	5.364	5.389	5.342	5.366	5.344	5.376
Al	2.623	2.636	2.611	2.658	2.634	2.656	2.624
Al (total)	3.329	3.382	3.359	3.371	3.360	3.372	3.367
R (vi) site: Al	0.706	0.746	0.748	0.713	0.726	0.716	0.744
Ti	0.332	0.328	0.329	0.322	0.322	0.326	0.308
Cr^{3+}	0.006	0.010	0.007	0.009	0.002	0.008	0.006
Fe2+	2.769	2.691	2.725	2.757	2.637	2.656	2.644
Mn^{2+}	0.023	0.019	0.017	0.016	0.015	0.018	0.014
Mg	1.825	1.868	1.830	1.873	1.978	1.982	1.977
A (XII) site: Ca	bd	bd	0.001	bd	0.002	0.001	0.002
Ba	0.019	0.012	0.004	0.021	0.012	0.004	0.010
Na	0.048	0.061	0.067	0.056	0.059	0.083	0.066
K	1.842	1.815	1.812	1.818	1.812	1.775	1.780

(APPENDIX C: CONTINUED)

Biotite

Sample #	SMC-14-035	SMC-14-035	SMC-14-035	SMC-14-035	SMC-14-035	SMC-14-035	SMC-14-035
Analysis pt. #	gb1	gb2	b1-03	b1-04	b1-05	b1-06	b1-07
SiO_2	34.19	35.17	34.60	34.99	34.82	34.45	35.07
Al_2O_3	19.43	18.93	18.98	18.98	18.97	18.87	18.81
TiO_2	1.21	1.45	1.86	1.69	1.84	1.95	1.83
Cr_2O_3	0.04	0.06	0.06	0.03	0.06	0.02	0.05
FeO	22.38	21.60	21.44	20.91	21.48	21.75	21.45
MnO	0.17	0.13	0.17	0.20	0.14	0.19	0.17
MgO	7.16	7.77	7.48	7.69	7.64	7.53	7.61
CaO	bd	bd	0.00	0.00	bd	0.00	bd
BaO	0.08	0.03	0.04	bd	0.03	0.09	bd
Na_2O	0.25	0.28	0.31	0.38	0.34	0.31	0.33
K_2O	9.16	8.77	8.92	8.97	8.92	8.93	8.99
F	0.50	0.78	0.70	0.77	0.79	0.60	0.72
Cl	0.11	0.10	0.08	0.10	0.09	0.10	0.09
H2O (calculated)	3.56	3.47	3.49	3.46	3.46	3.53	3.50
T (iv) site: Si	5.364	5.461	5.404	5.447	5.413	5.382	5.446
Al	2.636	2.539	2.596	2.553	2.587	2.618	2.554
Al (total)	3.592	3.464	3.494	3.482	3.476	3.474	3.442
R (vi) site: Al	0.956	0.925	0.898	0.929	0.889	0.856	0.888
Ti	0.143	0.169	0.218	0.198	0.215	0.229	0.214
Cr^{3+}	0.005	0.008	0.007	0.004	0.007	0.002	0.006
Fe2+	2.936	2.805	2.801	2.722	2.793	2.842	2.786
Mn^{2+}	0.022	0.017	0.023	0.026	0.019	0.025	0.022
Mg	1.674	1.798	1.742	1.785	1.771	1.754	1.762
A (XII) site: Ca	bd	bd	0.000	0.001	bd	0.001	bd
Ba	0.005	0.002	0.002	bd	0.002	0.006	bd
Na	0.075	0.084	0.094	0.116	0.103	0.095	0.098
K	1.833	1.737	1.777	1.781	1.769	1.780	1.781

(APPENDIX C: CONTINUED)

Biotite

Sample #	SMC-14-035	SMC-14-035	SMC-14-035	SMC-14-035	SMC-14-035	SMC-14-035	SMC-14-035
Analysis pt. #	b2-08	b2-09	b2-10	b2-11	b2-12	b3-13	b4-14
SiO_2	34.46	34.94	35.08	34.71	34.44	34.65	34.81
Al_2O_3	19.08	19.34	18.99	19.07	19.43	19.26	19.13
TiO_2	1.71	1.58	1.52	1.58	1.58	1.61	1.76
Cr_2O_3	0.04	0.04	0.03	0.04	0.03	0.02	0.06
FeO	20.85	21.50	20.79	21.32	20.82	21.53	21.35
MnO	0.19	0.18	0.19	0.20	0.16	0.16	0.14
MgO	7.59	7.76	7.86	7.74	7.64	7.62	7.78
CaO	0.01	0.01	bd	bd	bd	bd	0.01
BaO	0.08	bd	0.04	0.02	0.15	0.07	0.15
Na_2O	0.31	0.29	0.28	0.32	0.26	0.33	0.32
K_2O	8.96	8.95	8.89	8.90	8.89	8.95	9.02
F	0.85	0.77	0.72	0.75	0.78	0.77	0.76
Cl	0.07	0.08	0.05	0.09	0.06	0.09	0.10
H2O (calculated)	3.40	3.49	3.50	3.46	3.45	3.46	3.48
T (iv) site: Si	5.406	5.406	5.463	5.412	5.390	5.393	5.398
Al	2.594	2.594	2.537	2.588	2.610	2.607	2.602
Al (total)	3.527	3.527	3.485	3.504	3.584	3.533	3.497
R (vi) site: Al	0.933	0.933	0.948	0.917	0.974	0.925	0.895
Ti	0.202	0.184	0.178	0.186	0.186	0.189	0.205
Cr^{3+}	0.005	0.005	0.003	0.005	0.004	0.002	0.007
Fe2+	2.735	2.782	2.708	2.780	2.725	2.802	2.769
Mn^{2+}	0.026	0.023	0.024	0.027	0.021	0.021	0.019
Mg	1.775	1.790	1.825	1.799	1.783	1.768	1.799
A (XII) site: Ca	0.002	0.001	bd	bd	bd	bd	0.001
Ba	0.005	bd	0.003	0.001	0.009	0.004	0.009
Na	0.094	0.086	0.084	0.096	0.079	0.100	0.097
K	1.793	1.767	1.766	1.770	1.775	1.777	1.785

(APPENDIX C: CONTINUED)

Biotite

Sample #	SMC-14-035	SMC-14-035	SMC-14-035	SMC-14-039	SMC-14-039	SMC-14-039	SMC-14-039
Analysis pt. #	b4-15	b4-16	b4-17	b1-01	b1-02	b1-03	b1-04
SiO_2	34.85	34.58	34.68	34.24	33.78	34.17	34.36
Al_2O_3	18.99	19.10	18.78	18.05	17.92	18.29	18.27
TiO_2	1.67	1.64	1.66	2.80	2.84	2.26	2.24
Cr_2O_3	0.03	0.02	0.05	0.04	0.05	0.04	0.03
FeO	21.31	20.88	21.16	23.30	23.01	22.97	23.33
MnO	0.18	0.17	0.20	0.11	0.16	0.13	0.15
MgO	7.75	7.68	7.79	6.68	6.56	6.51	6.66
CaO	bd	bd	bd	0.00	0.00	0.00	0.01
BaO	0.13	0.14	0.01	0.14	0.07	0.18	0.21
Na_2O	0.26	0.34	0.31	0.25	0.26	0.25	0.27
K_2O	8.98	9.00	9.02	8.86	8.91	8.92	8.76
F	0.76	0.69	0.80	0.31	0.39	0.27	0.24
Cl	0.08	0.09	0.10	0.18	0.21	0.18	0.18
H2O (calculated)	3.48	3.48	3.43	3.63	3.54	3.62	3.65
T (iv) site: Si	5.423	5.411	5.424	5.375	5.358	5.402	5.402
Al	2.577	2.589	2.576	2.625	2.642	2.598	2.598
Al (total)	3.483	3.523	3.462	3.340	3.350	3.408	3.385
R (vi) site: Al	0.906	0.934	0.886	0.715	0.709	0.810	0.787
Ti	0.195	0.193	0.196	0.331	0.339	0.269	0.265
Cr^{3+}	0.004	0.002	0.006	0.005	0.007	0.005	0.004
Fe2+	2.773	2.733	2.768	3.059	3.052	3.037	3.067
Mn^{2+}	0.024	0.022	0.027	0.015	0.021	0.018	0.020
Mg	1.798	1.792	1.816	1.563	1.551	1.534	1.561
A (XII) site: Ca	bd	bd	bd	0.000	0.001	0.001	0.002
Ba	0.008	0.009	0.001	0.008	0.004	0.011	0.013
Na	0.078	0.102	0.095	0.076	0.079	0.075	0.082
K	1.783	1.797	1.800	1.774	1.803	1.799	1.757

(APPENDIX C: CONTINUED)

Biotite

Sample #	SMC-14-039	SMC-14-039	SMC-14-039	SMC-14-039	SMC-14-039	SMC-14-039	SMC-14-039
Analysis pt. #	b2-05	b2-06	b2-07	b2-08	b2-09	b2-10	b2-11
SiO_2	34.56	34.65	34.76	34.54	34.18	34.30	34.32
Al_2O_3	17.89	17.88	18.96	18.08	17.85	18.17	17.80
TiO_2	2.64	2.72	1.69	2.48	2.34	2.45	2.66
Cr_2O_3	0.05	0.04	0.02	0.03	0.04	0.01	0.02
FeO	23.38	23.50	22.20	23.57	23.89	22.95	23.12
MnO	0.15	0.14	0.13	0.12	0.11	0.17	0.18
MgO	6.69	6.76	6.86	6.36	6.39	7.12	6.96
CaO	bd	bd	0.01	bd	0.01	0.01	0.00
BaO	0.16	0.01	bd	0.04	0.23	0.06	0.09
Na_2O	0.22	0.19	0.24	0.25	0.24	0.24	0.24
K_2O	8.88	9.00	8.80	8.93	8.80	8.93	8.92
F	0.17	0.16	0.26	0.24	0.18	0.21	0.15
Cl	0.17	0.16	0.22	0.18	0.19	0.16	0.21
H2O (calculated)	3.70	3.72	3.65	3.66	3.66	3.69	3.69
T (iv) site: Si	5.417	5.413	5.448	5.425	5.409	5.377	5.395
Al	2.583	2.587	2.552	2.575	2.591	2.623	2.605
Al (total)	3.305	3.292	3.502	3.347	3.329	3.357	3.298
R (vi) site: Al	0.721	0.705	0.950	0.772	0.738	0.735	0.692
Ti	0.311	0.320	0.199	0.293	0.278	0.289	0.314
Cr^{3+}	0.006	0.005	0.003	0.004	0.005	0.001	0.003
Fe2+	3.064	3.070	2.910	3.096	3.162	3.009	3.039
Mn^{2+}	0.020	0.018	0.018	0.016	0.015	0.023	0.024
Mg	1.563	1.574	1.603	1.489	1.507	1.664	1.631
A (XII) site: Ca	bd	bd	0.001	bd	0.002	0.001	0.000
Ba	0.010	0.001		0.003	0.014	0.004	0.005
Na	0.067	0.057	0.073	0.076	0.072	0.072	0.074
K	1.776	1.794	1.760	1.789	1.777	1.786	1.789

(APPENDIX C: CONTINUED)

Biotite	
Sample #	SMC-14-039
Analysis pt. #	b2-12
SiO_2	34.38
Al_2O_3	18.02
TiO_2	2.49
Cr_2O_3	0.03
FeO	23.17
MnO	0.17
MgO	7.02
CaO	bd
BaO	0.25
Na_2O	0.22
K_2O	8.83
F	0.26
Cl	0.23
H2O (calculated)	3.65
T (iv) site: Si	5.390
Al	2.610
Al (total)	3.330
R (vi) site: Al	0.720
Ti	0.294
Cr^{3+}	0.003
Fe2+	3.038
Mn^{2+}	0.022
Mg	1.641
A (XII) site: Ca	bd
Ba	0.015
Na	0.067
K	1.766

APPENDIX D: ELECTRON BACKSCATTERED IMAGES WITH EMPA ANALYSIS POINTS

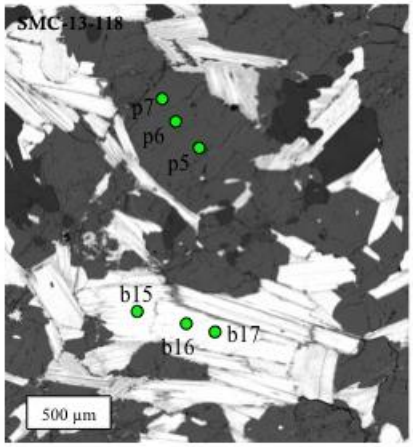

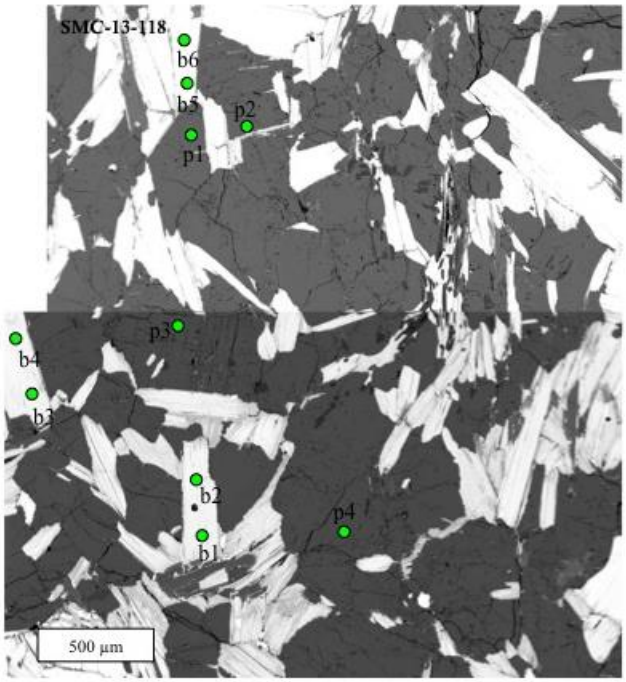

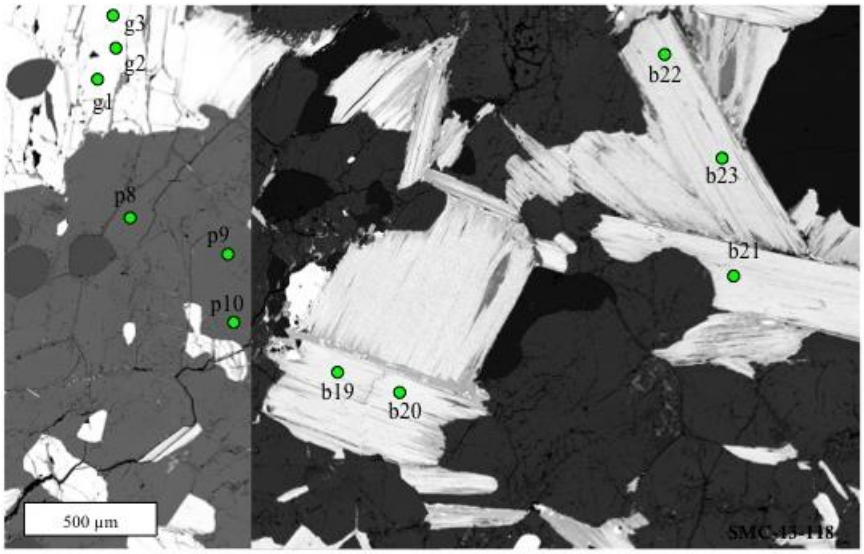

(APPENDIX D: CONTINUED)

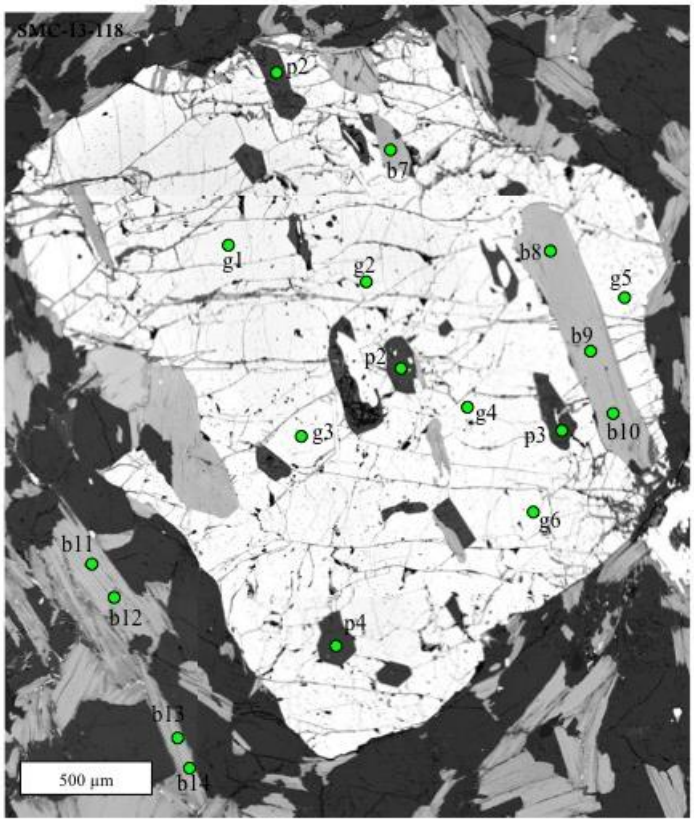

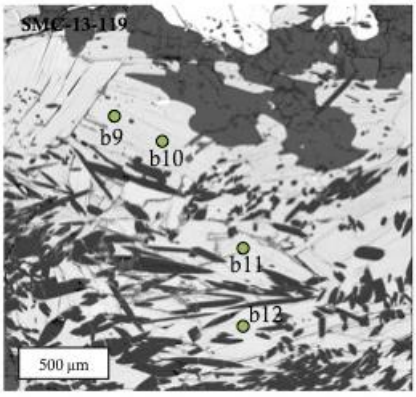

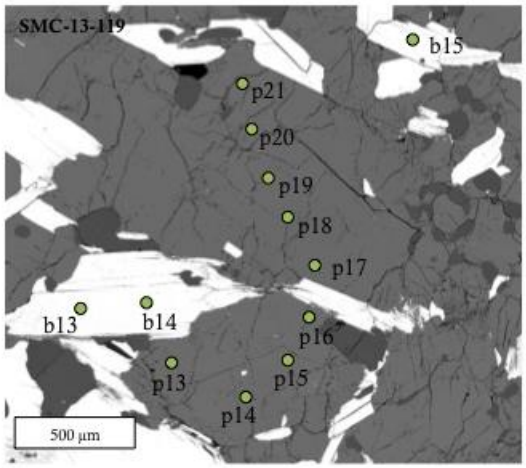

(APPENDIX D: CONTINUED)

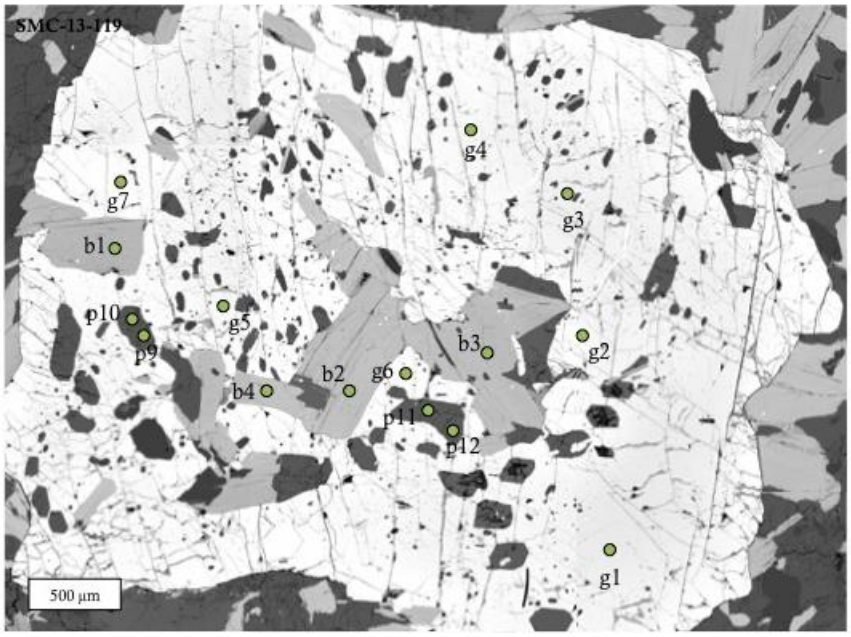

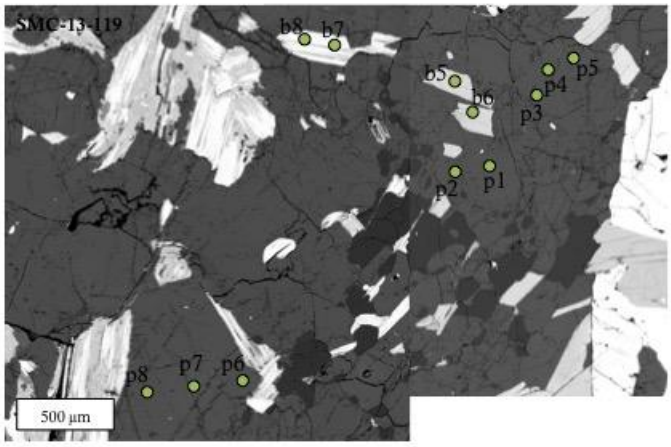

(APPENDIX D: CONTINUED)

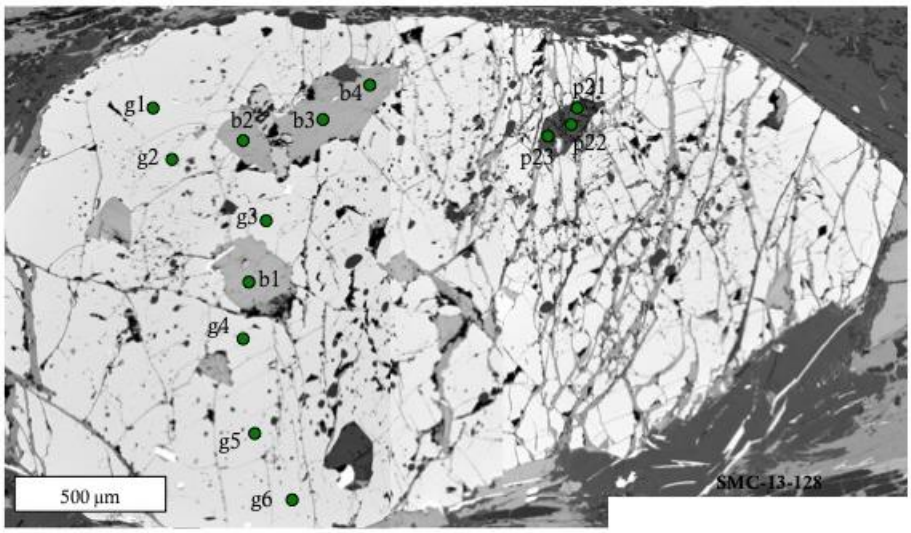

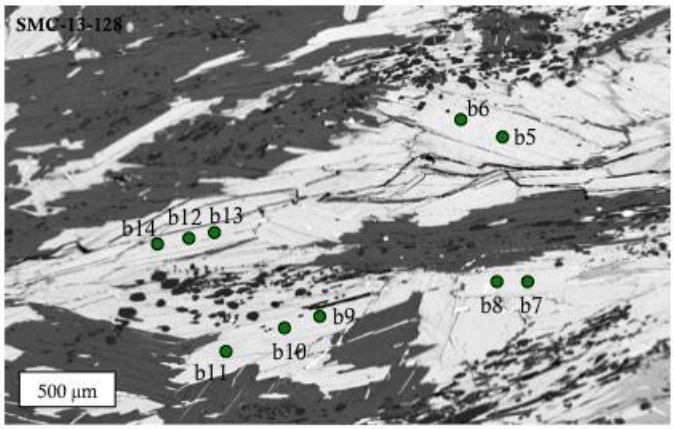

(APPENDIX D: CONTINUED)

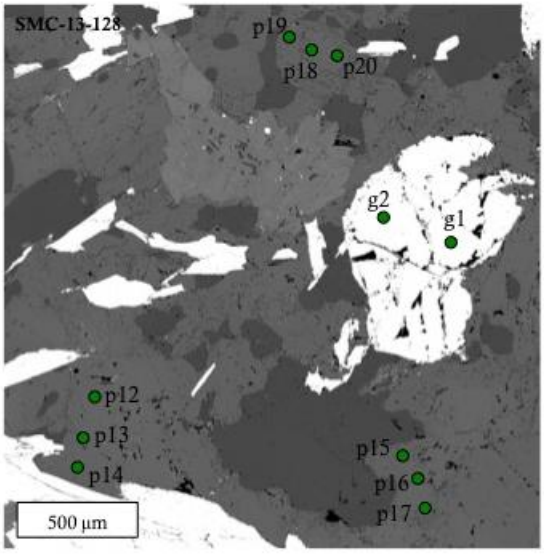

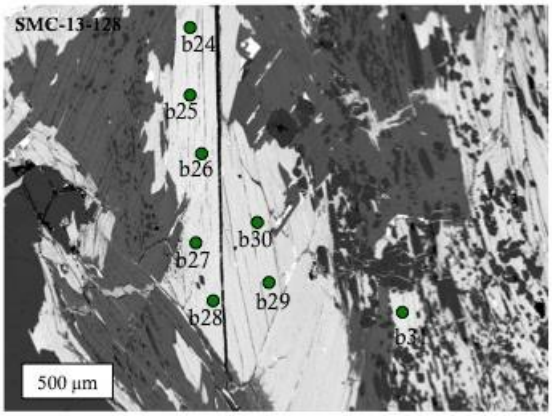

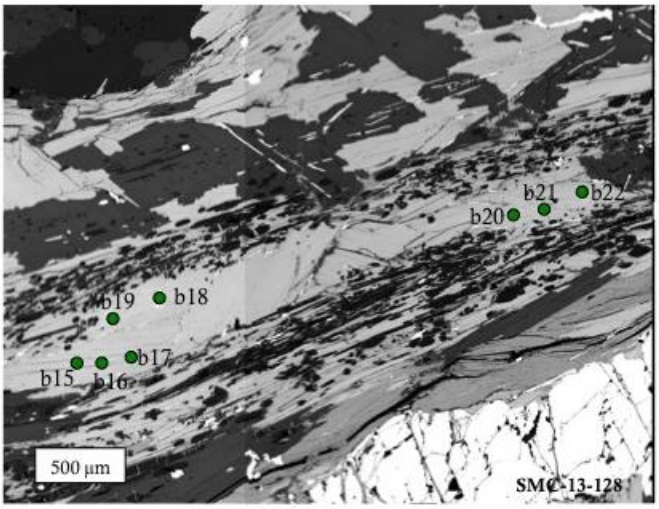

(APPENDIX D: CONTINUED)

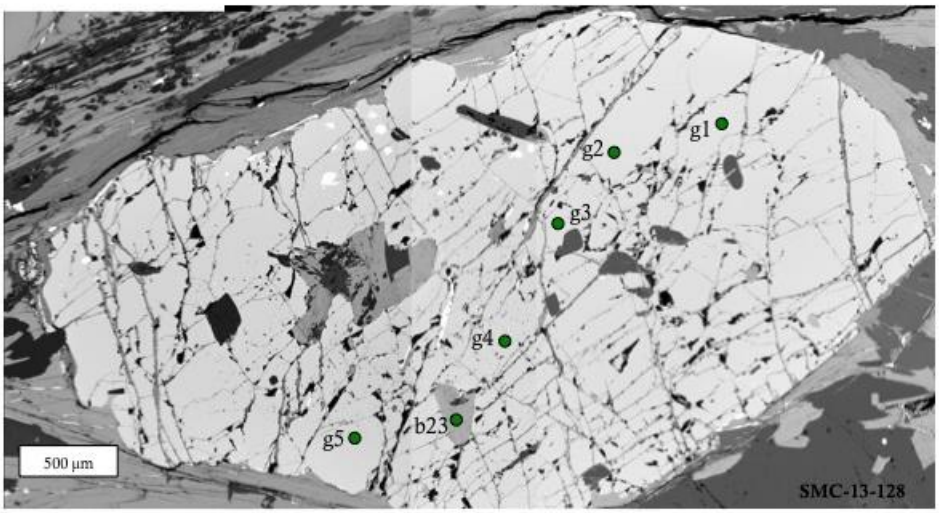

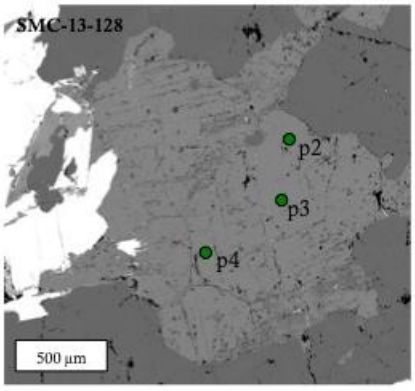

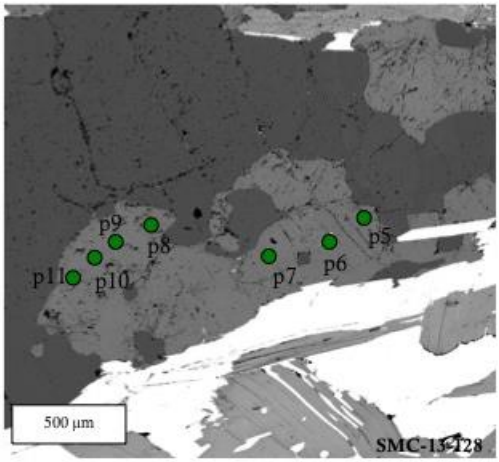

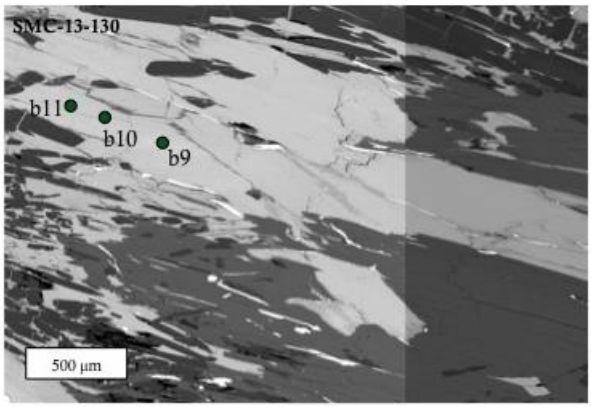

(APPENDIX D: CONTINUED)

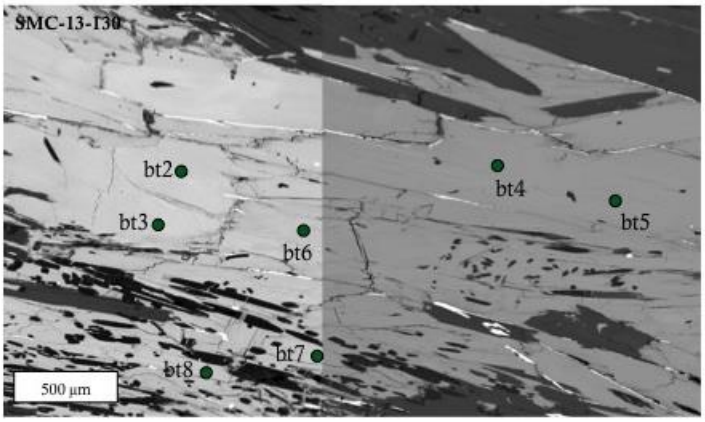

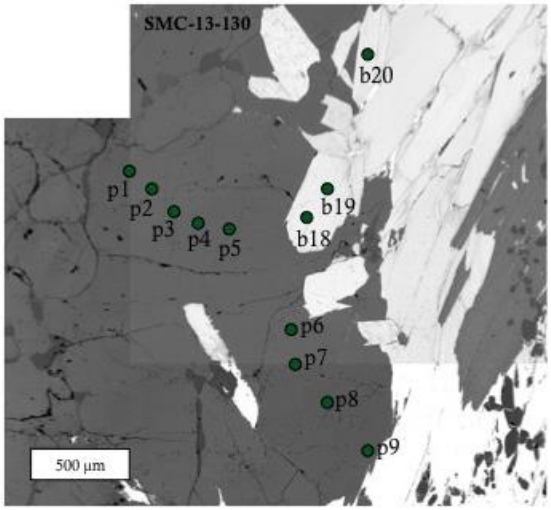

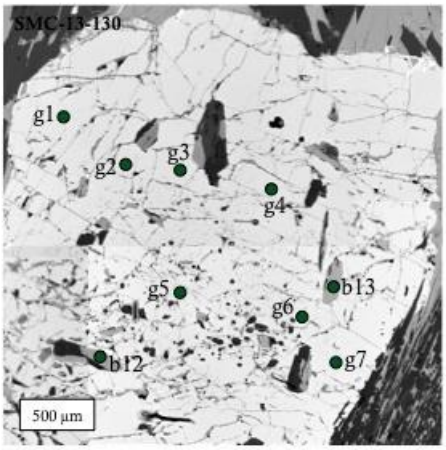

(APPENDIX D: CONTINUED)

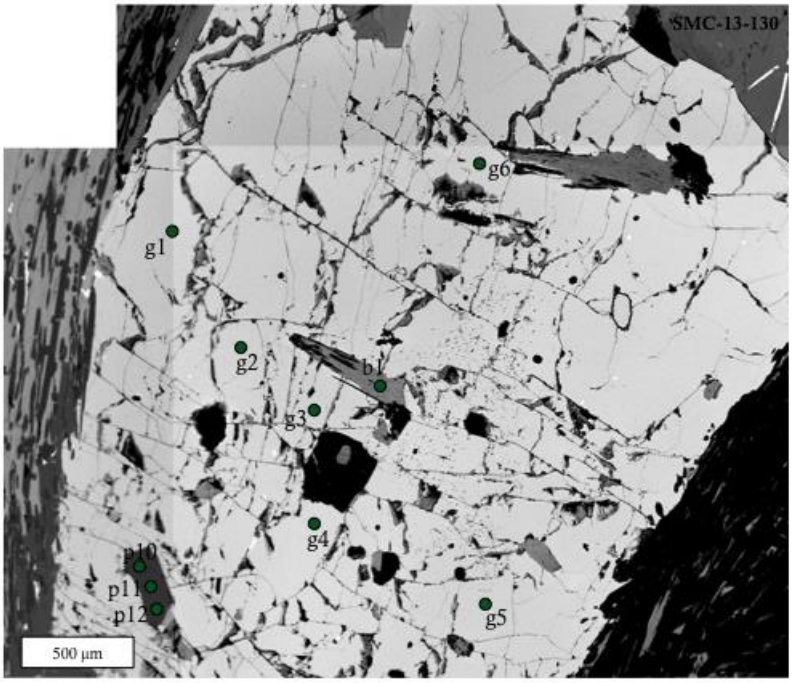

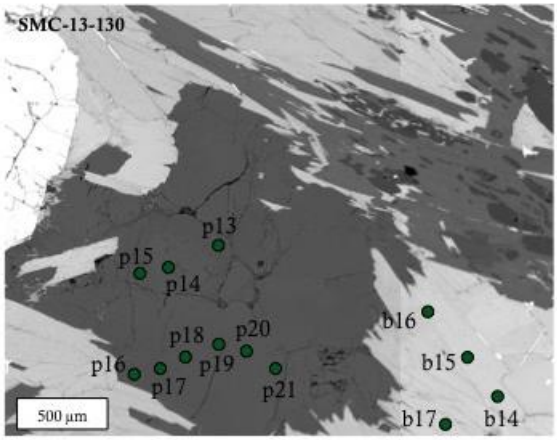

(APPENDIX D: CONTINUED)

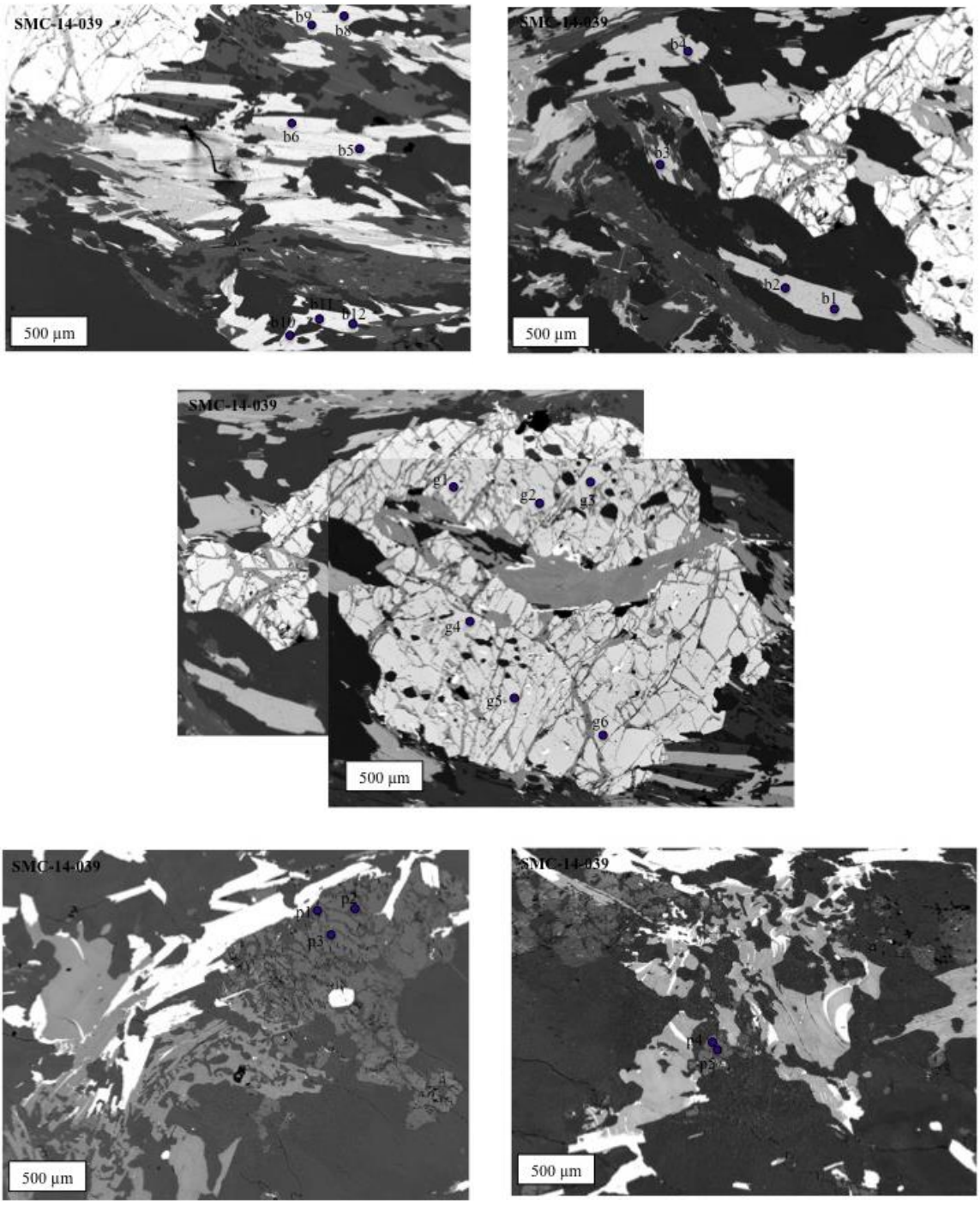

(APPENDIX D: CONTINUED)

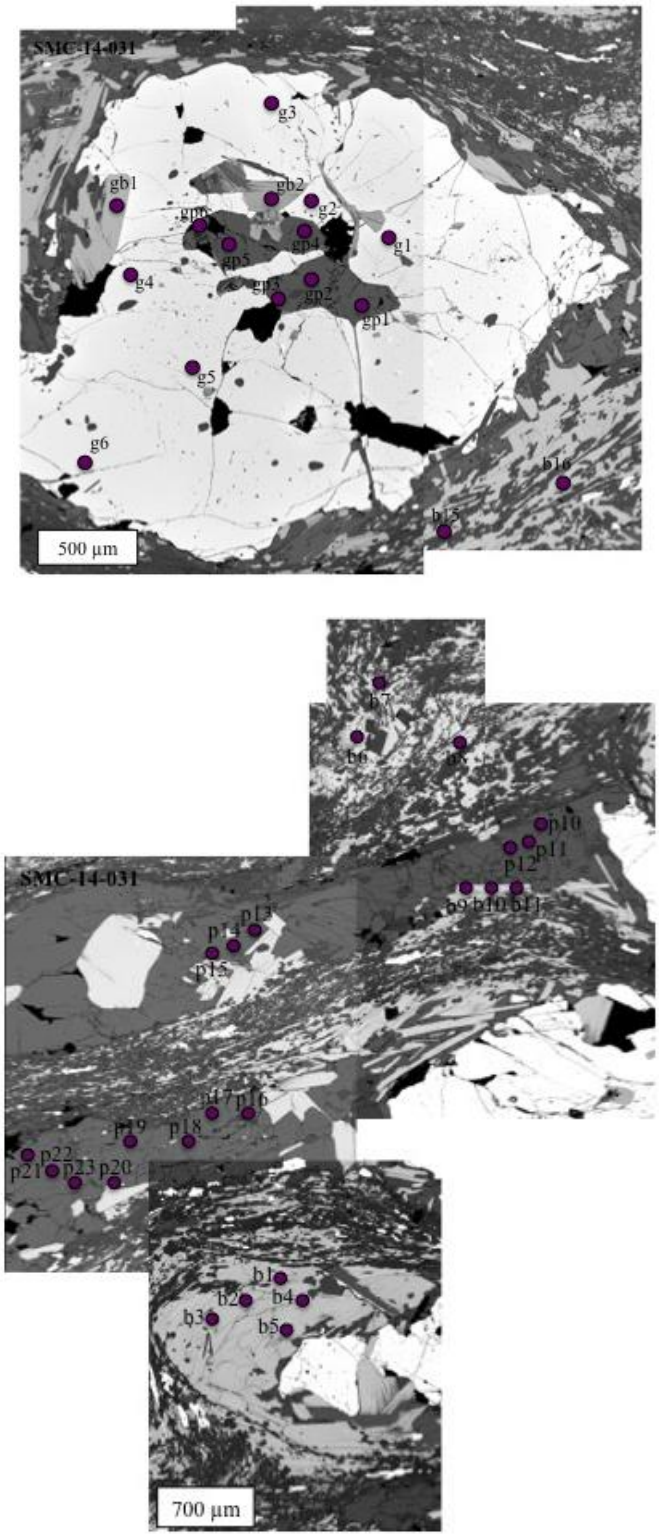

(APPENDIX D: CONTINUED)

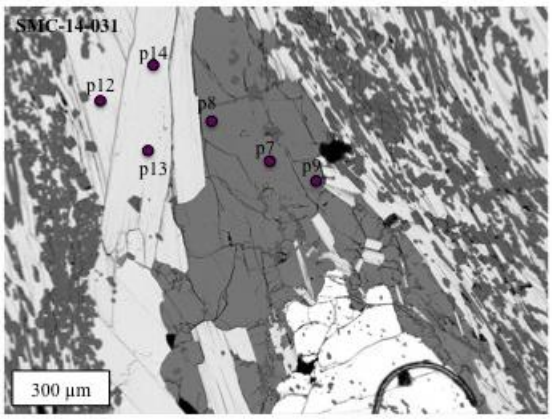

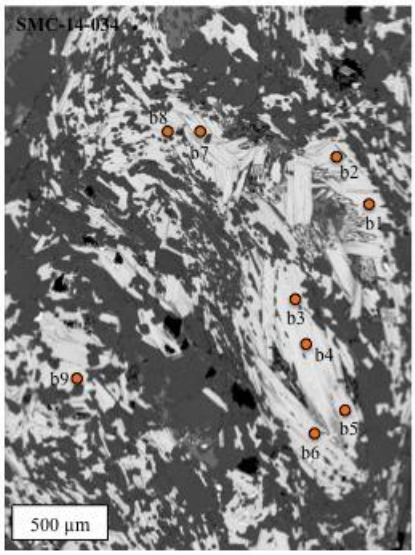

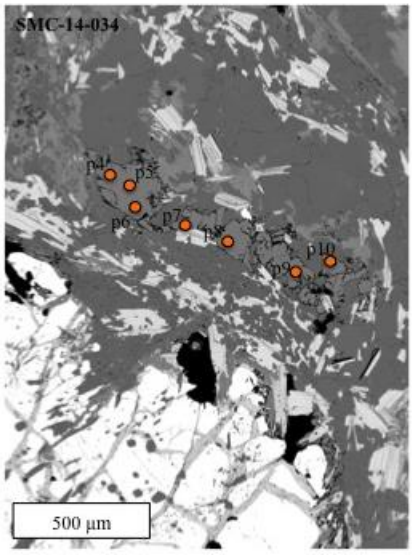

(APPENDIX D: CONTINUED)

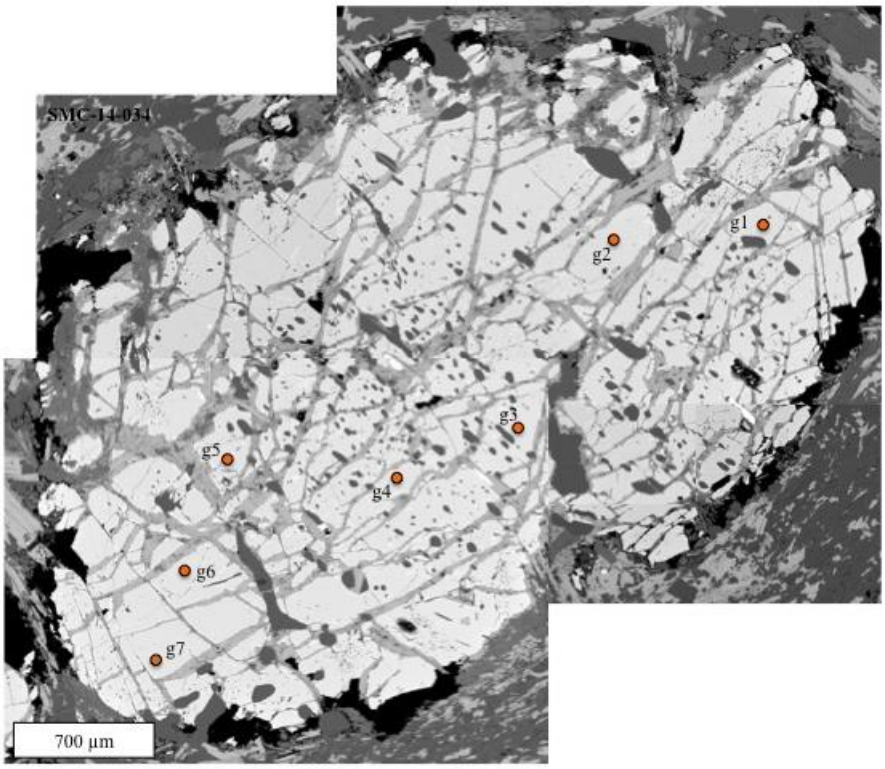

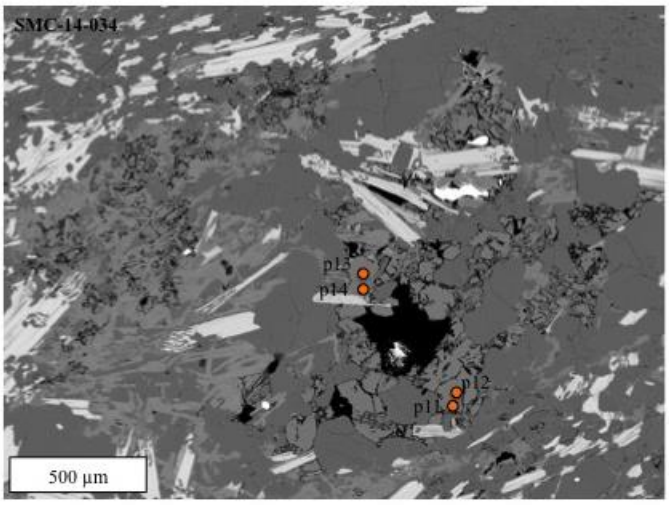

(APPENDIX D: CONTINUED)

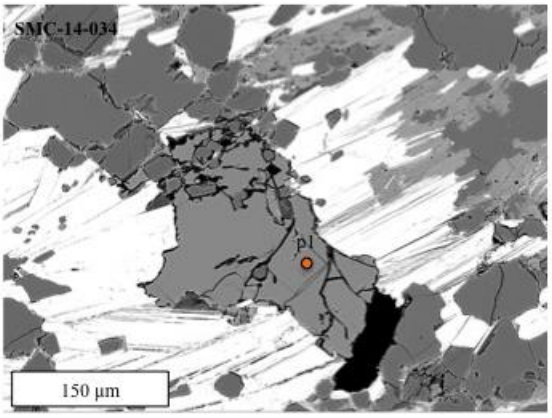

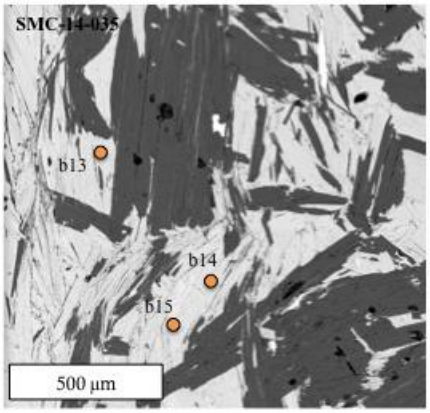

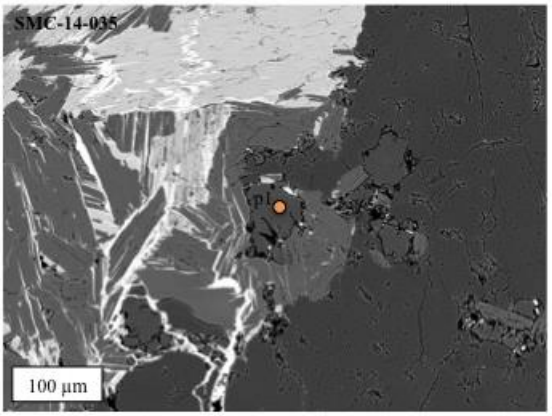

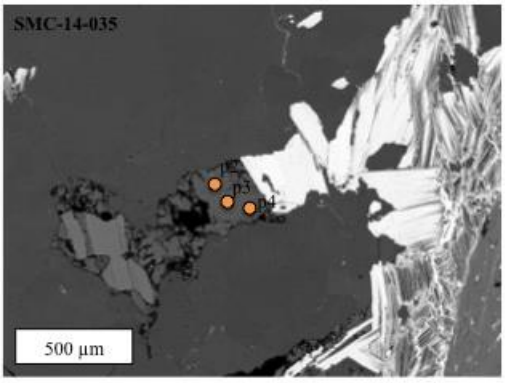

(APPENDIX D: CONTINUED)

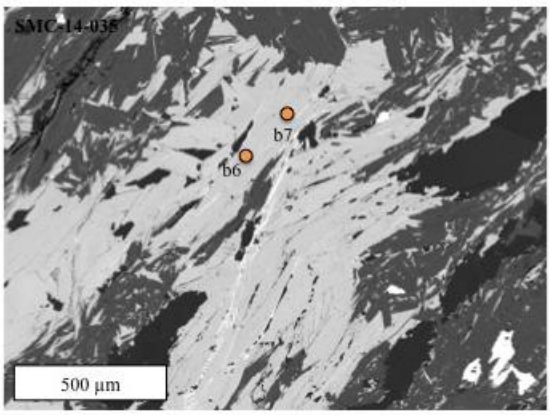

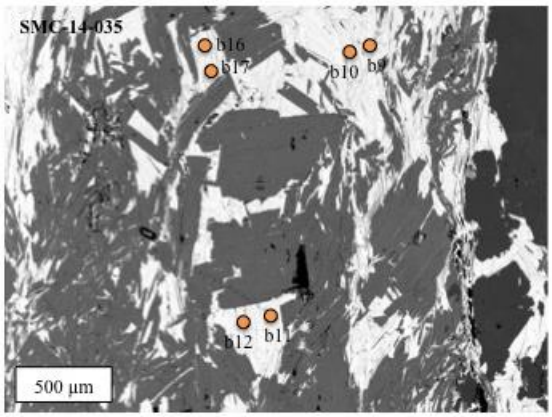

VITA

Eleanor Smith was born February 1993 in Natchez Mississippi. Eleanor developed an interest in Geology during her time at Cathedral High School and enrolled as a geology major at Louisiana State University in August, 2011. Eleanor began research under Dr. Barbara Dutrow as an undergraduate and began the LSU accelerated master's Programs her senior year. In May 2015, Eleanor successfully defended her B.S. thesis on the aluminous gneisses from the Sawtooth Metamorphic Complex, ID, and graduated with her B.S. degree.

Eleanor continued her work on the Sawtooth Metamorphic Complex in the fall of 2015 as part of the LSU accelerated master's program in geology as a senior under the guidance of Dr. Dutrow. She served as a teaching assistant to physical geology lab, igneous and metamorphic petrology, and mineralogy.

Upon completion of her thesis project, Eleanor will intern with ExxonMobil in Houston, TX before beginning a PhD program at McGill University in the Fall, 2016 Montréal, Quebec, Canada.